Heat Transfer Analysis of Air Expansion in Surge Vessels Using Large Eddy Simulation (LES)

Shuyao Li

Delft University of Technology

Heat Transfer Analysis of Air Expansion in Surge Vessels Using Large Eddy Simulation (LES)

by

Shuyao Li

Master of Science Thesis
to obtain the degree of Master of Science in Energy, Flow and Process
Technology at the Delft University of Technology

Student number:	5722624	
Date:	September 23, 2024	
Thesis committee:	Prof. dr. ir. M.J.B.M Pourquie	TU Delft, supervisor
	dr. ir. G. Oldenziel	Deltares, TU Delft, supervisor
	dr. P. Simões Costa,	TU Delft, committee member

Faculty of Mechanical Engineering
Delft University of Technology

Abstract

Surge vessels are water storage devices that maintain a consistent supply of water to a pipeline system when one or more pumps fail. A surge vessel has compressed air on top and usually water on the bottom. The heat transfer during the expansion processes of the air pocket is of great interest since the heat transfer behavior significantly affects the size of the surge vessels. Thus their thermal behavior is of great importance.

Two approaches are mainly applied to describe this heat transfer process: the classic polytropic method and the rational heat transfer (RHT) model. The polytropic model has been used for years to describe the heat transfer behavior. The RHT model can contain a detailed estimation of all heat transfer terms. This report will specifically examine the two models, highlight the advantages and disadvantages identified in current related research, and clarify the research approaches.

To address this need, the research employs both mathematical calculations and Computational Fluid Dynamics (CFD) simulations. This involves calculating various heat transfer processes and validating the simulation results against experimental data. The LES model is used to simulate the complex process of air pocket expansion within the surge vessel.

The validation process includes verifying the ideal gas model within the software, assessing mesh resolution, and evaluating the chosen models and solvers. A comparison of simulation results with experimental data from a separate case is included, providing a robust validation.

The results reveal detailed insights into the temperature and velocity fields within the surge vessel, highlighting temperature variations at probes and comparing findings with scaled models and mathematical calculations. A comparative analysis of simulation results against experimental data and mathematical calculations is also presented.

The findings of this research offer significant insights into the heat transfer characteristics within surge vessels such as temperature distribution and amount of heat transfer. These contributions are essential for refining surge vessel design.

Keyword: *Surge vessel, Pipeline system, Heat transfer, Rational heat transfer equation*

Acknowledgments

First, I would like to express my deepest gratitude to my supervisors at TU Delft and Deltares. Their support, insightful guidance, and invaluable expertise have been instrumental in the completion of this thesis. I am thankful for their dedication, for attending weekly progress meetings, and for always responding to my emails quickly. They even worked during weekends to provide me with guidance. Their patience, theoretical knowledge, and experience have not only enriched my work but also deepened my understanding of the subject.

I would also like to extend my thanks to both TU Delft and Deltares for providing the software and platforms, as well as the technical support for StarCCM+, which were crucial in completing my thesis and ensuring the successful execution of my simulations.

I would like to sincerely thank my friends, who have been a consistent source of encouragement and support throughout this entire journey. They have helped me tremendously and offered valuable suggestions throughout the process. I am also thankful for the times they joined me for drinks, which provided relaxation during stressful moments.

I am profoundly grateful to my family for their unwavering support, both emotional and financial. They gave me the confidence to persevere and the motivation to stay focused.

Finally, I would like to express my appreciation to ChatGPT for its help with formatting, grammar, and some refinement of this thesis. Its assistance allowed me to present my work in a better way.

Contents

Abstract iii

Nomenclature x

List of Figures xiii

List of Tables xix

1 Introduction 1

1.1 Background 1

1.2 Research Goals 3

1.3 Thesis Outline 3

2 Literature review 5

2.1 Surge Vessels in Pipeline Systems 5

2.2 heat transfer and relevant dimensionless numbers 5

2.3 Thermodynamics of surge vessels 7

2.4 Existing Models 7

2.4.1 Polytropic Model 7

2.4.2 Rational Heat Transfer (RHT) Equation 9

2.5 Research Approach 17

3 Research Methodology 19

3.1 Physical Model 19

3.2 Heat transfer processes 22

3.2.1 Convection 22

3.2.2 Condensation 23

3.2.3 Radiation 24

3.2.4 Work 24

3.3 Numerical model 24

3.3.1 Governing Equations 25

3.3.2 Scaled Small-size 25

3.3.3 Full-scale 27

3.4 Initial & Boundary Conditions 29

3.5 Models & Solvers 29

3.5.1 Gas Model 29

3.5.2 Flow & Energy Model 30

3.5.3 Time Solver 31
3.5.4 Mesh Morpher Solver 31

4 Validation 33
4.1 Ideal Gas Model 33
4.2 Mesh independence test 34
4.2.1 Scaled Small-size 34
4.2.2 Full Scale. 35
4.3 Models & Solvers 36
4.3.1 Scaled Small-size 36
4.3.2 Full Scale. 40
4.4 Simulation of another experimental setup 43
4.5 Experimental data & mathematical computations 44

5 Results 45
5.1 General Field Description of the Full-scale model 46
5.1.1 Temperature Field 46
5.1.2 Velocity Field 47
5.1.3 Probe Monitor 50
5.1.4 Polytropic Number 54
5.2 Scaled Small-Size Model 54
5.2.1 Temperature & Velocity Field 54
5.2.2 Probe Monitor 57
5.3 Experimental Measurements 57
5.3.1 Comparison between k-type and t-type Thermocouples in the Measurements 58
5.3.2 Comparison with Simulation Results 58
5.3.3 Discussion 59
5.4 Mathematical Calculation 61
5.4.1 Analytical estimation of heat transfer contributions 61
5.4.2 RHT Model 63
5.4.3 Dynamic Heat Transfer Calculation using 0D Numerical Model 64
5.5 Additional Experimental Case 66

6 Conclusions & Discussions 69
6.1 Conclusion 69
6.2 Discussion 70

Bibliography 75

A Simulation Setup and Parameters 79
A.1 Geometry 79
A.2 Initial & Boundary Conditions 79

A.3 Models & Solvers 79

B Validation by Rayleigh-Bénard Convection 81
B.1 Model 81
B.2 Results 83

C Impact of Structured Mesh Deformation on Simulation Convergence For the full-scale model 89
C.1 Structured Mesh 90
C.2 Models. 90
C.3 Solutions 90
C.4 Results 92

D Impact of the Coupled Solver on the volume change 95

E Non-expanding simulation results 99
E.1 Full-Scale 99
E.2 Scaled Small-size 101
E.3 Conclusion 101

F Convergence Plots of the expanding simulations 103

G Measurement Data for the Simulation Case 1 & 2 in the Experiment 105
G.1 Case 1. 105
  G.1.1 Temperature probes measurements 105
  G.1.2 Other measurements 106
G.2 Case 2. 110
  G.2.1 Temperature probes measurements 110
  G.2.2 Other measurements 110

H Impact of the Heated Frame on Thermocouple Measurements 115
H.1 Geometry & Boundary Conditions. 115
H.2 Mesh. 116
H.3 Results 117

I Calculation Process of Heat Transfer Contributions 119
I.1 Parameters 119
I.2 Gas Properties 119
I.3 Condensation 120
I.4 Convection (ignore heat transfer from the ceiling) 120
I.5 Radiation 121
I.6 Work 122
I.7 summary 122

J Matlab Codes **123**
J.1 Pressure Calculation from the RHT model 123
J.2 Heat Transfer Model of air in the surge vessel for the full-scaled model 124

Nomenclature

p	Absolute pressure [bar]
V	Air volume [m^3]
M	Molar mass [g/mol]
T	Temperature [K]
m	Mass [kg]
n	Polytropic index
N	Number of moles of air
C_p	Specific heat capacity at constant pressure [J/kgK]
C_V	Specific heat capacity at constant volume [J/kgK]
γ	Ratio of the specific heats, $\gamma = \frac{C_p}{C_V}$
U	Internal energy [J]
ϕ	Heat transfer rate [W]
Q	Heat transfer into the vessel [J]
W	Work done by the system [J]
R	Specific ideal gas constant [J/mol·K]
α	Thermal diffusivity [m^2/s]
β	Thermal expansion coefficient [1/K]
ν	Kinematic viscosity [m^2/s]
ρ	Density [kg/m^3]
σ	Stefan-Boltzmann constant [W/$m^2 \cdot K^4$]
ε	Emission factor
g	Gravitational acceleration [kg/s^2]
U	Overall heat transfer coefficient [W/m^{2}K]

h_c	Convection heat transfer coefficient [W/m^{2}K]
h_r	Radiative heat transfer coefficient [W/m^{2}K]
k	Thermal conductivity [W/m^{2}K]
A	Surface area [m^2]
RH	Relative humidity [%]
Nu	Nusselt number
Pr	Prandtl number
Ra	Rayleigh number

List of Figures

1.1 The surge vessel at the alpha loop facility at Deltares and its sketch 1
1.2 Overview of a part of a pipeline system, including surge vessels and pumping station (Zwan, 2020) 2

2.1 Optimal C value of the surge vessel volume for the polytropic model (upper bound: minimum water level; lower bound: minimum pressure) (van der Zwan et al., 2015) . . 8
2.2 temperature schematic of the vertical wall in the vessel (Graze, 1968) 10
2.3 Heat inflow and outflow schematic diagram of the surge vessel (Toussaint, 2014) 12
2.4 Heat contributions in time (solid line: conduction, dashed line: convection, dotted line: condensation, dash-dotted line: work done by the expanding volume) (Toussaint, 2014) 12
2.5 JUKLA power plant layout (Vereide et al., 2015) 13
2.6 Three regions for natural convection within a vertical cylinder at constant heat flux (Evans et al., 1968) 13
2.7 Axial temperature distributions for natural convection within a vertical cylinder with constant heat flux (Evans et al., 1968) 14
2.8 Polytropic number changing during the expansion as (a) water flow rate, (b) initial pressure, (c) initial air ratio (Chen et al., 2024a) 14
2.9 Phase (left) and temperature (right) contours in 2-phase CFD simulations (Chen et al., 2024a) 15
2.10 Principle diagram of exchanged heat quantities (Haakh, 2022) 16
2.11 Calculated internal energy U, volume work W, and heat transfer Q change for the expansion process from experimental data (Haakh, 2022) 17

3.1 Schematic diagram of the experimental surge vessel expanding 20
3.2 Measurement data from the differential pressure sensor in the experiment case 1 20
3.3 Probe locations schematic diagram in the measurement (Zhang, 2022a) 21
3.4 Real thermocouple construction in the experimental setup (red circles: locations of the thermocouples) 21
3.5 Thermal resistance schematic for the actual scenario 22
3.6 Simplified thermal resistance schematic for the simulation scenario 22
3.7 O-grid Demonstration 25
3.8 Structured mesh of the scaled small-size model 26
3.9 Unstructured mesh of the full-scale model 27
3.10 Mesh resolution in the boundary layer of the full-scale model at t = 122.29s 28

3.11 Temperature profile in the Boundary layer at t = 122.29s (dots: every 8th points on the horizontal line probe) . . . 28
3.12 Sketch of the boundary conditions . . . 29

4.1 The calculated ideal gas constant R_s of the scaled small-size simulation . . . 34
4.2 mesh independence study results for the scaled small-size model . . . 35
4.3 mesh independence study results for the full-scale model . . . 36
4.4 Initial thermocouple temperatures in the experiment case 1 . . . 37
4.5 Linear fit for probes average temperature at each height for the experiment case 1 . . . 37
4.6 Heat transfer of the bottom surface comparison between the RANS and LES model for the scaled small-size model . . . 38
4.7 Results compared between the LES model and the RANS model for the scaled small-size model at t = 47s . . . 38
4.8 Residuals compared after the lower energy residual settings for the scaled small-size model . . . 39
4.9 models and solvers results comparison for the scaled small-size model . . . 39
4.10 Initial temperature and velocity field results under experimental conditions . . . 41
4.11 thermocouple average temperature in the initial field compared with experimental initial temperature (x in the name represents the average value of different thermocouples on the same height) . . . 41
4.12 temperature comparison with the initial temperature and velocity field . . . 42
4.13 temperature comparison with the dome volume . . . 43

5.1 Zoom-in temperature field for the full-scale model at the top left corner at t = 100s . . . 47
5.2 Temperature field for the full-scale model on the middle vertical plane at different times 48
5.3 Velocity field for the full-scale model on the middle vertical plane at different times . . . 49
5.4 Geometry of two horizontal line probes for the full-scale model . . . 50
5.5 Temperature distribution of the horizontal line probe at h=0 for the full-scale model at different times . . . 51
5.7 Temperature distribution of the horizontal line probe at h=$\frac{3h}{4}$ for the full-scale model at different times . . . 51
5.6 z-direction Velocity distribution of the horizontal line probe at h=0 for the full-scale model at different times . . . 52
5.8 Geometry of the vertical line probes for the full-scale model . . . 52
5.9 Temperature distribution of the vertical line probe for the full-scale model at different times . . . 53
5.10 Temperature and velocity of the point probes for the full-scale model . . . 53
5.11 Polytropic number n during the expansion of the full-scale model and its linear fit . . . 54
5.12 Temperature field for the scaled small-size model on the middle vertical plane at different times . . . 55
5.13 Temperature field for the scaled small-size model on the middle vertical plane at different times . . . 56

5.14 Temperature probe comparison between the scaled small-size and full-scale model . . 57
5.15 Comparison between the k-type and t-type thermocouples in the measurements for case 1 58
5.16 Comparison of temperature on probes between the measurements and full-scale simulation 59
5.17 Comparison of pressure between the measurement and full-scale simulation 59
5.18 Thermal resistance schematic diagram in the measurements 60
5.19 Aluminum frame photo in the measurements 60
5.20 Measurement data from the pressure sensor in the experiment case 1 61
5.21 Measurement data from the relative humidity sensor in the experiment case 1 62
5.22 Flowchart for calculating pressure from the RHT model for case 1 63
5.23 Comparison of full-scale Simulated, Experimental, and RHT-Calculated Pressure Values for case 1 63
5.24 Flowchart for calculating heat transfer over time for 0D numerical model 64
5.25 Comparison of Heat Transfer Leaving from Vessel Surfaces to the Inside Air between the Full-Scale Simulation and 0D Numerical Model Results for Case 1 65
5.26 Volume average temperature comparison between full-scale simulation and 0D numerical model calculation results for case 1 65
5.27 Comparison of temperature on probes between the measurements and simulation in case 2 66
5.28 Polytropic number n comparison between case 1 and case 2 67
5.29 Comparison of Heat Transfer Leaving from Vessel Surfaces to the Inside Air between the Full-Scale Simulation and 0D Numerical Model Results for Case 2 67
5.30 Volume average temperature comparison between full-scale simulation and 0D numerical model calculation results in case 2 67

6.1 Temperature of the outside and inside wall during expansion in the experiment (Haakh, 2022) 71
6.2 The wire thermocouple used in Haakh's experiment measurements (Haakh, 2022) . . . 71

B.1 Mesh for the validation case, a) side view, b) top view 83
B.2 streamlines and isotherms of the validation case with Ra = 700 and Pr = 1 84
B.3 velocity field and isotherms of the simulation with Ra = 800 and Pr = 1 85
B.4 velocity field and isotherms of the simulation with Ra = 750 and Pr = 1 85
B.5 Relationship between Nusselt number and Rayleigh number 86
B.6 velocity field and isotherms of the simulation with a RANS model with Ra = 850 and Pr = 1 86

C.1 Residual Explosion Plots Due to Structured Mesh Deformation for the Full-scale Model 89
C.2 Structured Mesh of the full-scale model 90
C.3 The middle cut plane of the full-scale structured mesh one iteration before the crash with mesh deformation 91
C.4 Residual Explosion Plots by increasing inner iterations 91
C.5 Residual Explosion Plots by lowering the under-relaxation factor for the Segregated Energy solver 92

C.6 Residual Explosion Plots by using the Coupled solver 92

D.1 Temperature and volume plots for the scaled small-size model simulation with the Coupled solver and mesh morphing model 96
D.2 Temperature contour on the vertical cut plane for the scaled small-size model simulation with the Coupled solver and mesh morphing model 96
D.3 Residual plot for the scaled small-size model simulation with the Coupled solver and mesh morphing model 97

E.1 Temperature field for the non-expanding full-scale model on the middle vertical plane at different times 100
E.2 Temperature probe for the non-expanding full-scale model 101
E.3 Temperature probe comparison between the measurements and the non-expanding full-scale simulation 101
E.4 Temperature probe for the non-expanding scaled small-scale model 102

F.1 Residuals and time step monitor for the full-scale model simulation 104
F.2 Residuals and time step monitor for the scaled small-size model simulation 104

G.1 Measurement data from the temperature sensors on the first beam in the experiment for case 1 106
G.2 Measurement data from the temperature sensors on the second beam in the experiment for case 1 106
G.3 Measurement data from the temperature sensors on the third beam in the experiment for case 1 107
G.4 Measurement data from the temperature sensors on the fourth beam in the experiment for case 1 107
G.5 Measurement data from the t-type temperature sensors in the experiment for case 1 . . 107
G.6 Measurement data from the differential pressure sensor in the experiment for case 1 . . 108
G.7 Measurement data from the pressure sensor in the experiment for case 1 108
G.8 Measurement data from the relative humidity sensor in the experiment for case 1 . . . 108
G.9 Measurement data from the ambient temperature sensor in the experiment for case 1 . . 109
G.10 Measurement data from the valve position sensor in the experiment for case 1 109
G.11 Measurement data from the temperature sensors on the first beam in the experiment for case 2 110
G.12 Measurement data from the temperature sensors on the second beam in the experiment for case 2 110
G.13 Measurement data from the temperature sensors on the third beam in the experiment for case 2 111
G.14 Measurement data from the temperature sensors on the fourth beam in the experiment for case 2 111
G.15 Measurement data from the t-type temperature sensors in the experiment for case 2 . . 112

G.16 Measurement data from the differential pressure sensor in the experiment for case 2 . . 112
G.17 Measurement data from the pressure sensor in the experiment for case 2 112
G.18 Measurement data from the relative humidity sensor in the experiment for case 2 . . . 113
G.19 Measurement data from the ambient temperature sensor in the experiment for case 2 . . 113
G.20 Measurement data from the valve position sensor in the experiment for case 2 113

H.1 Geometry and names in the frame simulation 115
H.2 Mesh of the frame simulation 116
H.3 Mesh of the frame simulation for fluid and solid regions 117
H.4 Temperature contour for the frame simulation at t = 86.6 s (red dots: location of thermocouples) 117
H.5 Locations of probes for the frame simulation 118
H.6 Temperature on the probes for the frame simulation 118

List of Tables

3.1 Mesh parameters for scaled small-size numerical model 26
3.2 Mesh parameters for full-scale numerical model 28
3.3 Air properties 30

5.1 Summary of simulations and locations in the thesis 45
5.2 Initial conditions of the experimental measurement case 1 for analytical estimation . . 62
5.3 Final conditions of the experimental measurement case 1 for analytical estimation when t = 124.2s 62
5.4 Analytical estimation of heat flow from the different processes and the work done by the system for experiment measurement case 1 62

A.1 Geometry of the full-scale and scaled-small size model 79
A.2 Initial conditions 79
A.3 Boundary conditions 80
A.4 Models & solvers used in the simulation 80
A.5 Stopping criteria 80

B.1 Air properties and physical parameters in the validation case 83

1

Introduction

Chapter 1 presents an introduction to the surge vessel and the significance of analyzing the thermodynamics in surge vessels. Based on this research background, the chapter then proposes a research objective and research questions. An outline of the whole thesis is also provided.

1.1. Background

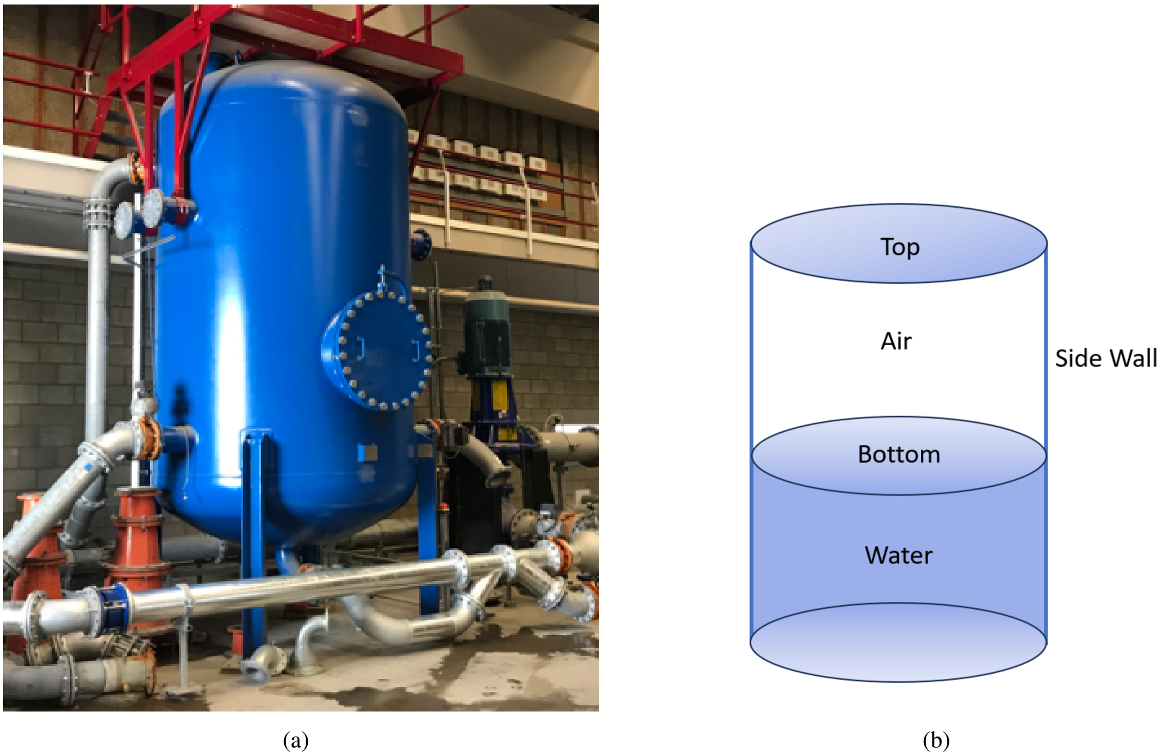

(a)

(b)

Figure 1.1: The surge vessel at the alpha loop facility at Deltares and its sketch

In pipeline systems, surge vessels, typically situated downstream of the pumping station, contain pressurized air to mitigate severe pressure fluctuations due to pump failure in the connected pipeline. An example of a surge vessel is shown in Figure 3.4. In these vessels, there is often a layer of the working fluid below the gas pocket. When one or more pumps fail, the pressure inside the pipeline will drop below the operation limit level, causing low efficiency and possibly operation failure. To protect the pipeline system, a surge vessel is installed downstream of the pumps as in figure 1.2 (Zwan, 2020). The expansion and compression processes absorb pressure surges and ensure that there is enough water available to provide water to the pipeline system. This ensures that the pipeline always has a steady water flow until the pump restarts or other measures are taken. During the expansion and compression of the gas inside, heat transfer would occur, playing an important role in the gas behavior and in the size of the air cushion and surge vessel itself. The pipeline system would be protected better with a bigger air cushion. But it would be more costly as well. Consequently, the knowledge of the dynamic behavior of the entrapped air in these vessels helps in the proper sizing of the air vessel, and also for proper behavior analysis of the pipeline system (Zhang et al.), using one-dimensional simulations with software such as WANDA.

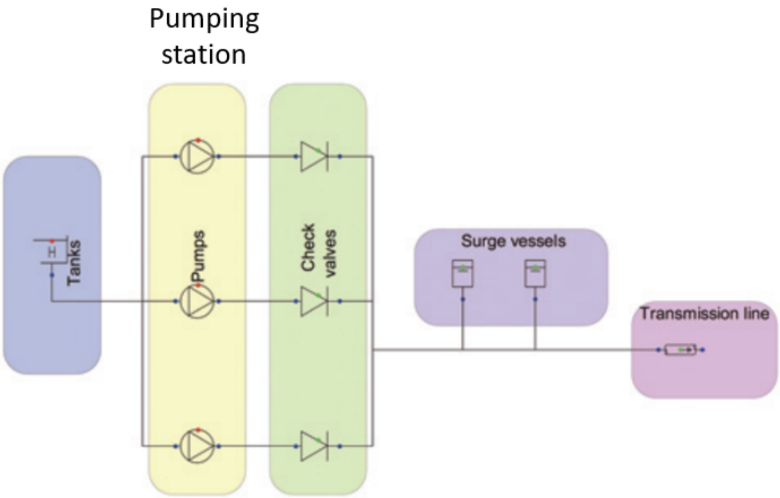

Figure 1.2: Overview of a part of a pipeline system, including surge vessels and pumping station (Zwan, 2020)

Two methods are usually applied to describe the thermodynamic behavior of surge vessels: the classic polytropic method and the Rational Heat Transfer (RHT) model. Most of the thermodynamic calculations use the classic polytropic method, which is $pV^n = constant$. Where p is the air pressure, V is the air volume, and n is the polytropic index. The polytropic index is supposed to be a certain number between 1.0 and 1.4, the isothermal and adiabatic approximation respectively. But in reality, the heat transfer process is neither isothermal nor adiabatic but changes over time. The polytropic index initially is approximately 1.4 (adiabatic state), and then gradually decreases to close to 1.0 (isothermal state). The polytropic model with values of 1.0 and 1.4 does not account for the temperature and heat transfer dynamics within surge vessels. The heat transfer in a cylinder filled with air is analyzed in the RHT model, using the ideal gas law (Graze, 1968). In Graze's work on the RHT model, in the term $\frac{\mathrm{d}Q}{\mathrm{d}t}$ only the convection between the inside wall and the air is considered and it is only for one phase inside the vessel, namely air. So some modifications still need to be made to improve the model.

1.2. Research Goals

Three main problems will be analyzed and discussed in this project:

1. Develop an analytical model for the heat transfer based on the RHT model
2. Use a Computational Fluid Dynamics (CFD) model to simulate the process of heating of air in a vessel after the expansion of air, and possibly during the expansion, for heat transfer analysis
3. Find a robust relation to describe the thermodynamics of the surge vessel

1.3. Thesis Outline

The remainder of this document is organized as follows:

In Chapter 2, the current state of research on surge vessels and the related heat transfer processes is explored. It focuses on two primary modeling approaches: the polytropic model and the Rational Heat Transfer (RHT) model. The review highlights the strengths and limitations of these models, setting the foundation for the methodological approach chosen in this study.

In Chapter 3, the methodologies employed in the study are detailed. It begins with a description of the physical models and mathematical equations. The chapter then discusses the numerical models used, including the initial and boundary conditions. Additionally, the choice of models and solvers, as well as the computational setup, are explained. This comprehensive methodology lays the groundwork for the simulations and analyses conducted in later chapters.

In Chapter 4, the validation is conducted to ensure the accuracy and reliability of the simulations. It includes validation of the ideal gas equations, mesh independence studies, and the models and solvers used in the simulations. Furthermore, the chapter presents the validation of experimental measurement data and mathematical computations. This validation chapter confirms that the models and methods are well-suited for the study's objectives and ensures confidence in the subsequent results.

In Chapter 5, the simulation and mathematical results are presented and analyzed, focusing on the temperature and velocity fields for two different sizes of the surge vessels. The chapter investigates the heat transfer phenomena observed in the simulations, comparing the results against experimental data and analytical computations.

In Chapter 6, the key findings are summarized, emphasizing the contributions to the understanding of heat transfer in surge vessels. It discusses the implications of the results for both theory and practice. The chapter concludes with recommendations for future research, identifying potential areas for further investigation to enhance the models and methods developed in this study.

2

Literature review

In this section, an overview of the existing research on surge vessels and their thermodynamics is provided. First, relevant research on the different functions of surge vessels is included. The necessity of thermodynamic analysis of surge vessels is also mentioned in this section. Then, the thermodynamic principles used in current research on surge vessels are analyzed, and the heat transfer analysis in cylindrical geometries is also considered as a supplement.

2.1. Surge Vessels in Pipeline Systems

Surge vessels act as temporary buffers to maintain flow stability in a water supply system. These vessels are deployed to mitigate the effects of pump failures or power outages, ensuring sustainable water supply and preventing damage to the pipeline system. In addition to the functions mentioned before, surge vessels are also used to handle specific events, such as the water hammer phenomenon, where sudden pressure changes in the pipeline need to be absorbed and prevented (Chen et al., 2024b). Water hammer is a hydraulic phenomenon during which rapid pressure fluctuations result from sudden changes in pipeline systems such as a valve closure. These surge vessels are widely used in the industry to protect pipeline systems from water hammer. Although they are designed with different considerations and requirements for emergencies, these surge vessels share the same function and purpose of pressure surge mitigation.

Accurate modeling of the thermodynamic behavior of the air pocket in the vessels is crucial for the precise sizing and design of surge vessels (van der Zwan et al., 2015). Two main models— the Polytropic model and the Rational Heat Transfer (RHT) model—have been developed to describe the thermodynamic behavior of heat transfer in surge vessels. In the following sections, these models will be discussed in detail, highlighting their principles and limitations.

2.2. heat transfer and relevant dimensionless numbers

This section introduces the key dimensionless numbers relevant to surge vessel heat transfer analysis. In surge vessel studies, dimensionless numbers such as the Rayleigh number, Nusselt number, and Prandtl number help characterize the thermodynamic performance of the air in surge vessels.

Rayleigh number

The Rayleigh (Ra) number is a dimensionless number that characterizes the fluid's flow regime driven by buoyancy forces (Mills, 1999). A higher Ra number indicates turbulent flow, while a lower Ra indicates laminar flow. The Ra number is given by:

$$Ra = \frac{g\beta(T_s - T_\infty)L^3}{\nu\alpha} \tag{2.1}$$

where, g is the gravitational acceleration, β is the thermal expansion coefficient of the air, T_s is the surface temperature of the vessel wall, T_∞ is the air temperature inside the vessel, L is the height of the vessel, ν is the kinematic viscosity of the air, α is the thermal diffusivity of the air.

Nusselt number

The Nusselt (Nu) number is a dimensionless number that is the ratio of total heat transfer to conductive heat transfer at a boundary in a fluid (Mills, 1999). The Nu number is determined by the Ra number. For heat transfer from flat plates, the relationship between Ra and Nu differs depending on whether the surface is horizontal or vertical.

For example, the Nu relation for heat transfer for a vertical plate (Mills, 1999):

For $Ra_L \leq 10^9$:

$$\overline{Nu}_L = 0.68 + 0.670\,(Ra_L\Psi)^{1/4} \tag{2.2}$$

Where,

$$\Psi = [1 + \left(\frac{0.492}{Pr}\right)^{9/16}]^{-16/9} = 0.347$$

.

For $10^9 \leq Ra_L < 10^{12}$:

$$\overline{Nu}_L = 0.68 + 0.670\,(Ra_L\Psi)^{1/4}\left(1 + 1.6 \times 10^{-8} Ra_L\Psi\right)^{1/12} \tag{2.3}$$

Where, Pr is the Prandtl number of air, indicating the ratio of momentum diffusivity to thermal diffusivity, which is 0.71.

For a horizontal plate with a heated upper surface (Incropera and De Witt, 1985):

For $10^7 < Ra_L < 10^{11}$

$$\overline{Nu}_L = 0.15 Ra_L^{1/3} \tag{2.4}$$

For $10^4 < Ra_L < 10^7$

$$\overline{Nu}_L = 0.54 Ra_L^{1/4} \tag{2.5}$$

Convective heat transfer coefficient h

The convective heat transfer coefficient h can then be calculated from the Nu number using the relation:

$$h = \frac{Nu \cdot k}{L} \tag{2.6}$$

where, k is the thermal conductivity of air.

2.3. Thermodynamics of surge vessels

During the failure of the pump, the water level of the surge vessel starts to drop to compensate for this. The air pocket in the surge vessel expands consequently and the temperature drops. Then the temperature of surrounding walls and water is higher than that of the air in the surge vessel, causing heat transfer from water and wall to the air. Subsequently, the air temperature inside the vessel increases.

The polytropic model is commonly used to describe this phenomenon (Wylie et al., 1993). Initially, the polytropic process of the air within the vessel approximates an adiabatic process (polytropic number n = 1.4), and as the domain expands, it gradually transitions towards an isothermal process (n = 1.0) (Akpan et al., 2014; Thorley, 2004). Therefore, the polytropic number changes over time, and a single value cannot describe the thermodynamic variations involved. Then, a thermal equilibrium analysis of the thermodynamic processes within the air inside the vessel is necessary, leading to the proposal of the RHT model (Graze, 1968). The primary modes of heat transfer within the vessel include convection, radiation, and phase change heat transfer. Computational studies have evaluated the significance of these modes, showing that convection, primarily occurring through the sidewalls, is the dominant mode of heat transfer (Toussaint, 2014). This is influenced by parameters such as the vessel size, air properties, and the duration of air expansion within the vessel. Computational Fluid Dynamics (CFD) multiphase simulations have further explored these phenomena, demonstrating that the air temperature within the vessel can drop significantly during expansion (Chen et al., 2024a). Experimental studies also support these findings, showing an initial temperature drop followed by a gradual rise (Haakh, 2022). Early studies indicate that during the cooling phase of air expansion, a boundary layer will form near the sidewalls, and high-temperature gas accumulates near the top of the vessel (Drake, 1966; Evans et al., 1968).

Based on these insights, it is essential to investigate the changes in the polytropic number of air inside the vessel during and after the expansion, as well as the temperature distribution along the vessel's height and radius, and to develop specific temperature field profiles. These analyses will help refine the understanding of the thermodynamic behavior of air in surge vessels, leading to improved vessel design and performance optimization.

2.4. Existing Models

2.4.1. Polytropic Model

The Polytropic model assumes that the state of the entrapped air pocket within the surge vessel can be approximated to be a polytropic process as its pressure, temperature, and volume change during the expansion and compression processes (Wylie et al., 1993).

The polytropic relationship:

$$pV^n = C \tag{2.7}$$

The ideal gas law:

$$pV = NRT \tag{2.8}$$

Where p is the absolute air pressure; V is the air volume; n is the polytropic index, also known as the Laplace coefficient, varying between 1.0 for the isothermal process and 1.4 for the adiabatic process; C is a constant; T is the gas temperature; N is the number of moles of air.

With the C value, the initial air volume and initial water level can be determined by the pressure in the pipeline system. The acceptable range of C values is bounded by the minimum pressure (n = 1.4) and minimum water level (n = 1.0). While assuming the isothermal approximation (n = 1.0), more heat would be absorbed in the air cushion, causing a larger expansion. The water level in the surge vessel needs to be higher than the pipeline to prevent air from entering. While assuming the adiabatic approximation, there is insufficient time for heat exchange. The air transient is very rapid and the inlet and outlet heat transfer can be neglected (Thorley, 2004). The minimum pressure needs to be higher than the design pressure of the surge vessel and pipeline system. For both cases, acceptable values for the different sizes of surge vessels can be determined, as in Figure 2.1. In the figure, a combination of the C value and surge vessel volume in the white area is acceptable.

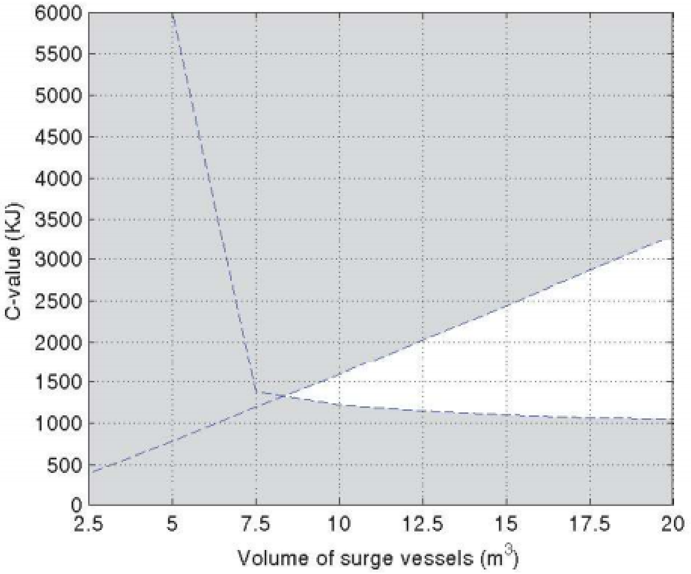

Figure 2.1: Optimal C value of the surge vessel volume for the polytropic model (upper bound: minimum water level; lower bound: minimum pressure) (van der Zwan et al., 2015)

By equation (2.7) and (2.8), the time-dependent Laplace coefficient can be written as:

$$n = \frac{\log \frac{p_0 V_0^{n_0}}{p}}{\log V} \tag{2.9}$$

Where p_0 and V_0 are initial pressure and volume of air; p and V are calculated values.

An intermediate value of n = 1.2 is sometimes used as a compromise. However, this value leads to inaccuracies in both the fluid level and the pressure (Leruth et al., 2012), so not one single value of n can sufficiently describe the whole process. The polytropic model tends to underestimate energy loss and the rate of pressure decreases (Zhou et al., 2023).

Graze (H.R.Graze, 1967) noticed that for a certain process with a constant polytropic number n = 1.2, heat transfer is required from cold to warm, which violates the second law of thermodynamics and is thus not possible. According to the second law of thermodynamics, heat flows only from a high-temperature region to a low-temperature region, resulting in a heat outflow. However, the polytropic model assumes heat inflow during certain time intervals, which contradicts the second law of thermodynamics (Akpan et al., 2014).

2.4.2. Rational Heat Transfer (RHT) Equation

Model description

Graze proposed a rational heat transfer (RHT) model to describe the air behavior in surge vessels (Graze, 1968). The air inside the vessel is assumed to be an ideal gas. The detailed derivation of the rational heat transfer (RHT) model is below:

For an ideal gas, it holds that:

$$C_p - C_v = R_s \tag{2.10}$$

Where C_p and C_v are specific heat capacities at constant pressure and volume; R_s is the specific ideal gas constant.

The first law of thermodynamics is:

$$\mathrm{d}U = \mathrm{d}Q - \mathrm{d}W \tag{2.11}$$

Where $\mathrm{d}U$ is the internal energy change; $\mathrm{d}Q$ is the heat transfer into the vessel; $\mathrm{d}W$ is work done by the system, where $\mathrm{d}W = p\mathrm{d}V$.

By Equation 2.8, 2.10, and 2.11 we have, for constant c_p and c_v:

$$\frac{1}{\gamma - 1} d(pV) = -dQ - pdV \tag{2.12}$$

After rearrangement of Equation 2.12:

$$\frac{\mathrm{d}p}{\mathrm{d}t} = -\gamma \frac{p}{V} \frac{\mathrm{d}V}{\mathrm{d}t} - \frac{(\gamma - 1)}{V} \frac{\mathrm{d}Q}{\mathrm{d}t} \tag{2.13}$$

or, in terms of Head:

$$\frac{\mathrm{d}H}{\mathrm{d}t} = -\gamma \frac{H}{V} \frac{\mathrm{d}V}{\mathrm{d}t} - \frac{(\gamma - 1)}{\rho_w g V} \frac{\mathrm{d}Q}{\mathrm{d}t} \tag{2.14}$$

Where γ is the ratio of the specific heats, defined by $\gamma = \frac{C_p}{C_v}$; ρ_w is the density of water; H is the absolute pressure head of the air volume; g is the gravitational acceleration.

The main equation of the RHT model is given by Equations 2.13.

Further research

Following the RHT model, Graze specifically analyzed the term $\frac{dQ}{dt}$ in the RHT model as below (H.R.Graze, 1967). It neglects the conduction through the walls, as well as the radiation heat transfer inside the vessel and the radiation and convection heat transfer outside the vessel.

The rate of heat outflow:

$$\frac{\mathrm{d}Q}{\mathrm{d}t} = UA(T_{in} - T_{ex}) \tag{2.15}$$

Where A is the heat transfer contact area, namely the sum of the side and top and bottom surfaces, $A = 2\pi r_2(X + r_2)$, r_2 is the inner radius of the surge vessel; X is the height of the air cushion in the surge vessel; U is the overall heat transfer coefficient; T_{in} and T_{ex} are internal and external air temperature.
By involving all three modes of heat transfer, the heat transfer coefficient can be calculated:

$$\frac{1}{U} = \frac{1}{2\pi}\left[\frac{1}{r_2(h_{c2} + h_{r2})} + \frac{\ln \frac{r_3}{r_2}}{k_t} + \frac{1}{r_3(h_{c3} + h_{r3})}\right] \tag{2.16}$$

Where r_2 and r_3 are internal and external wall radius; h_{c2} and h_{c3} are internal and external convection heat transfer coefficient; h_{r2} and h_{r3} are internal and external radiative heat transfer coefficient; k_t is the thermal conductivity of the vessel wall, assumed constant.
The temperature schematic of the vertical wall in the vessel is in Figure 2.2.

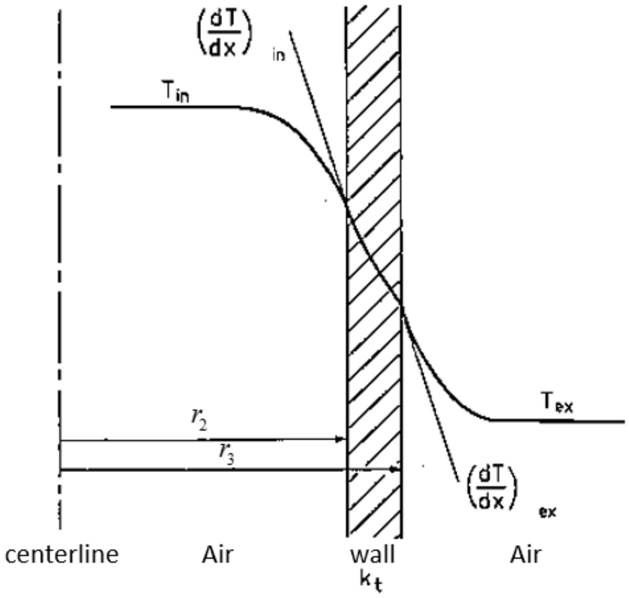
$\left(\frac{dT}{dx}\right)_{in}$
T_{in}
T_{ex}
r_2
r_3
$\left(\frac{dT}{dx}\right)_{ex}$
centerline
Air
wall
k_t
Air

Figure 2.2: temperature schematic of the vertical wall in the vessel (Graze, 1968)

Assumptions are made for a suitable expression of the overall heat transfer coefficient in the RHT model by Graze:

1. Air is an ideal gas
2. The value of h_{r2} is essentially zero since the Nitrogen and Oxygen gas in the air are transparent to radiation and the surfaces of the inner walls are at the same temperature at any time
3. The wall of the vessel is thin ($r_2 \approx r_3$) so the conductive term is negligible compared to the convection terms
4. Convection and radiative resistance on the outside wall is negligible considering the relatively small magnitude

Therefore, Graze uses the simplified overall heat transfer coefficient:

$$U = h_{c2} \times A \tag{2.17}$$

Graze also conducted experiments on the characteristics of trapped air in a vertical pipe to verify the RHT model. The experimental model utilized by Graze is considerably smaller in scale compared to the surge vessel. The result shows that the heat transfer coefficient calculated by the RHT model is scale and system-dependent.

Additionally, it's difficult to accurately substitute the appropriate form of the heat outflow rate $\frac{dQ}{dt}$ in the RHT model equation due to the complex thermodynamics, so the model is not used widely for the design of surge vessels. Therefore, Akpan (Akpan et al., 2019) proposed a modified Equation based on Equation 2.14:

$$\frac{\mathrm{d}H}{\mathrm{d}t} = -\gamma \frac{H}{V}\frac{\mathrm{d}V}{\mathrm{d}t} - \frac{(\gamma - 1)}{\rho_w g V}\dot{Q}_{ar} \tag{2.18}$$

Where $\dot{Q}_{ar}$ is a constant heat transfer outflow rate term. This term was determined numerically through an iterative adjustment of the heat outflow rates until the thermodynamic behavior of the entrapped air agreed with the solution of the polytropic models within a reasonable limit.

However, the iterative adjustment of Q_{ar} requires a considerable amount of time, and despite the effort, the obtained results may not be accurate enough. Besides, the number of Q_{ar} is verified solely through comparison with the Polytropic model, lacking experimental validation. Consequently, the applicability of the model remains unproven.

Besides, the assumptions of the RHT model by Graze, and specifically the heat transfer term, $\frac{\mathrm{d}Q}{\mathrm{d}t}$, ignore too many heat transfer factors and geometric factors.

Toussaint (Toussaint, 2014) proposed a lumped 0D model to analyze the heat balance and heat flow caused by thermal conduction, convection, radiation, and phase change as in Equation 2.19, see Figure 2.3.

$$\frac{\mathrm{d}\rho_{air} V c_p T}{\mathrm{d}t} = \phi_{conduction} + \phi_{convection} + \phi_{condensaton} - \phi_{evaporation} + \phi_{radiation} - \frac{\mathrm{d}W}{\mathrm{d}t} \tag{2.19}$$

By calculating each term of the heat flow, Toussaint finds that convective heat transfer accounts for the largest proportion, followed by conduction, and phase change, as shown in Figure 2.4. Since the heat transfer between the surge vessel wall and the internal air is convective, the conduction term in Toussaint's model is already included in the convective heat transfer and should be neglected. Convective heat transfer is dominant due to the large contact area and temperature difference between the air and walls of the surge vessel.

The 0D calculated results from Toussaint are compared and validated with the tests from a large pipeline system located in Shuweihat in the Arab Emirates. Compared to the results from Shuweihat, the volume results show a relatively small error margin of 5.67%. The pressure results, however, exhibit a significant error of approximately 41.67%. Regarding temperature change, according to the data from Shuweihat, the temperature remains relatively constant, whereas the computed data with Toussaint's model indicates a change of 18 K, resulting in an error of around 35.48%. This difference could be at-

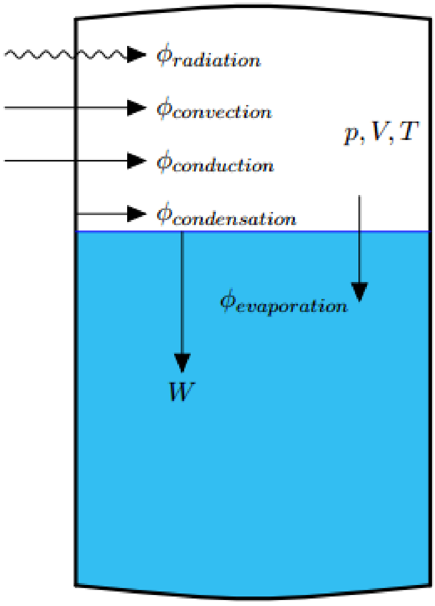

Figure 2.3: Heat inflow and outflow schematic diagram of the surge vessel (Toussaint, 2014)

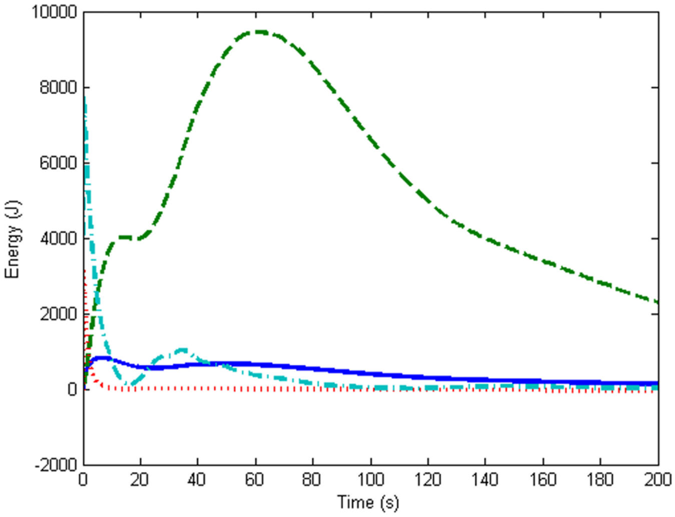

Figure 2.4: Heat contributions in time (solid line: conduction, dashed line: convection, dotted line: condensation, dash-dotted line: work done by the expanding volume) (Toussaint, 2014)

tributed to the locations of the thermocouples and potential inaccuracies in the recorded data. Besides, this heat transfer model underestimates the heat transfer because only the 0-D analysis is considered, which means the properties of air (temperature, pressure, density, etc.) in the surge vessel are all volume averaged.

Vereide et al. (Vereide et al., 2015) apply the RHT model to surge vessels for JUKLA power plants underground, as shown in Figure 2.5. For the $\frac{dQ}{dt}$ term, the contributions of heat transfer of water and walls are considered separately. Specifically, different Nusselt number relations are applied to compute the convective heat transfer coefficients for horizontal water surfaces and vertical wall surfaces. Then, this $\frac{dQ}{dt}$ value is substituted into the RHT model for calculation. This model was compared regarding measured water level and pressure values, and temperature changes with a polytropic model. It shows a better fit to the measured data compared to the polytropic model, although some deviation remains. However, temperature changes are not measured so the model cannot be accurately assessed.

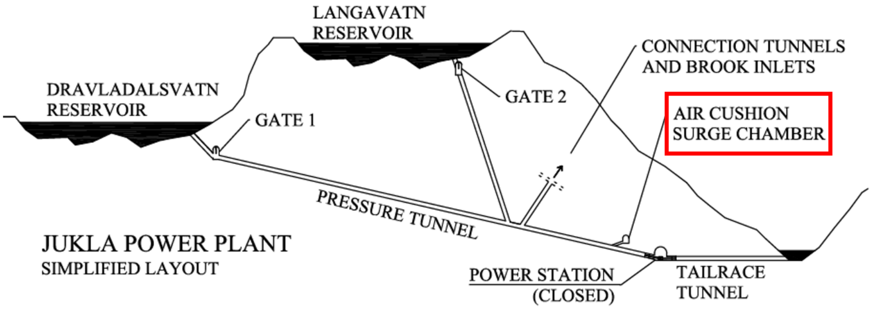
LANGAVATN RESERVOIR
DRAVLADALSVATN RESERVOIR
GATE 1
GATE 2
CONNECTION TUNNELS AND BROOK INLETS
AIR CUSHION SURGE CHAMBER
PRESSURE TUNNEL
JUKLA POWER PLANT
SIMPLIFIED LAYOUT
POWER STATION (CLOSED)
TAILRACE TUNNEL

Figure 2.5: JUKLA power plant layout (Vereide et al., 2015)

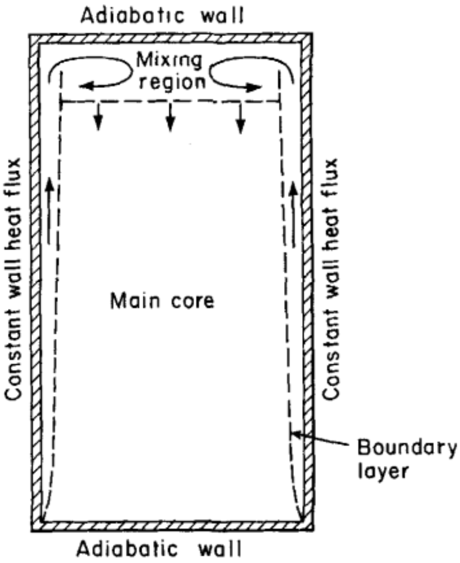
Adiabatic wall
Mixing region
Main core
Constant wall heat flux
Constant wall heat flux
Boundary layer
Adiabatic wall

Figure 2.6: Three regions for natural convection within a vertical cylinder at constant heat flux (Evans et al., 1968)

Convective heat transfer accounts for a large proportion of the overall heat flow. An experimental and lumped 1D model of transient natural convection in a vertical cylinder is presented by Evans et al. and Drake (Drake, 1966; Evans et al., 1968). The experimental model is filled with water. Based on the experimental observations, under constant heat flux at the side walls, the system was divided into three regions: a mixing region at the top, a stratified sinking central core, and a boundary layer rising at the heated wall as in Figure 2.6. The axial temperature distributions from the experiment and 1D numerical model are as Figure 2.7. It can be seen that the stratified mixing region in Figure 2.6 is characterized by high temperatures. The computed results show good agreement with the experimental results in the middle part. Related momentum and energy equations for these three regions are given to describe the temperature gradient during the process. By employing an appropriate technique for

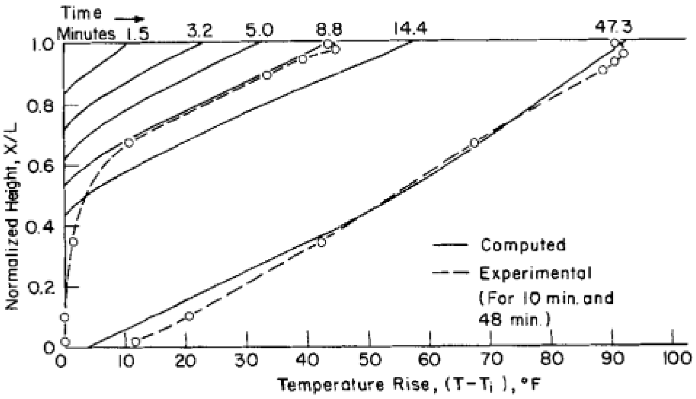

Figure 2.7: Axial temperature distributions for natural convection within a vertical cylinder with constant heat flux (Evans et al., 1968)

converting constant heat flux boundary conditions into isothermal boundary conditions, it becomes feasible to derive a theoretical model to describe the heat transfer within surge vessels with other types of boundary conditions for heat transfer than constant heat flow. In Evans' (Evans et al., 1968) article, Equation 15 is wrong and should be as shown in Equation 2.20.

$$\frac{\mathrm{d}E^*}{\mathrm{d}X} = 1 - 5\left(\frac{N_{Pr}}{60}\right)^{2/5}\left(\frac{10}{4/5 + N_{Pr}}\right)^{1/5}(E^*M^*)^{1/3}\theta'_\infty \tag{2.20}$$

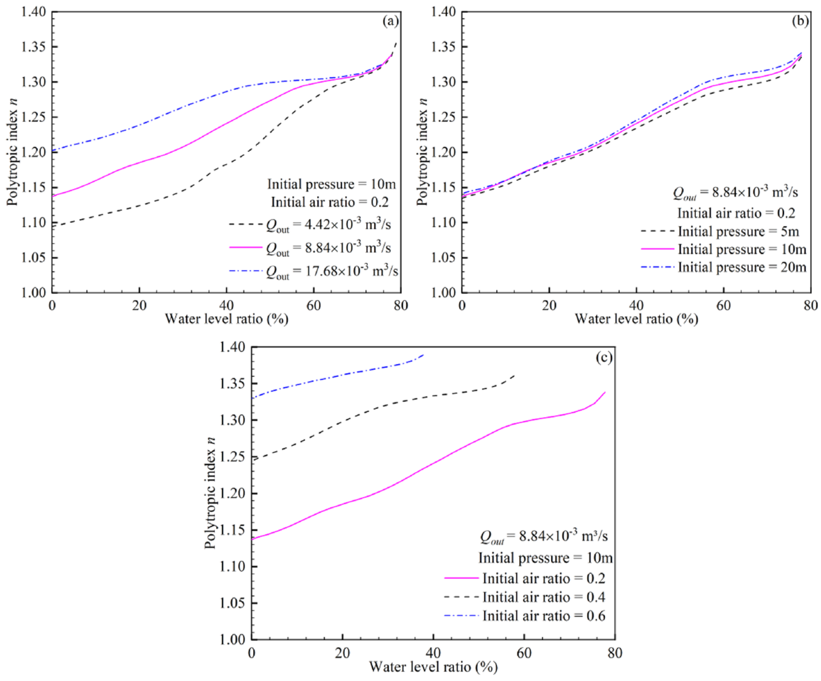

Figure 2.8: Polytropic number changing during the expansion as (a) water flow rate, (b) initial pressure, (c) initial air ratio (Chen et al., 2024a)

In addition to mathematical analysis, Chen and Mozayeni (Chen et al., 2024a; Mozayeni et al., 2020) used the CFD (computational fluid dynamics) method to simulate the heat transfer during the process.

The volume of fluid (VOF) method and standard $k-\varepsilon$ turbulence model are used to solve the momentum and energy equations of the air and water in the vessel. The simulation results of the pressure and temperature are substituted into Equation 2.21 to calculate the polytropic number for evaluation, as shown in Figure 2.8. Equation 2.21 is from polytropic Equation 2.7.

$$n = \frac{\ln(\frac{p_2}{p_1})}{\ln(\frac{V_1}{V_2})} \tag{2.21}$$

Where, p_1 and V_1 are the pressure and volume at the previous time step, p_2 and V_2 are the pressure and volume at the next time step.

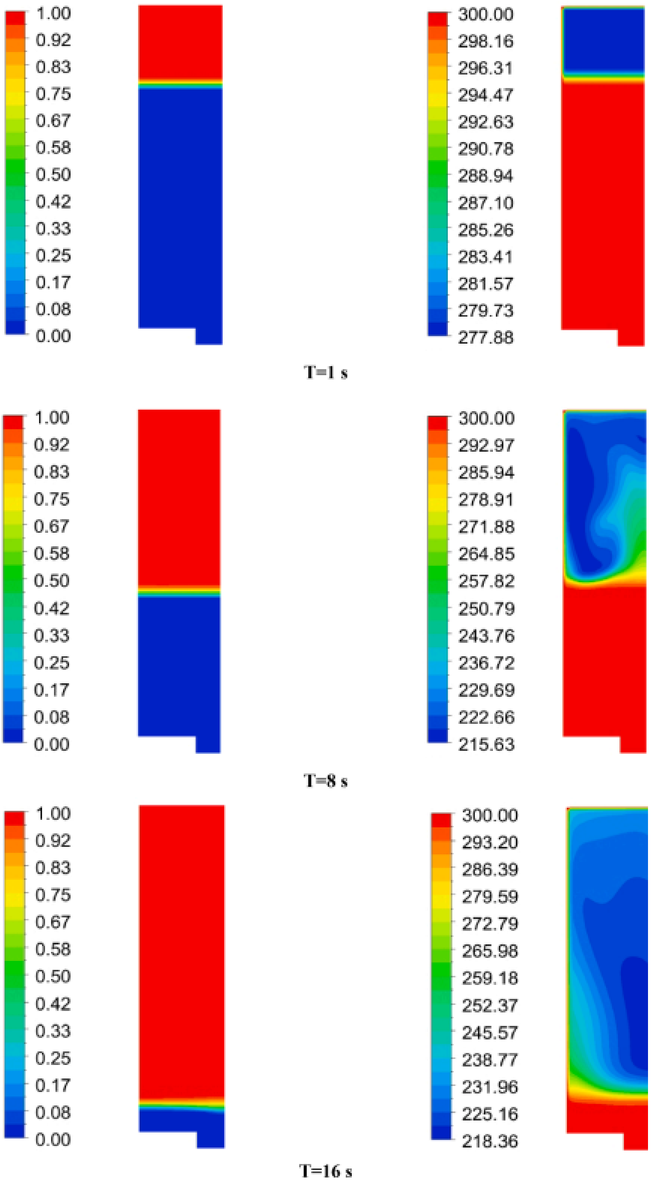

Figure 2.9: Phase (left) and temperature (right) contours in 2-phase CFD simulations (Chen et al., 2024a)

It can be observed that the polytropic number starts near adiabatic conditions (n = 1.4) at the beginning

of the expansion and then gradually decreases to approach isothermal conditions (n = 1.0). The inlet and outlet water flows, initial pressure and initial water level affect the thermodynamics of the air.
Figure 2.9 shows the 2-phase CFD simulation results of the phase and temperature contour. From the figure, it can be observed that in this multi-phase simulation, the expansion of air results in a significant temperature drop to a very low level. Meanwhile, the temperature of the liquid phase remains essentially constant and stable, the same as that of the wall. Therefore, in this study, the influence of the liquid phase is ignored, and only the air is considered as the subject of investigation.
Haakh and Veit (Haakh, 2022) conducted detailed experiments and thermodynamic analyses of the expansion and compression processes of air inside a surge vessel. The study provides comprehensive measurement data on internal air pressure, water level, air temperature, humidity, and temperatures on both the inner and outer sides of the vessel walls. The experiments were performed under high-pressure conditions, with the absolute pressure reaching up to 31 bar. Figure 2.10 shows the principle diagram of heat exchange during the expansion (decompression) process. It shows that as the temperature inside the vessel decreases during expansion, water may condense or even freeze. Simultaneously, the walls transfer heat to the internal air. Figure 2.11 illustrates the changes in internal energy, work done, and heat transfer during the air expansion process. It shows that internal energy initially decreases during the expansion process and then increases.

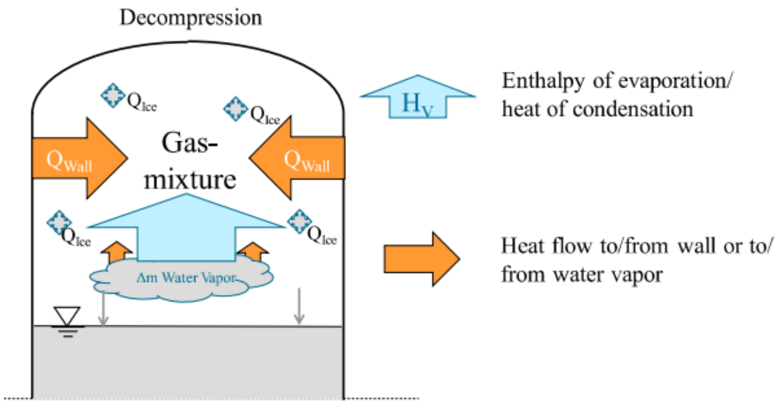

Figure 2.10: Principle diagram of exchanged heat quantities (Haakh, 2022)

Overall, the understanding of the different heat transfer processes and the heat transfer term in the RHT model needs to be improved. The majority of these methods involve comparison solely with the polytropic index 1.0 and 1.4, lacking direct comparison with experimental data. Consequently, the accuracy of the optimized RHT model remains unevaluated. Therefore, further refinement of the model and comparison with experimental and numerical results are needed. Furthermore, it is necessary to investigate the actual flow within the vessel, the temperature distribution, and the heat transfer rates, and to validate the assumptions and results related to these factors. The CFD method will be used to simulate the heat transfer process.

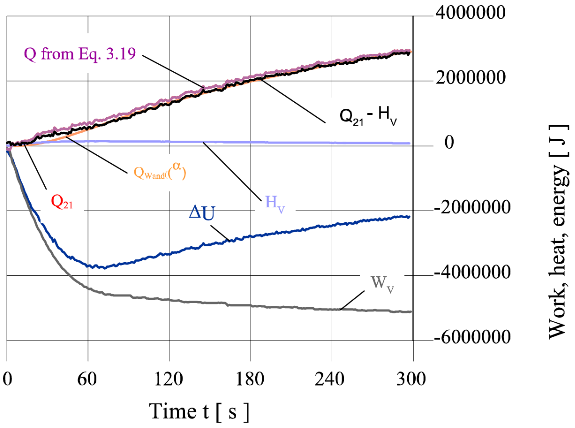

Figure 2.11: Calculated internal energy U, volume work W, and heat transfer Q change for the expansion process from experimental data (Haakh, 2022)

2.5. Research Approach

Based on the literature study discussed in this chapter, this section breaks down the targets outlined in the introduction into specific sub-goals.

1. Obtain analytical estimates of the different contributions to the total heat transfer and combine them with the RHT model

   -Quantify the contribution of each heat transfer term, including convection, radiation, and condensation.

   -By comparing each term and quantifying the work performed throughout the entire process, the dominant terms can be determined.

   -Subsequently, integrate the calculated dominant terms into the RHT model.

2. Use the CFD method to simulate the process of heating of air in a vessel after expansion of air, and possibly during the expansion, for heat transfer analysis

   -The air pocket inside the surge vessel is taken as a separate subject of study. The heat transfer modes and fluid behavior are being analyzed under both expanding and non-expanding conditions.

   -To minimize trial-and-error computational time and investigate heat transfer characteristics in the surge vessel at low Reynolds/ Rayleigh numbers, an initial simulation using a scaled-down computational model is conducted.

   -Subsequently, a full-scale computational model is to be employed to more accurately investigate the heat transfer behavior, thereby getting more comparable results to the experiment measurements.

3. Find a robust relation to describe the thermodynamics of the surge vessel, improving the 0-D model in a hydraulic software[1] by Deltares

   -Compare the simulation results with the RHT model, a 0D numerical model, and experimental measurement data. Then, attempt to derive the relevant RHT formula for the target surge vessel to represent the heat transfer process inside.

---

[1] WANDA is a software developed by Deltares that can calculate the 1-dimensional steady and transient flows of fluids inside pipeline networks.

3

Research Methodology

In Chapter 3, an overview of the research methodology is provided, including the physical model, the mathematical calculations, and the computational models, which are divided into a scaled small-size model and a full-scale model. This chapter also details the boundary conditions applied in the CFD simulations and the solver settings.

3.1. Physical Model

To get a better comparison with the experimental data, the physical model is defined based on the dimensions of the surge vessel of the alpha loop pipe flow facility at Deltares. The focus of the study is only on the air pocket within the surge vessel. The air volume and volume change are consistent with the experimental setup.

Before the measurements begin, gas is injected into the surge vessel to compress the air, and a waiting time is taken to reach thermal equilibrium. In the experimental measurements, water is drained from the bottom pipeline by opening the valve at the bottom of the vessel. Once the water reaches the desired level, the valve is closed, and the water level remains constant. To investigate the heat transfer modes, simulations were conducted for both the expanding and non-expanding conditions (i.e. after expansion), corresponding to scenarios with a moving bottom surface and a stationary state. The expanding simulation spans the entire process of the experiment, monitoring the expansion of the air region. After the expansion, the system remains static for a period to observe the heat transfer behavior. The non-expanding simulation begins once the expansion stops and the water level stabilizes. It focuses on heat transfer under stationary conditions. Figure 3.1 shows a schematic diagram of the expanding domain size. The effect of the flanges and outlets is neglected in the physical model due to its minor influence on the flow. The rounded top of the vessel is approximated to be a cylinder top. Hence, a cylinder with 1.908m in height and 2.5m in diameter is used as the initial domain for the expanding simulation; a cylinder with 3.299m is used for the non-expanding simulation.

Figure 3.2 shows the differential pressure data from the experimental measurements. The differential pressure is the pressure of the water in the surge vessel, which is used to calculate the pressure head.

Using this data, the change in the water level, then the height variation of the air pocket, can be calculated using Equation:

$$h = \frac{\text{Differential pressure}}{\rho g} \tag{3.1}$$

Where, h is the pressure head, namely the water level; ρ is the water density; g is the gravitational acceleration.

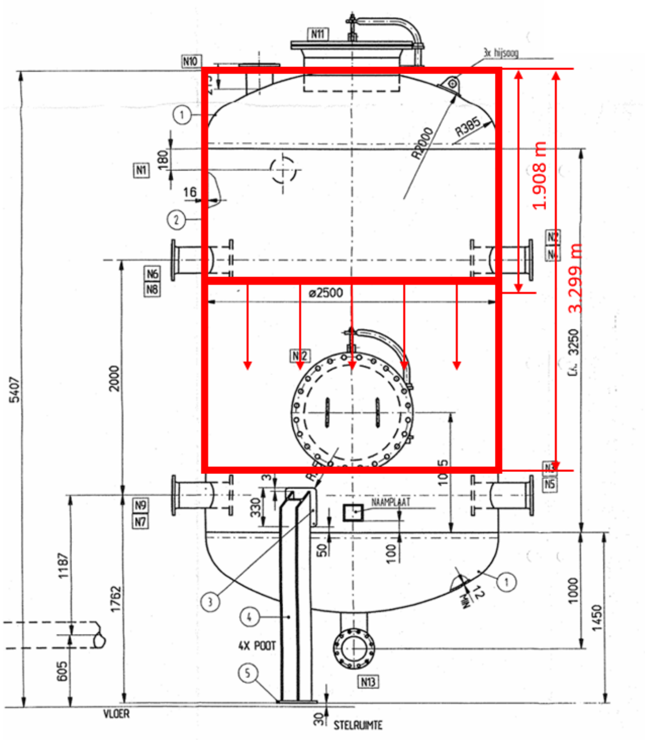
N11
N10
3x hijsoog
1.908 m
3.299 m
R2000
R385
N1
180
16
N6
N8
ø2500
N2
N5
N9
N7
330
NAAMPLAAT
50
100
1000
1450
3250
5407
2000
1187
1762
605
4X POOT
N13
VLOER
30
STELRUIMTE

Figure 3.1: Schematic diagram of the experimental surge vessel expanding

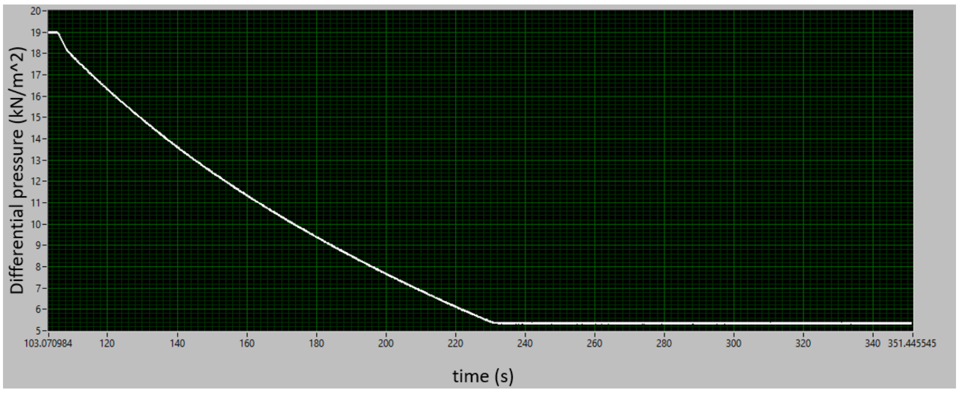

Figure 3.2: Measurement data from the differential pressure sensor in the experiment case 1

The temperature in the simulation is monitored at locations where temperature probes are placed in the experimental measurement. There are 25 probes at the upper part of the vessel, 20 so-called K-type, and 5 so-called T-type thermocouples. K-type thermocouples typically consist of nickel/aluminum alloy and nickel/chromium alloy and are suitable for measuring a wide range of temperatures. T-type thermocouples are known for fast response time and good accuracy. They are made of copper and suitable for measuring low temperatures. An aluminum frame supporting the probes is placed inside the vessel.

The probes are evenly placed on the vertical arms of the frame with the frame center at the vertical center line of the cylinder. The vertical location of the lowest probes is at the same level as at the center line of the topmost flanges in the vessel. The vertical space between each row of probes is 0.2 m. Figure 3.3 shows a schematic diagram of the locations of the probes in the measurement. Figure 3.4 shows the actual distribution of thermocouples in the experimental setup, with the red circles representing the location of the thermocouples.

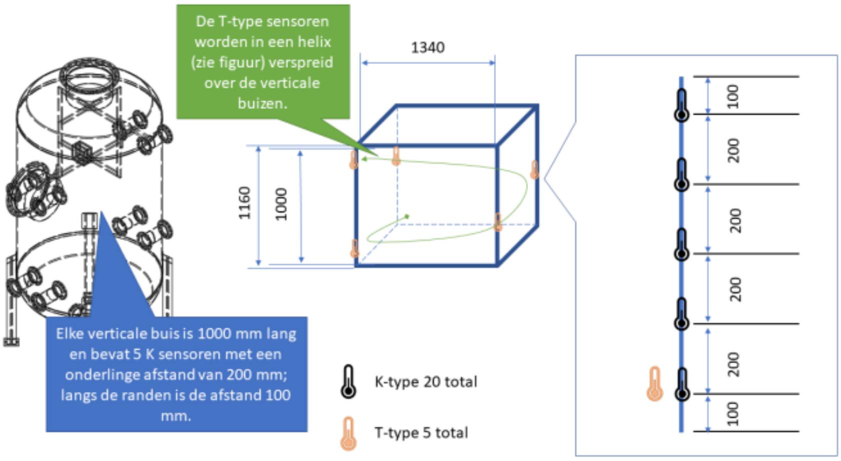
De T-type sensoren worden in een helix (zie figuur) verspreid over de verticale buizen.
1340
1160
1000
Elke verticale buis is 1000 mm lang en bevat 5 K sensoren met een onderlinge afstand van 200 mm; langs de randen is de afstand 100 mm.
K-type 20 total
T-type 5 total
100
200
200
200
200
100

Figure 3.3: Probe locations schematic diagram in the measurement (Zhang, 2022a)

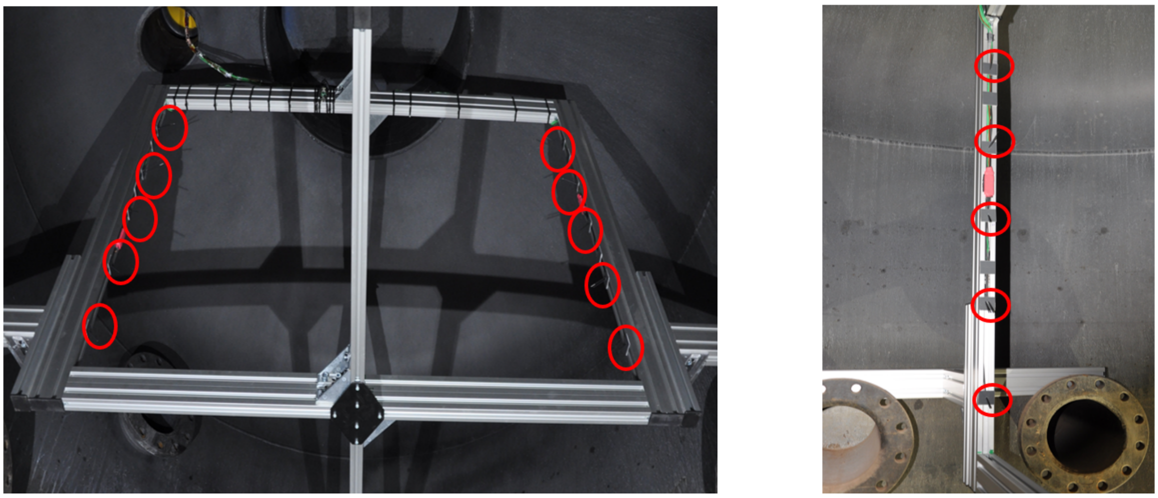

(a) (b)

Figure 3.4: Real thermocouple construction in the experimental setup (red circles: locations of the thermocouples)

3.2. Heat transfer processes

Based on the RHT model, this section aims to explore the values of each heat flux term in the energy balance equation 2.19. The derivation of the formulas required to calculate the contributions of different heat transfer processes in the air pocket will be described. Figure 3.5 shows the thermal resistance schematic for the actual experimental scenario. The air in the hall where the vessel is situated will transfer heat to the exterior wall of the vessel through convection. Subsequently, the exterior wall of the vessel will conduct the heat to the interior wall. The interior wall then transfers the heat to the air pocket inside the surge vessel through convection. Simultaneously, the water inside the vessel will transfer heat via convection as well.

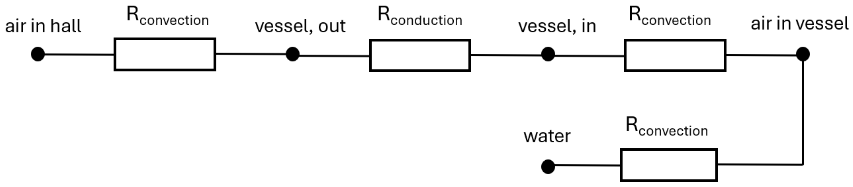

Figure 3.5: Thermal resistance schematic for the actual scenario

Since the convective heat transfer outside the surge vessel is estimated to be small, this external heat transfer is neglected in the calculations. The surge vessel wall temperature is assumed to be equal to the ambient temperature. Due to the relatively thin wall of the surge vessel (16 mm) and its metallic composition, heat conduction within the wall is neglected, so the wall temperature is considered uniform. Additionally, since the water temperature inside the surge vessel was not recorded, it is assumed that the water temperature is consistent with the ambient temperature. Consequently, the calculation only focuses on the heat transfer within the surge vessel, disregarding both the convective heat transfer outside the vessel and the internal conduction within the vessel wall. The simplified thermal resistance schematic is shown in figure 3.6. Detailed data and a quantitative analysis of each heat transfer term will be presented in Chapter 5.

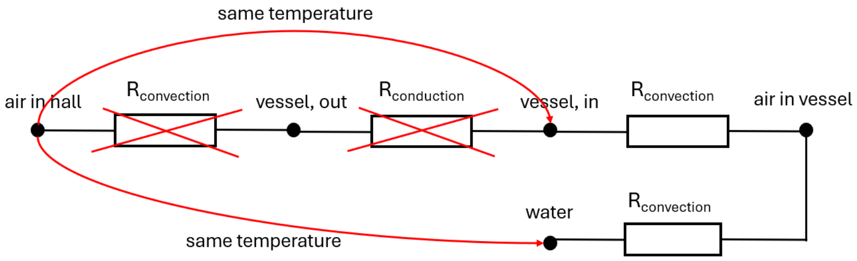

Figure 3.6: Simplified thermal resistance schematic for the simulation scenario

3.2.1. Convection

Since there is no forced airflow within the vessel, the heat transfer between the interior wall of the surge vessel and the air inside occurs through natural convection. Natural convection is driven by gravity. The air in contact with the wall of the surge vessel is heated and expanding, reduced in density, and this generates buoyancy, which drives the air to flow upward along the wall. This upward movement of heated air promotes the circulation of air within the vessel.

The convective heat transfer coefficient h can be determined using the dimensionless Rayleigh number (Ra) and Nusselt number (Nu) as mentioned in Section 2.4.2. The relationship between Ra and Nu numbers differs for horizontal and vertical surfaces. For the water level, the equations for a horizontal plate can be used. The ceiling of the tank introduces very small natural convection because its temperature is higher than the air, preventing the air below it from cooling. For the walls of the vessel, the equation for a vertical plate can be used.

After calculation of the convective heat transfer coefficients, the convective heat transfer $Q_{convective}$ between the vessel wall and the water surface and the air can be determined as follows:

$$Q_{convective} = h \cdot A \cdot (T_s - T_\infty) \tag{3.2}$$

where A is the surface area of the vessel wall and the water surface.

3.2.2. Condensation

As the temperature inside the vessel decreases, the relative humidity of the air increases, due to the fact that cooler air has a lower capacity to retain moisture. If the temperature drops sufficiently, condensation of water vapor will occur, releasing latent heat, which will subsequently transfer heat to the air within the vessel.

The saturation vapor pressure can be calculated using the Tetens equation (Wikipedia contributors, 2024), which is given by:

$$P_{sat} = 0.61078 \exp\left(\frac{17.27\,T}{T + 243.5}\right) \tag{3.3}$$

where, P is the saturation vapor pressure at temperature T (in Pa), T is the temperature (in °C).

Then, the vapor pressure of water can be determined using the following equation:

$$p_{vapor} = RH \times P_{sat} \tag{3.4}$$

where RH is the relative humidity of the air.

The amount of water vapor that is present in a kilogram of air can be calculated by (Oyj, 2013):

$$m_{water} = m_{air} \times \frac{M_{water}}{M_{air}} \times \frac{p_{vapor}}{p - p_{vapor}} \tag{3.5}$$

where the molar mass ratio $\frac{M_{water}}{M_{air}}$ is equal to 0.622.

The amount of condensed water that turns into mist can be calculated by multiplying the difference in relative water masses before and after expansion by the total mass of the air. The heat released during this condensation process is then calculated by:

$$Q_{condensation} = \Delta m_{water} \cdot \Delta H_{vap} \tag{3.6}$$

where the latent heat of vaporization H_{vap} is 2,260 kJ/kg for water.

3.2.3. Radiation

The radiant heat transfer primarily occurs between the inner walls of the container and the condensed liquid droplets in the air. The radiative heat energy can be calculated using the Stefan-Boltzmann law, which is:

$$q_{radiation} = \varepsilon \sigma T^4 \tag{3.7}$$

where ε is the emission factor and the Stefan-Boltzmann constant $\sigma = 5.67 \times 10^{-8} W/m^2 \cdot K^4$.
To estimate the heat absorbed by each droplet, it is important to account for both the radiation emitted from the container wall towards the droplet and the radiation emitted outward from the droplet itself. The radiation from water vapor is broken down into spherical droplets with a radius of approximately 1 µm. Then, the number of droplets can be calculated by:

$$N_{droplet} = \frac{\Delta m \text{ (from condensation)}}{m_{droplet}} \tag{3.8}$$

The radiative heat transfer can be calculated as:

$$Q_{radiation} = N_{droplets} \left(\varepsilon_{wall} A_{droplet} \sigma T_{wall}^4 - \varepsilon_{water} A_{droplet} \sigma T_{droplet}^4 \right) \cdot t \tag{3.9}$$

It is worth noting that the radiative heat can affect the temperature sensor readings as described in example 1.5 in Mill's book(Mills, 1999).

3.2.4. Work

The work done by the air during the expansion process can be calculated by:

$$W = \int P dV \tag{3.10}$$

3.3. Numerical model

This section outlines the development of the numerical model, with a focus on mesh generation. The mesh is a critical aspect that directly influences the accuracy and convergence of CFD simulations. The mesh is generated using Ansys ICEM software. In the scaled small-size model, a structured mesh was employed due to its ability to produce highly accurate results with efficient computation. However, in the full-scale model, an unstructured mesh was used. The choice of an unstructured grid was due to the complexities introduced by the larger geometry and the interaction with the mesh morphing model. Structured meshes were found to be incompatible with the mesh morphing model required for simulating dynamic behavior in the large-scale model. During the deformation of the structured mesh in the full-scale model, the residuals for the energy, momentum, and continuity equations rise sharply, leading to the simulation crash. Detailed information on this issue can be found in Appendix C.
Simulations were conducted at two different sizes to analyze airflow and heat transfer under different region sizes. For the low Rayleigh number scenario, the region size was set to one-tenth of the full scale of the vessel, resulting in different Rayleigh numbers, and is referred to as the ”scaled small-size” model in subsequent discussions.

For the full-scale model, the diameter of the model is 2.5 m, with the height varying from 1.908 m to 3.299 m. For the scaled size model, the diameter is 0.25 m, with the height varying from 0.1908 m to 0.3299 m.

3.3.1. Governing Equations

For fluid flow over a finite control volume, the governing equations are the conservation of mass, momentum, and energy.

Continuity equation:

$$\frac{\partial}{\partial t}\int_V \rho dV + \oint_A \rho \mathbf{v} \cdot d\mathbf{a} = 0 \tag{3.11}$$

Where t is time; V is the control volume; $\mathbf{a}$ is the area vector; ρ is the density; $\mathbf{v}$ is the velocity.

Momentum equation:

$$\frac{\partial}{\partial t}\int_V \rho \mathbf{v} dV + \oint_A \rho \mathbf{v} \otimes \mathbf{v} \cdot d\mathbf{a} = -\oint_A p\mathbf{I} \cdot d\mathbf{a} + \oint_A \mathbf{T} \cdot d\mathbf{a} + \int_V \mathbf{f}_b dV \tag{3.12}$$

Where p is pressure, $\mathbf{T}$ is the viscous stress tensor, and $\mathbf{f}_b$ is the resultant of body forces.

Energy equation:

$$\frac{\partial}{\partial t}\int_V \rho E dV + \oint_A \rho H \mathbf{v} \cdot d\mathbf{a} = -\oint_A \mathbf{q} \cdot d\mathbf{a} + \oint_A \mathbf{T} \cdot \mathbf{v} d\mathbf{a} + \int_V \mathbf{f}_b \cdot \mathbf{v} dV \tag{3.13}$$

Where E is the total energy, H is the total enthalpy, $\mathbf{q}$ is the heat flux.

Based on these continuity, energy, and momentum equations, the computations were completed using the models and solvers mentioned in Section 3.5.

3.3.2. Scaled Small-size

The scaled small-size model uses the structured mesh. Given the cylindrical shape of the model, the O-grid block was employed for mesh generation. The O-grid block produces a highly symmetric and uniform mesh, reducing numerical errors due to skewed cells.

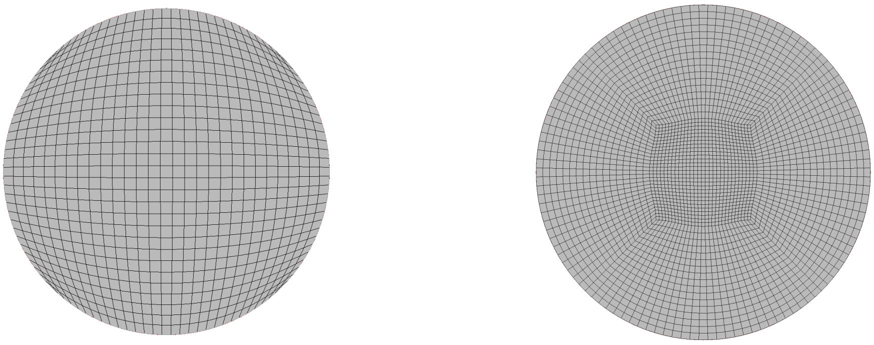

(a) Original Grid

(b) Grid with O-grid block

Figure 3.7: O-grid Demonstration

It modifies a single block into a 5 (2D) or 7 (3D) sub-block topology, as shown in Figure 3.7. It rearranges grid lines into an ”O” shape, effectively reducing skewness at the connection. Additionally, since the near-wall elements are now aligned normally with the wall, the O-block can efficiently capture flow details near the wall, improving the accuracy of boundary layer resolution.

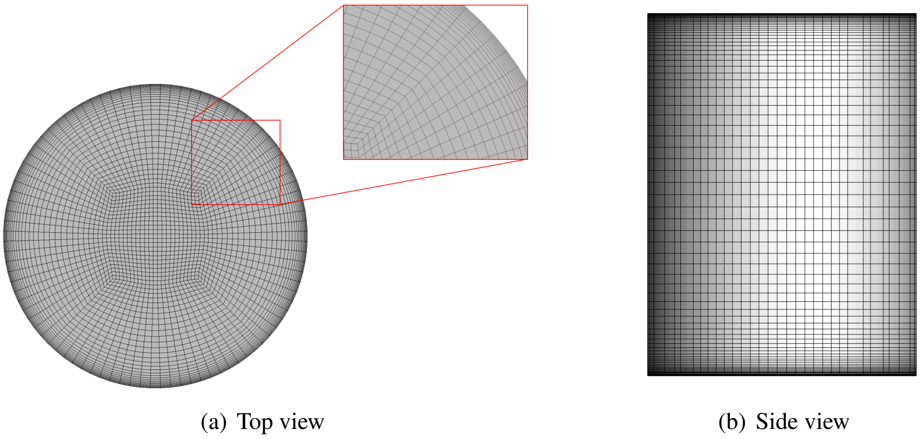
(a) Top view (b) Side view

Figure 3.8: Structured mesh of the scaled small-size model

The mesh for the scaled small-size model is shown in Figure 3.8. An exponential distribution law is used near the wall region to refine the mesh distribution from the boundary. The minimum boundary grid size is 0.0004 m on both the side and top/bottom surfaces, ensuring that the wall shear stress y+ values remain below 1. The wall y+ value is a dimensionless parameter that represents the distance from the wall in terms of viscous units. It can assess the resolution of the near-wall mesh in CFD simulations. The y+ value is defined as:

$$y^+ = \frac{y u_\tau}{\nu} \tag{3.14}$$

where, y is the distance to the nearest wall, u_τ is the friction velocity, ν is the kinematic viscosity of the fluid.

The Hexa mesh quality is calculated as the minimum value among the warping of the mesh (ANSYS, 2022). Warpage is normalized to a factor between 0 to 1, where 90 degrees is 0, and 0 degrees is 1. The mesh parameters for the scaled small-size numerical model are in Table 3.1.

Table 3.1: Mesh parameters for scaled small-size numerical model

Type	Scaled small-size
mesh number on radial direction	42
mesh number on vertical direction	80
element number	277242
wall spacing top and bottom	0.0004 m
wall spacing sidewall	0.0004 m
mesh quality	>0.7

3.3.3. Full-scale

The full-scale model uses the unstructured tetrahedron mesh as shown in Figure 3.9. The maximum mesh sizes are 0.04 m for the bottom and top surfaces, 0.07 m for the wall surfaces, and 0.1 m for the internal volume mesh. To enhance accuracy and precision, the prism boundary layer mesh is used near the boundaries. The boundary layers have a minimum height of 0.0002 m, consist of 20 layers, and have a height ratio of 1.2. The y+ number always remains below 1.

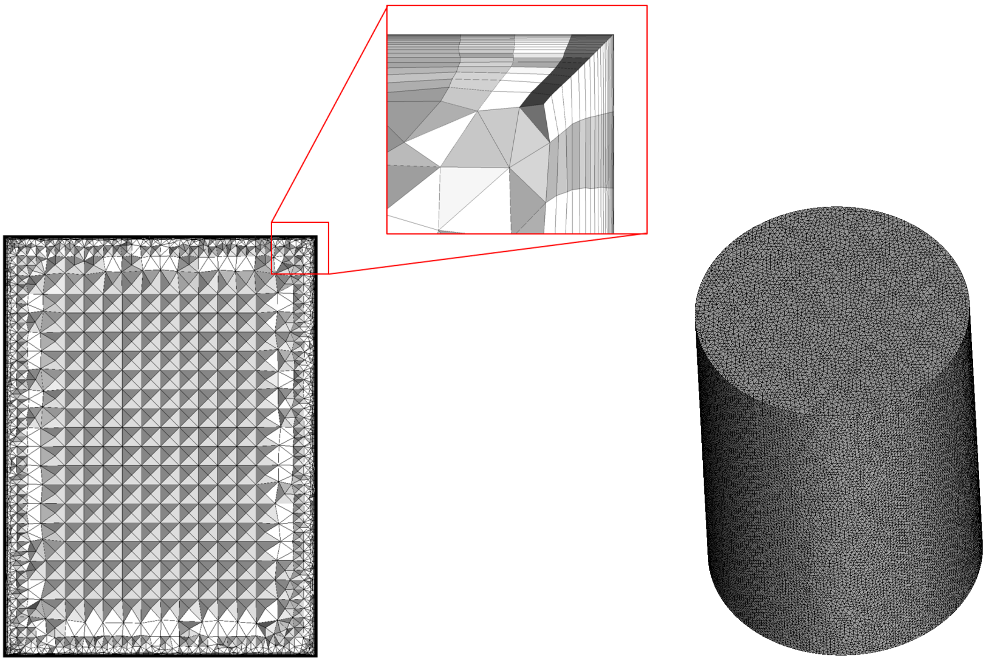

(a) middle cut plane (b) overall view

Figure 3.9: Unstructured mesh of the full-scale model

From Figure 3.10, the boundary layer on the side wall remains within the boundary layer mesh, indicating that the mesh is appropriate for capturing the boundary layer. Figure 3.11 shows the temperature profile of two horizontal line probes within a 0.03m range near the boundary. The dots represent points on the horizontal line probe, with every 8th point being selected from the set of probe points. The specific positions of the temperature probes are described in Section 2.2. From the temperature readings, the presence of the boundary layer can be observed, with the temperature near the wall being 288.44 K (wall temperature), and gradually decreasing towards the center. Outside the boundary layer, the temperature remains relatively uniform. The pyramid mesh quality is defined by the determinant. The Determinant is defined as the ratio of the smallest to the largest determinant of the Jacobian matrix, calculated at each node of the element. A value of 1 indicates a perfectly regular mesh element, while a value of 0 indicates an element that is degenerated along one or more edges. The prism quality is calculated as the minimum of the Determinant and Warpage.

The mesh parameters for the full-scale numerical model are in Table 3.2.

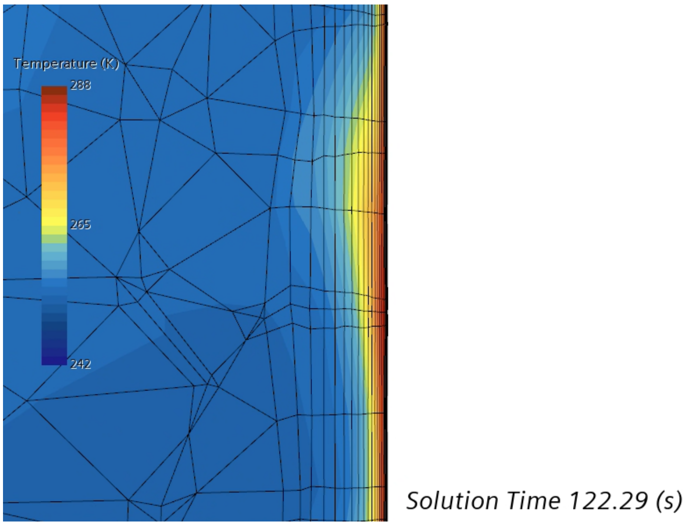

Figure 3.10: Mesh resolution in the boundary layer of the full-scale model at t = 122.29s

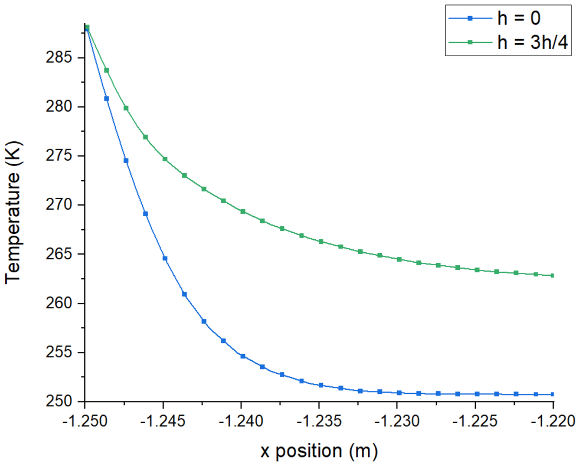

Figure 3.11: Temperature profile in the Boundary layer at t = 122.29s (dots: every 8th points on the horizontal line probe)

Table 3.2: Mesh parameters for full-scale numerical model

Type	full-scale
maximum mesh size top and bottom	0.04 m
maximum mesh size sidewall	0.07 m
maximum mesh size internal	0.1 m
minimum boundary layer mesh height	0.0002 m
number of boundary layer mesh	20
boundary layer mesh height ratio	1.2
element number	1515280
mesh quality	>0.55

3.4. Initial & Boundary Conditions

The initial temperature of the air domain is set to 288.44 K, with an initial gauge pressure of 0.746 bar and no initial velocity.

Figure 3.12 shows the sketch of the boundary conditions. All thermal boundaries are configured with isothermal boundary conditions with a temperature of 288.44 K. For shear stress, the boundaries are set to no-slip boundary conditions. In the expanding simulation, the bottom surface is translated using a User-Defined Function (UDF). The bottom surface deforms along the negative z-axis at a speed of 0.0112 m/s for 124.2 seconds, after which it remains stationary. For the scaled small-size model, the deformation speed is proportionally scaled according to the geometry, resulting in a speed of 0.00112 m/s.

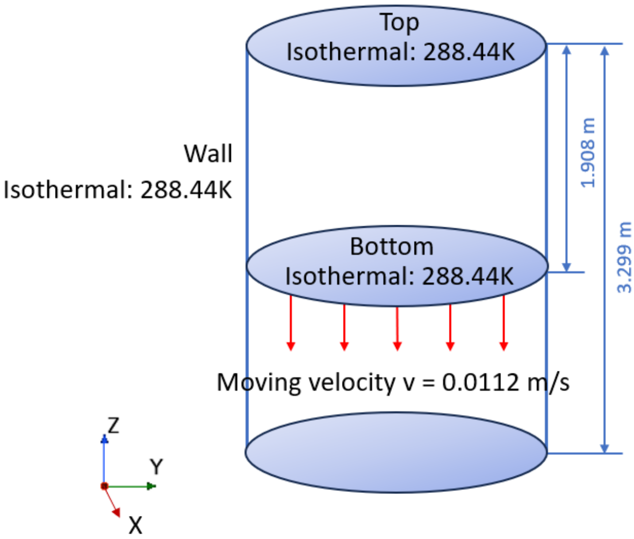

Figure 3.12: Sketch of the boundary conditions

The temperature, time, and movement speed data are all derived and modified from experimental data as shown in Appendix G.

3.5. Models & Solvers

In this section, the solvers and models used in the simulation are introduced to effectively capture the thermodynamic processes within the system. These models ensure an accurate representation of the physical behavior during the simulation. The selection of appropriate solvers and models is critical to achieving convergence and obtaining reliable results.

3.5.1. Gas Model

The air inside the vessel is approximated as compressible ideal gas. According to Equation 2.8, the ideal gas law describes the density as a function of temperature and pressure as Equation 3.15. Given that the air density continuously changes during the expansion process, a compressible fluid model is employed. The air properties are listed in Table 3.3.

$$\rho = \frac{p}{R_s T} \tag{3.15}$$

Where R_s is the specific gas constant.

Table 3.3: Air properties

specific heat of air	c_{air}	1006.76	$J/kg \cdot K$
dynamic viscosity	μ	1.760×10^{-5}	$Pa \cdot s$
kinematic viscosity	ν	1.81100×10^{-5}	m^2/s
thermal conductivity	k	0.0249	$W/m \cdot K$
thermal diffusivity	α	1.8315×10^{-5}	m^2/s
gravity	g	[0,0,-9.81]	m/s^2

3.5.2. Flow & Energy Model

The air in the vessel is under a high Rayleigh number, so the turbulence model is used. Turbulence significantly impacts the description of heat transfer within the vessel.

The turbulence model utilized is the WALE (Wall-Adapting Local-Eddy Viscosity) subgrid scale LES turbulence model. The LES model is chosen instead of the RANS model because it can capture a wider range of turbulence scales. It avoids the modeling uncertainties connected with the RANS model, providing more accurate and detailed flow predictions. Additionally, the WALE subgrid model captures near-wall turbulence without wall damping. It offers better numerical stability and reduced sensitivity to the value of the model coefficient than the Smagorinsky subgrid scale model.

The subgrid scale viscosity in the WALE model accounts for the effects of turbulence at scales smaller than the grid resolution, improving the accuracy of turbulence prediction. The WALE subgrid scale viscosity is:

$$\mu_t = \rho \Delta^2 S_w \tag{3.16}$$

Where, Δ is the length scale, S_w is the deformation parameter.

Length scale model limit is applied, meaning that the filter length $\Delta = \min(\kappa d, C_w V^{1/3})$, where $\kappa = 0.41$ is the von Karman constant, d is the wall distance, $C_w = 0.544$ is the model coefficient, and V is the cell volume.

The deformation parameter adapts the turbulence predictions to local flow conditions, enhancing the model's ability to capture the effects of varying flow deformations. The deformation parameter S_w is:

$$S_w = \frac{S_d : S_d^{3/2}}{S_d : S_d^{5/4} + S_d : S_d^{5/2}} \tag{3.17}$$

where S is the rate of strain computed from the resolved velocity field u. The tensor S_d is defined as:

$$S_d = \frac{1}{2}[\nabla v \cdot \nabla v + (\nabla v \cdot \nabla v)^T] - \frac{1}{3} tr(\nabla v \cdot \nabla v) I \tag{3.18}$$

Where I is the identity tensor.

The coupled solver is employed in the non-expanding model, while the segregated solver is used in the expanding model. This choice is due to the incompatibility of the coupled solver with the mesh deformation solver, detailed information is provided in Appendix D.

The segregated solver sequentially solves the mass and momentum conservation equations. It employs a pressure-velocity coupling algorithm, which ensures mass conservation in the velocity field by solving a pressure correction equation. The SIMPLE algorithm is used to control the solution update. The bounded-central convection scheme is employed for the momentum equation to control numerical oscillations and maintain stability. The segregated fluid temperature model solves the total energy equation with temperature as the primary variable. The second-order upwind scheme achieves as good as or higher accuracy than the first-order scheme. This scheme introduces linear interpolation of cell values on either side of the upstream or downstream face.

The coupled solver simultaneously solves the governing equations, directly coupling the continuity and momentum conservation equations to enhance robustness. This method improves convergence rates and yields more robust solutions for compressible flow (Siemens, 2021). The bounded-central convection scheme is also employed in the coupled solver for both the flow and energy.

3.5.3. Time Solver

The time solver employs a second-order implicit unsteady model, utilizing an adaptive time-step approach. This adaptive time-step model automatically adjusts the time step to optimize computational efficiency. The maximum time step is set to 0.01 s. The maximum inner iterations are set to be 10 for the scaled small-size model and 20 for the full-scale model. The simulation for the scaled small-size model runs for 150s, and 250s for the full-scale model. The solution time for the scaled small-size model is shorter because after 150s the air temperature in the vessel is near the ambient temperature. The target mean Courant-Friedrichs-Lewy (CFL) number is set to 0.85, with a maximum allowable CFL number of 0.95. The CFL number is a dimensionless parameter used to evaluate the stability and convergence of numerical simulations in fluid dynamics:

$$\mathrm{CFL} = \frac{U\Delta t}{\Delta x} \tag{3.19}$$

where, U is the velocity of the flow, Δt is the time step size, Δx is the spatial grid size.

3.5.4. Mesh Morpher Solver

For the expanding simulation, the mesh in the region was first scaled along the y-axis to the size before expansion in StarCCM+, which is from 3.365 m scaled down to 1.908 m. During the expansion process of the air in the vessel, the top surface is fixed, the bottom surface has displacement with a fixed velocity, and the side surface is set as floating. ”Floating” refers to the vertices on the boundary moving according to an interpolation of the displacement vector field. The displacement of the bottom surface is calculated using:

$$\mathrm{target\_coordinate} = \mathrm{current\_coordinate} + \mathrm{grid\_velocity} \times \mathrm{time\_step} \tag{3.20}$$

The morpher tolerance is set as 1e-7.

4

Validation

This chapter outlines an overview of the validation employed to ensure the accuracy and reliability of the computational results. It provides the reason behind the selection of the models and solvers used. The validation process begins with the ideal gas model to make sure the results are theoretically reasonable. Next, we validate the scaled small-size and full-scale models to assess the appropriateness of the grid, model, and solver. Additionally, analytical estimates of the different contributions to the total heat transfer are performed to verify the precision of numerical methods. The validation process also includes a simulation of another experimental setup to test the model's adaptability. Detailed validation of the simulation results against a 0D numerical model and experimental data will be discussed in the Results section.

The validation of the capability of the StarCCM+ software for buoyancy-driven flow and heat transfer analysis is in Appendix B. This validation is given by a Rayleigh-Benard convection case by Neumann (Neumann, 1990).

4.1. Ideal Gas Model

To validate the accuracy of the ideal gas model during the expansion process in the simulation software StarCCM+, the specific ideal gas constant R is calculated. Using Equation 3.15, the specific ideal gas constant can be calculated as $R_s = P/\rho T$. The values of the specific ideal gas constant were calculated for the scaled small-size model during the expansion process. The results are shown in Figure 4.1.

The specific ideal gas constant for air is 287 J/kg·K. As observed from the figure, the calculated ideal gas constant during the expanding process fluctuates within 1% of 287, indicating that the ideal gas equation is applicable in the simulation software StarCCM+.

Given that the gas expansion must occur between an isothermal and an adiabatic process, the lowest temperature achievable during adiabatic expansion was calculated to assess the reasonableness of the simulation results. During the adiabatic process, the polytropic index n is taken as 1.4. The pressure

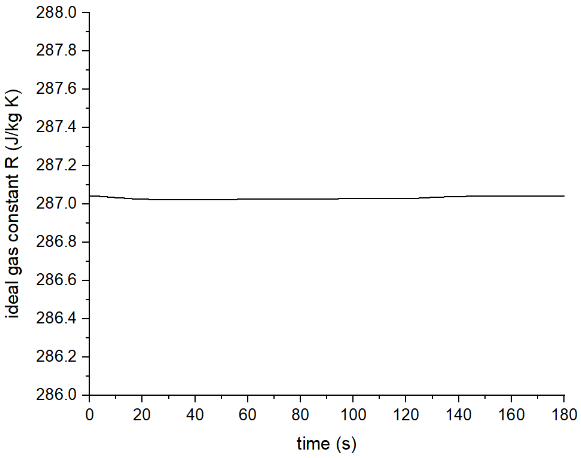

Figure 4.1: The calculated ideal gas constant R_s of the scaled small-size simulation

after expansion can be calculated using Equation 2.7 by:

$$p_{final} = p_{initial}(\frac{V_{initial}}{V_{final}})^{1.4} \tag{4.1}$$

Then, the number of moles of air inside the vessel can be calculated using Equation 2.8:

$$N = \frac{p_{initial}V_{initial}}{RT_{initial}} \tag{4.2}$$

The temperature after the adiabatic expansion process:

$$T_{final} = \frac{p_{final}V_{final}}{NR} \tag{4.3}$$

The calculated temperature after the adiabatic process is 231.71K. Therefore, the simulated temperature results should not drop below 231.71 K and should not exceed the initial temperature of 288.44 K. Since the scaled small-size and full-scale models have proportional volumes and the same initial pressure and temperature parameters, this temperature range is applicable to both models.

4.2. Mesh independence test

To ensure the accuracy and reliability of the computational results, a grid independence study is conducted for both the scaled small-size model mesh and the full-scale model mesh. This analysis aims to ensure that the chosen grid size provides sufficiently accurate results. For both models, 2 different mesh densities were tested separately, and the results were compared to assess the sensitivity of the solution to grid refinement.

4.2.1. Scaled Small-size

Based on the scaled small-size model, the overall mesh density was reduced. The number of mesh cells in the radial direction was decreased from 42 to 35, and the number of mesh cells in the vertical direction was reduced from 80 to 70. Consequently, the total mesh count was reduced from 277k to 180k. The

grid refinement ratio is higher than 1.1 to be differentiated from other error sources (Slater, 2021).
Using the k11 thermocouple and the volume-averaged temperature as comparison benchmarks, as shown in the figure 4.2. The overall fluctuations are of the same magnitude. Differences are expected for instantaneous local variables. The volume-averaged results from the two different mesh densities are nearly identical within 180 seconds. The thermocouple temperature variation between the meshes is minimal, and these differences are within an acceptable range, ensuring that they do not significantly impact the overall accuracy of the results. The consistency of temperature values in the coarser mesh indicates that the solution is entirely independent of mesh resolution, confirming that the selected mesh is suitable for the simulation.

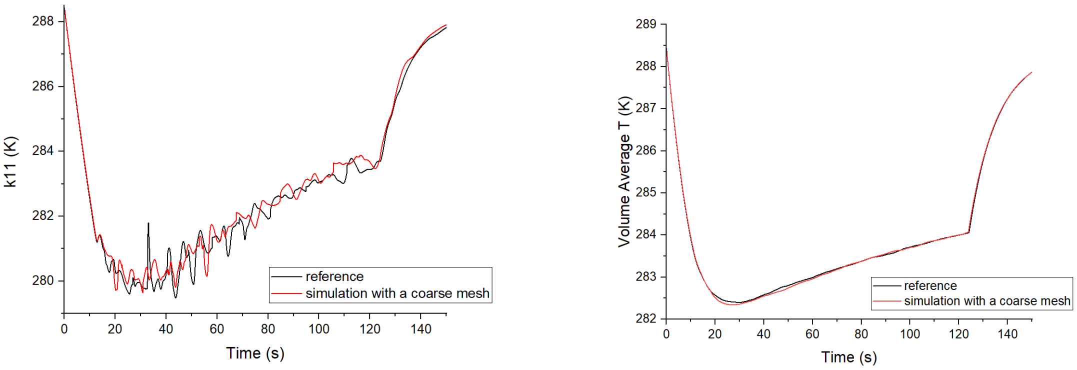

(a) k11 temperature (b) volume average temperature

Figure 4.2: mesh independence study results for the scaled small-size model

4.2.2. Full Scale

Based on the full-scale mesh model, the mesh within the body was refined, increasing the overall mesh density. The maximum mesh sizes are kept at 0.04 m for the bottom and top surfaces, decreased from 0.07 m to 0.06 m for the wall surfaces, and decreased from 0.1 m to 0.06 m for the internal volume mesh. The boundary layers are kept as before. The y+ number always remains below 1. Consequently, the total mesh count was increased from 1.5M to 2.4M.

Similarly, using the k11 thermocouple and the volume-averaged temperature as comparison benchmarks, as shown in the figure 4.3. It can be observed that the overall fluctuation amplitude of the two simulation results is the same. The difference between the K11 thermocouple and the volume-averaged temperature is minimal and within an acceptable range, ensuring that it does not affect the overall accuracy of the results. The consistency of the temperature values in the finer mesh indicates that the solution is independent of the mesh resolution, thus confirming that the selected mesh is suitable for the simulation.

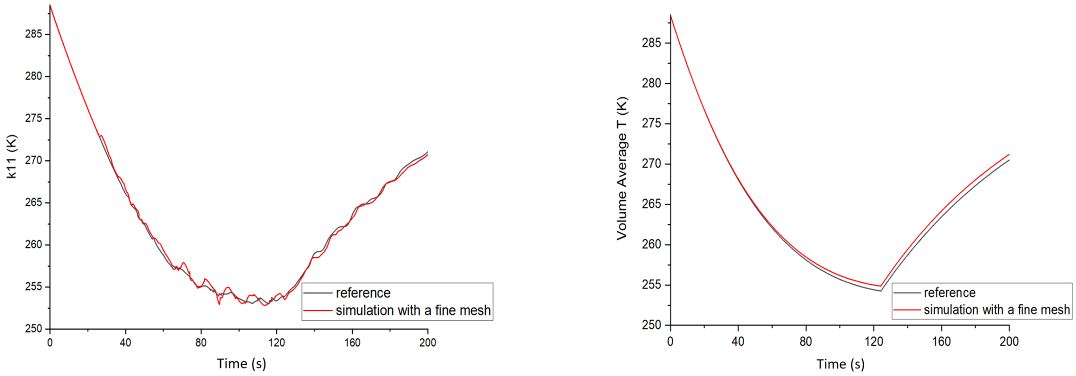

(a) k11 temperature (b) volume average temperature

Figure 4.3: mesh independence study results for the full-scale model

4.3. Models & Solvers

This section presents the validation of the selected model and solver configurations to ensure their suitability for the simulations. Various turbulence models, initial conditions, and numerical solvers are tested to determine whether the results are dependent on the specific choices of these computational settings. By comparing the outcomes under different configurations, we assess the robustness of the simulation results and ensure that the results are not significantly affected by the selected model or solver. This analysis confirms the reliability and consistency of the computational approach.

Due to the lower computational cost of the scaled small-size model and the better alignment of the full-scale model with experimental results, validation analyses using different models and solvers were conducted on both the scaled small-size and full-scale models.

4.3.1. Scaled Small-size

Initial Temperature Field

In the simulations, the initial temperature condition is set to a uniform temperature of 288.44 K, consistent with the temperatures of the walls and the top and bottom surfaces.

In the experiment, the thermocouple temperature at different heights was not identical but instead exhibited a temperature difference of approximately 1.5 K, as shown in Figure 4.4. After averaging the temperatures from the thermocouples at each height, a linear fit was performed by $T_{initial} = 12.716z + 286.23$ as shown in Figure 4.5. Where z is the height. This temperature function is applied to the simulation as the initial condition, with all other settings remaining consistent with the reference simulation.

Reynolds-averaged Navier–Stokes (RANS) Turbulent Model

The validation utilized the realizable $k - \varepsilon$ turbulence model. All other settings remain consistent with the reference simulation. The $k - \varepsilon$ model solves transport equations for turbulence kinetic energy (k) and its dissipation rate (ε) to estimate the effects of turbulence on the mean flow. 2-layer all y+ wall treatment is applied for RANS model simulation.

The RANS turbulent heat flux term, that is presented in the mean energy equation in the RANS model,

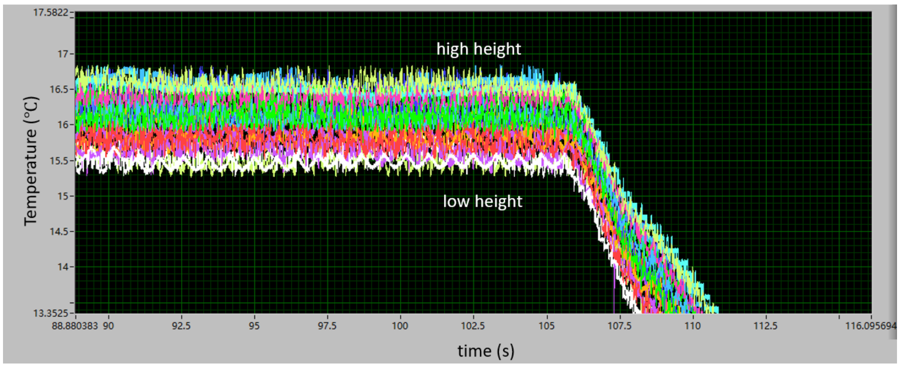

Figure 4.4: Initial thermocouple temperatures in the experiment case 1

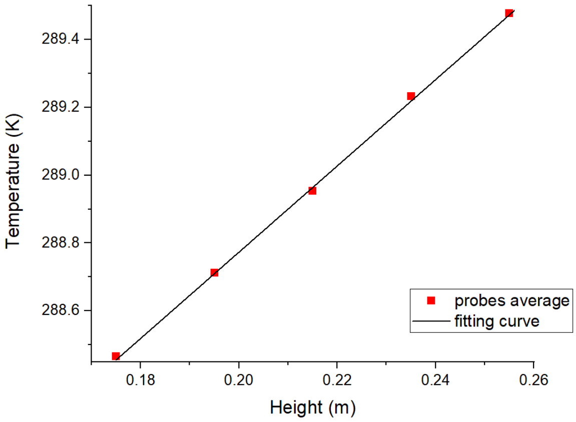

Figure 4.5: Linear fit for probes average temperature at each height for the experiment case 1

is modeled by (Ortiz and Koloszar, 2023):

$$\overline{u_i'T'} = -\alpha_t \frac{\partial \overline{T}}{\partial x_i} \tag{4.4}$$

Where, $\overline{u_i'T'}$ is the turbulent heat flux, α_t is the turbulent thermal diffusivity.
The heat flux is computed from the mean temperature field $\frac{\partial \overline{T}}{\partial x_i}$, which is small in the RANS model. Therefore, the heat transfer from the bottom in the surge vessel case will likely be underpredicted. Figure 4.6 shows the comparison of bottom heat transfer between the RANS and LES models. It can be observed that the heat transfer calculated by the RANS model is relatively lower after 10 seconds, with a difference of approximately 0.25 to 0.5 W, so 11% to 21%.

Figure 4.7 illustrates the temperature field results from the RANS and LES models at 47 seconds. The Realizable $k - \varepsilon$ RANS model shows a smoother temperature distribution near the bottom surface and within the vessel. In contrast, the LES model reveals a more variable temperature field with noticeable temperature gradients and fluctuations. The LES model provides a clearer depiction of how turbulence affects the temperature distribution.

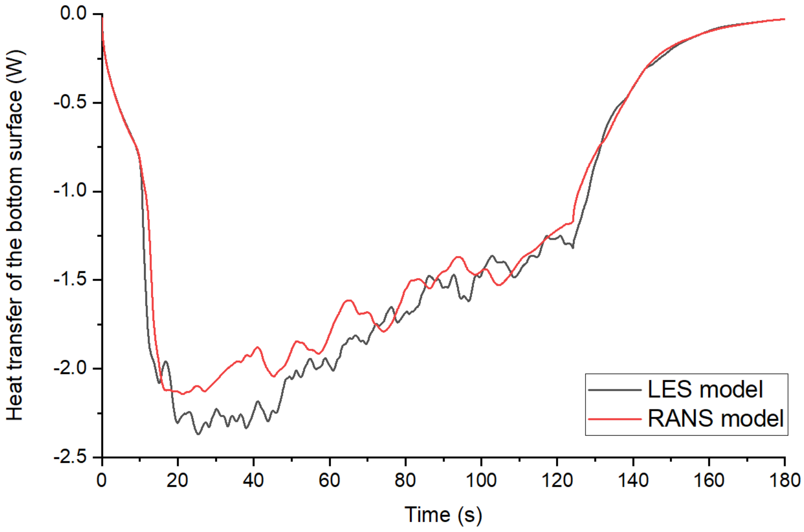

Figure 4.6: Heat transfer of the bottom surface comparison between the RANS and LES model for the scaled small-size model

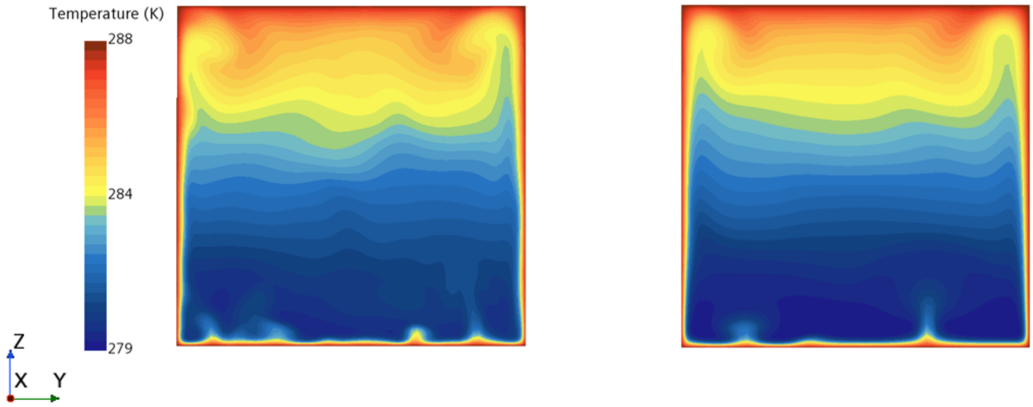

(a) LES model at t = 47s

(b) RANS model at t = 47s

Figure 4.7: Results compared between the LES model and the RANS model for the scaled small-size model at t = 47s

SIMPLE Consistent (SIMPLEC) Solver

Compared with the SIMPLE solver, the SIMPLEC solver assumes velocity corrections in neighboring cells are equal to those at the central cell, leading to a different pressure correction equation (Siemens, 2021). SIMPLEC implicitly incorporates pressure under-relaxation related to time-step size and velocity under-relaxation within the pressure correction equation. The deeper convergence is ensured within a time step than the SIMPLE solver.

Lower Energy Residual Settings

Setting a lower energy residual stopping criteria during the validation process can enhance the accuracy and convergence of the simulation. A lower residual threshold requires the solution to achieve finer numerical precision, thereby ensuring a stricter adherence to energy conservation. This approach helps to minimize numerical errors and improve the reliability of the simulation results. The original minimum residual value was approximately between 1e-5 and 1e-6. The minimum residual value is set to 1e-8. All other settings remain consistent with the reference simulation. The residual results are shown in Figure 4.8. It is worth noting that after reducing the residual value, the calculation time is significantly increased by about four times.

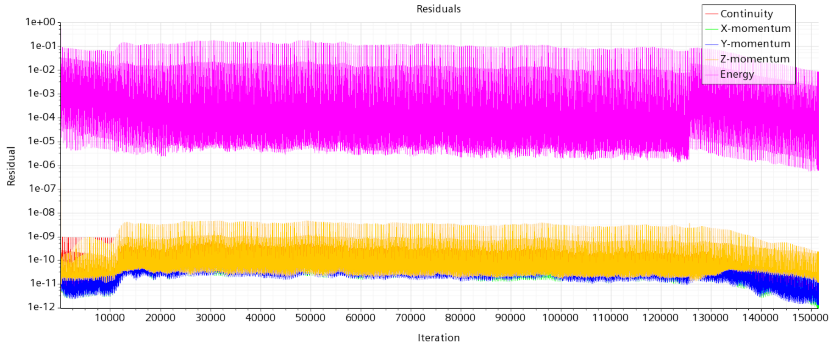

(a) reference residuals

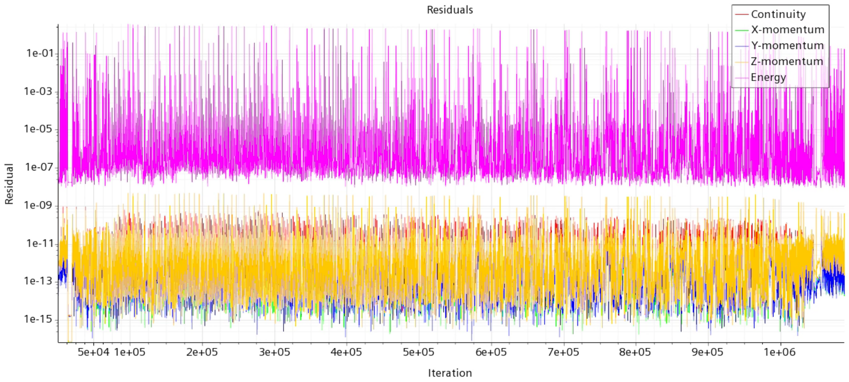

(b) residuals with lower energy residual settings

Figure 4.8: Residuals compared after the lower energy residual settings for the scaled small-size model

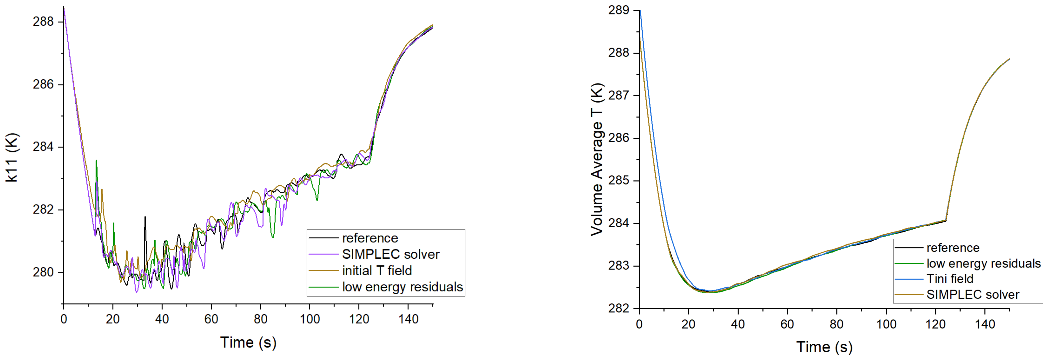

(a) k11 temperature (b) volume average temperature

Figure 4.9: models and solvers results comparison for the scaled small-size model

Results

Similarly, using the k11 thermocouple and the volume average temperature as comparison benchmarks, the results for the three scenarios—initial temperature field, SIMPLEC solver, and lower energy residual—are compared with those from the reference simulation. The comparison results are shown in Figure 4.9. The figure shows that the temperature results for each scenario are similar, indicating that the initial conditions, models, and solvers used are both reasonable and accurate.

4.3.2. Full Scale

Initial Temperature & Velocity Field

In the experiment, water was first put into the surge vessel, and then the air was pressurized until the air temperature stabilized. The experiment was then initiated. As a result, the initial conditions of the experiment included a higher stratified temperature field, as shown in Figure 4.4. Additionally, there might have been some initial velocity fields in the air that were not monitored during the experiment. These initial velocity fields could influence the early stages of the simulations, introducing complexities. Therefore, this subsection simulates the velocity and temperature fields before the start of the experimental measurements. These fields were then used as initial conditions for the expansion simulation to validate the necessity of having initial velocity and temperature fields.

To investigate the impact of initial temperature and velocity fields on the simulation results, this subsection sets the initial air temperature of the volume to 295K. The initial air pressure is calculated using the volume, temperature, and molar mass of air through the ideal gas equation, resulting in approximately 179.23 kPa. In the simulation, the model remains still.

The simulation is set to stop when one of two conditions is met:

- The volume-averaged pressure reaches the initial pressure value that was measured in the experiment.
- The average temperature of the thermocouples located at the highest height reaches the average temperature recorded by the highest thermocouples in the experiment.

These conditions ensure that the simulation accurately represents the physical setup and reflects the influence of initial conditions on the results. The simulation reached the pressure stop condition after running for 354 seconds. Figure 4.10 shows the temperature contour and velocity vector field when the simulation stops. It can be observed from the results that, under the initial experimental conditions, there was indeed a low-velocity field and an approximately linear temperature distribution within the air inside the vessel. The maximum velocity is about 0.277 m/s.

The temperature readings from the thermocouples in the simulation were compared to the initial experimental temperature, as shown in Figure 4.11. The x in the plot represents the average value of different thermocouples at the same height. The comparison reveals that the simulated temperatures are approximately 0.2K different from the initial experimental temperatures, which is negligible.

Then, the same expansion simulation is carried out as the full-scale expanding simulation. All other parameters and settings except for the initial conditions remain consistent. The full-scale simulation

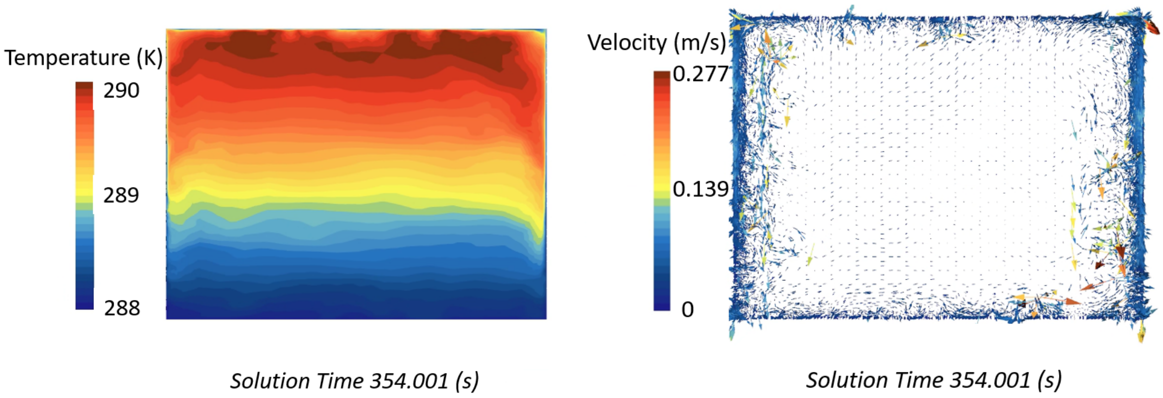

(a) temperature contour

(b) velocity vector field

Figure 4.10: Initial temperature and velocity field results under experimental conditions

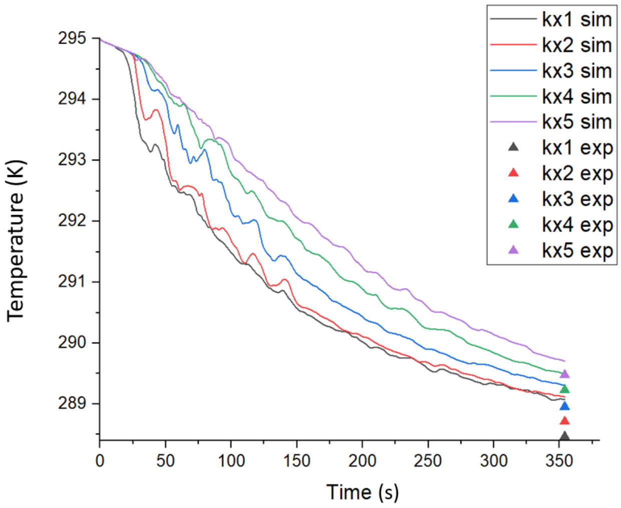

Figure 4.11: thermocouple average temperature in the initial field compared with experimental initial temperature (x in the name represents the average value of different thermocouples on the same height)

has uniform initial conditions with a temperature of 288.44 K, an absolute pressure of 175,892.6 Pa, and zero initial velocity.

A temperature comparison was made using 5 thermocouples from each of the various heights, alongside the volume-averaged temperature, as shown in the figure 4.12. The comparison shows that the thermocouple temperature readings and trends remain nearly consistent with the full-scale simulation, with a difference in the volume-averaged temperature of less than 0.1K. Therefore, it can be concluded that the initial velocity and temperature fields have a negligible impact on the simulation results. This suggests that even if there is some deviation in the initial temperature and velocity fields, the accuracy of the final results is not significantly affected, thereby confirming the robustness and reliability of the simulation.

Dome Volume

As shown in Figure 3.1, the prototype of the surge vessel has a dome-shaped top. In the simulations, this was approximated as a horizontal cylindrical top surface. There is a volume difference between the

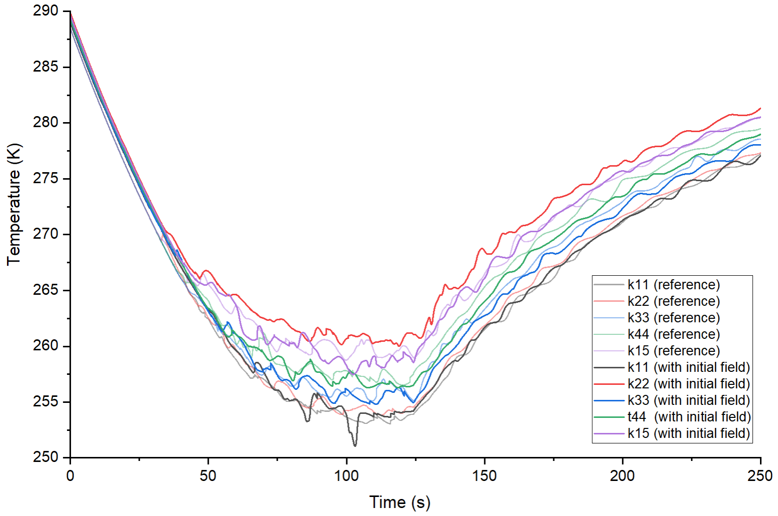

(a) probes temperature

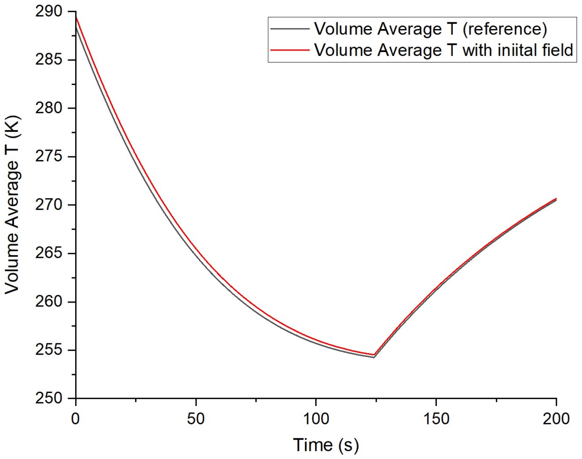

(b) volume average temperature

Figure 4.12: temperature comparison with the initial temperature and velocity field

cylindrical volume and the dome volume, with the dome's volume being smaller. It is approximately 1.5 square meters by calculation (South, 2023). This volume difference is determined by the volume of the hatch at the top. To simplify the model, this volume difference was converted into a height difference for the cylinder, resulting in an approximate height difference of 0.31 meters. Consequently, the initial height of the cylinder was adjusted from 1.908 meters to 1.603 meters, and the expanded height was adjusted from 3.299 meters to 2.994 meters. All other parameters remain unchanged, and the new geometric heights were applied to the simulation.

A temperature comparison was made using 5 thermocouples from each of the various heights, alongside the volume-averaged temperature, as shown in the figure 4.13. The results indicate that considering the dome volume leads to a greater temperature drop of approximately 2 K. This is attributed to the reduction in the sidewall surface area of the model, which decreases the heat transfer area and thus reduces heat transfer, resulting in lower temperatures. This demonstrates that the simulation results are sensitive to volume changes. However, the impact of the dome volume is not considered in the current simulation, and the specific reasons for this decision will be discussed in Chapter 5.

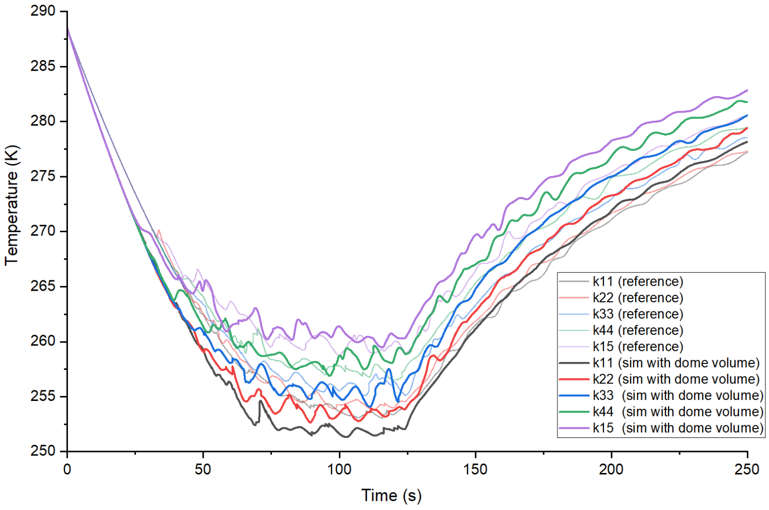

(a) probes temperature

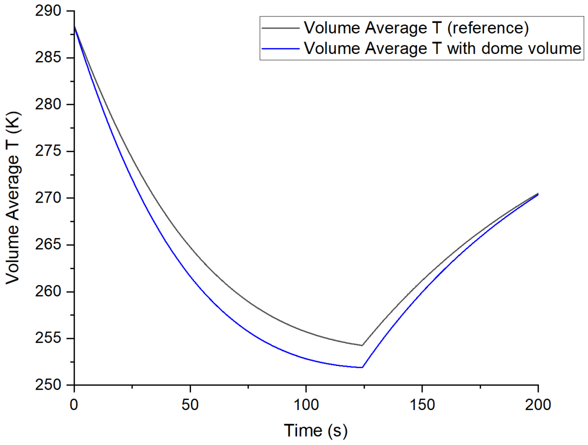

(b) volume average temperature

Figure 4.13: temperature comparison with the dome volume

4.4. Simulation of another experimental setup

The simulation for an additional experimental case is also performed for validation, the results of which will be thoroughly discussed in Chapter 5. By applying the model to a different experimental scenario, It is able to assess its predictive capabilities across varied conditions, thereby evaluating the model's generalizability and reliability.

This case will be referred to as ”case 2” in subsequent sections. The mesh used in the Case 2 simulation is consistent with the unstructured mesh described in section 3.3.3. The model has a diameter of 2.5 meters, and the height increases from 1.913 meters to 3.35 meters over 72.1 seconds. The initial temperature is 287.76 K, and the initial pressure is 322.13 kPa.

4.5. Experimental data & mathematical computations

Validating experimental data ensures that the simulation results are consistent with measurements, thereby confirming the simulation's accuracy. On the other hand, validating mathematical calculations with a 0D numerical model involves comparing the simulation results with computations involving correlations for different heat transfer contributions to ensure that the numerical methods used are correctly implemented and accurate. One needs to substitute both the analytical estimates of the heat transfer results and the simulation results into the RHT model equations to compute the difference between them. The detailed comparative results of these validations will be presented in Chapter 5.

5

Results

This chapter provides a detailed analysis of the simulation and calculation outcomes. The detailed settings and parameters of the simulation are in appendix A. The figures are primarily processed using OriginPro 2022 software.

First, the general fields are described based on the simulation results of the full-scale model, highlighting key thermal and flow patterns. Subsequent analysis addresses the scaled small-size model's fields, evaluating how scaling impacts the results and comparing them with the full-scale model. Validation is performed by comparing simulation data with experimental measurements and mathematical calculations. Additionally, results from an alternative experimental case are presented to further validate the accuracy and robustness of the simulations. Then, the experimental, simulation, and calculated results were incorporated into the RHT model to assess the accuracy of each result. This comprehensive analysis aims to validate the computational models and enhance the understanding of heat transfer dynamics within the surge vessel.

Only the expanding simulation for the full-scale and scaled small-size models will be discussed in this chapter. Detailed information about the non-expanding simulations will be provided in Appendix E. The summary of simulations is shown in Table 5.1.

As described in Section 3.3, the number of cells for the full-scale model is 1.5M, and for the scaled small-size model is 277k. The full-scale model was computed using 80 cores, taking approximately 4 days to simulate 250 seconds of physical time. The scaled small-size model was computed using 8 cores, taking approximately 1 day to simulate 150 seconds of physical time.

Table 5.1: Summary of simulations and locations in the thesis

Experimental Case	Simulations	Name in Text	Section
case 1	non-expanding full-scale model	same	Appendix E
	non-expanding scaled small-size model	same	Appendix E
	expanding full-scale model	full-scale	5.1
	expanding scaled small-size model	scaled small-size	5.2
case 2	expanding full-scale model	simulation in case 2	5.5

5.1. General Field Description of the Full-scale model

This section primarily presents the temperature and velocity fields of the full-scale model, along with the monitoring data at the thermocouple locations. These data illustrate the development of the flow field and heat transfer during the expansion of the surge vessel and its subsequent static state, providing insight into the heat transfer phenomena. For the full-scale simulation, the estimated maximum Rayleigh number (Ra) is 1.63×10^{11}, which occurs at the time when the expansion stops (t = 124.2 s). At the start of the expansion, the temperature difference between the air inside the vessel and the vessel walls is 0, resulting in an initial Ra number of 0. This indicates that during the expansion process, the airflow inside the vessel transitions from laminar to an intermediate state, eventually developing into fully turbulent.

5.1.1. Temperature Field

Figure 5.13 shows the temperature field images at different times, illustrating the complex interplay between temperature, time, and spatial distribution. The air expansion process lasts for 124.2 s. During the expansion, images are captured every 10 seconds, and after the expansion ends, images are taken every 25 seconds.

During the 250s process, the heat transfer within the surge vessel can generally be divided into three stages:

- Initial State and Early Cooling (t = 0s to t = 10s):
  The system appears to be in a relatively uniform thermal state at the start, with temperatures around 288 K. In the early stages, a slight cooling effect is already taking place due to the work done by the system. This cooling may not be immediately apparent due to the wide color scale used in the contour plots, which covers temperature variations.

- Rapid Cooling and Thermal Stratification (t = 10s to t = 124.2s):
  As time progresses from 10 seconds to 40 seconds, the effects of the expansion become evident. A cooling effect is observed, particularly in the central region of the air, where the temperature begins to drop. This cooling is a direct result of the work done by the system during expansion. By 50 seconds, a noticeable temperature gradient can be observed. As shown in Figure 5.1, a thin boundary layer near the sidewalls becomes apparent, caused by the upward movement of heated air near the walls due to gravity. This heated air from the boundary layer accumulates and stagnates in the top region due to mass conservation and buoyancy.

  After 90 seconds, a relatively stratified vertical temperature distribution is observed in the central region, indicating thermal stratification. Moreover, a ring vortex emerges in the upper corners of the contour map due to the obstruction by the top surface, resulting in localized low-temperature regions on either side of the top area in contours, specifically in the annular region of the surge vessel near the top and the side surfaces. Additionally, small vortices and plumes are noticeable near the bottom surface, where heated air rises from the bottom, dissipating into the larger air mass above. The temperature difference between the top and bottom regions increases, reaching its peak around 124.2 s, just as the expansion process concludes.
  The lowest temperature during the process is around 245K.

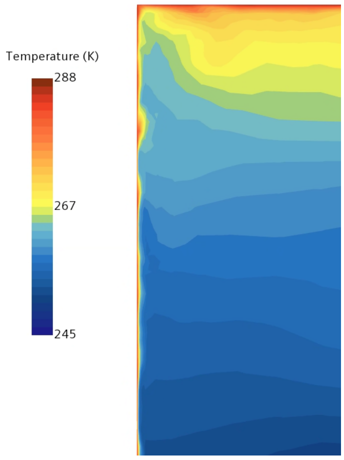

Figure 5.1: Zoom-in temperature field for the full-scale model at the top left corner at t = 100s

- After Expansion Reheating (t = 124.2s to t = 250s):

  After the expansion stops at 124.2 s, the stratified region at the top grows due to mass conservation, and there is an overall increase in the system's temperature. This reheating phase is clearly visible in the contour plots from 124.2 to 250 s. As the system gradually heats up, the high-temperature isotherms slowly move downward. Additionally, the small vortices near the bottom surface become more obvious.

  After 200 seconds, the merging of hot air from the bottom vortices with the stratified air above contributes to the heating of the internal air together. This merging phenomenon affects the vertical stratification seen in the lower regions of the contour plots, reducing the temperature uniformity along the same horizontal planes. By 250 seconds, the temperature has almost recovered to the initial temperature.

5.1.2. Velocity Field

Figure 5.3 shows the velocity field images at different times, illustrating the evolution of the velocity field. The velocity field images are represented using streamlines along with velocity vectors positioned on the streamlines. The air expansion process lasts for 124.2 s. Images are captured every 25 seconds during the expansion, and images are taken every 50 seconds after the expansion.

At the beginning, the overall velocity inside the container is relatively low. However, as the air expands, the boundary layers, as described in section 5.1.1, begin to form. As the expansion continues, the velocity within the boundary layer gradually increases, while the velocity in the central region remains lower due to mass conservation. The velocity in the core region is around 0.05m/s downwards. After the expansion stops, the velocity within the boundary layer gradually decreases, and the velocity field becomes more uniform. The highest velocity, 1.35 m/s, occurs within the boundary layer at t= 124.2s (expansion stops).

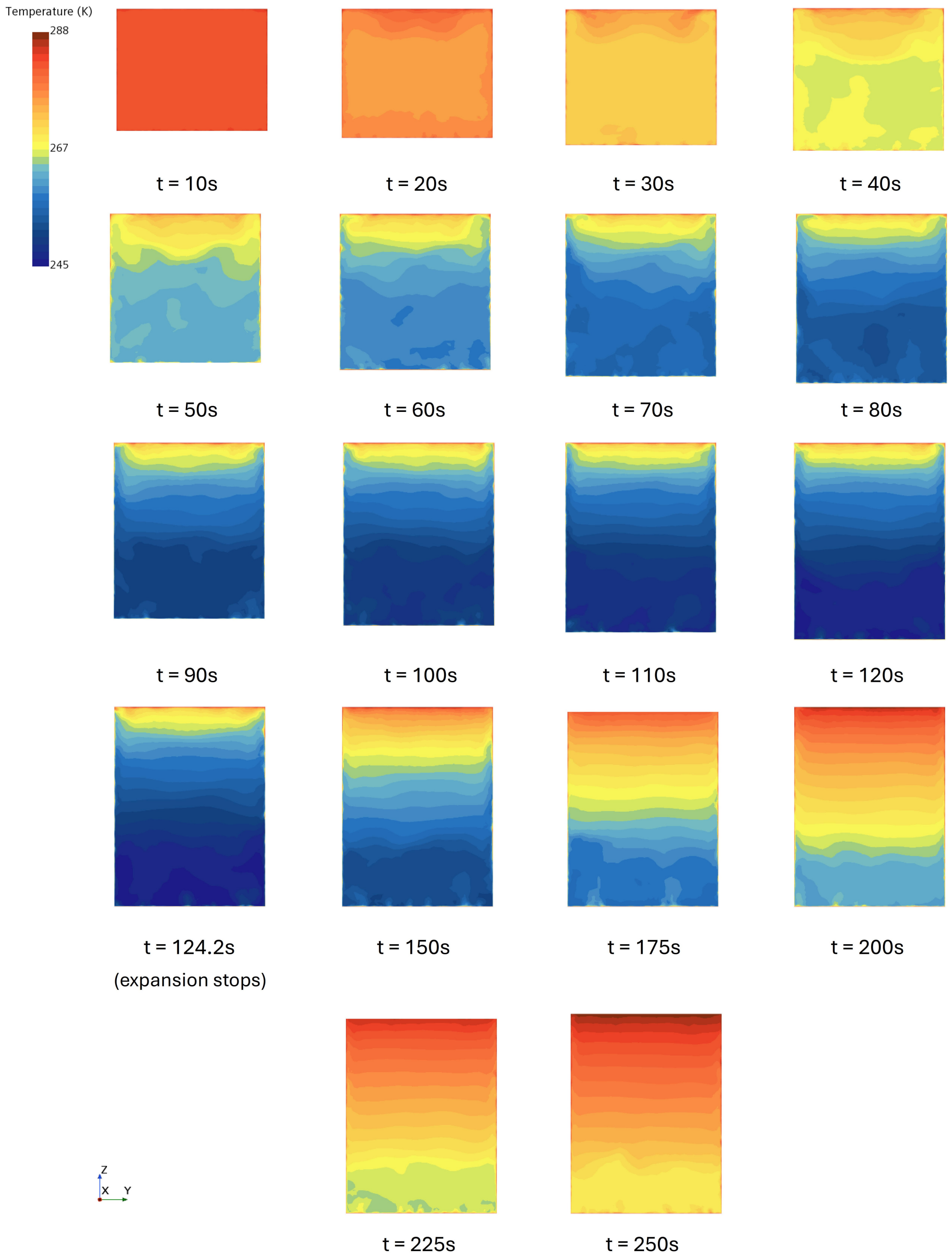

t = 10s t = 20s t = 30s t = 40s

t = 50s t = 60s t = 70s t = 80s

t = 90s t = 100s t = 110s t = 120s

t = 124.2s (expansion stops) t = 150s t = 175s t = 200s

t = 225s t = 250s

Figure 5.2: Temperature field for the full-scale model on the middle vertical plane at different times

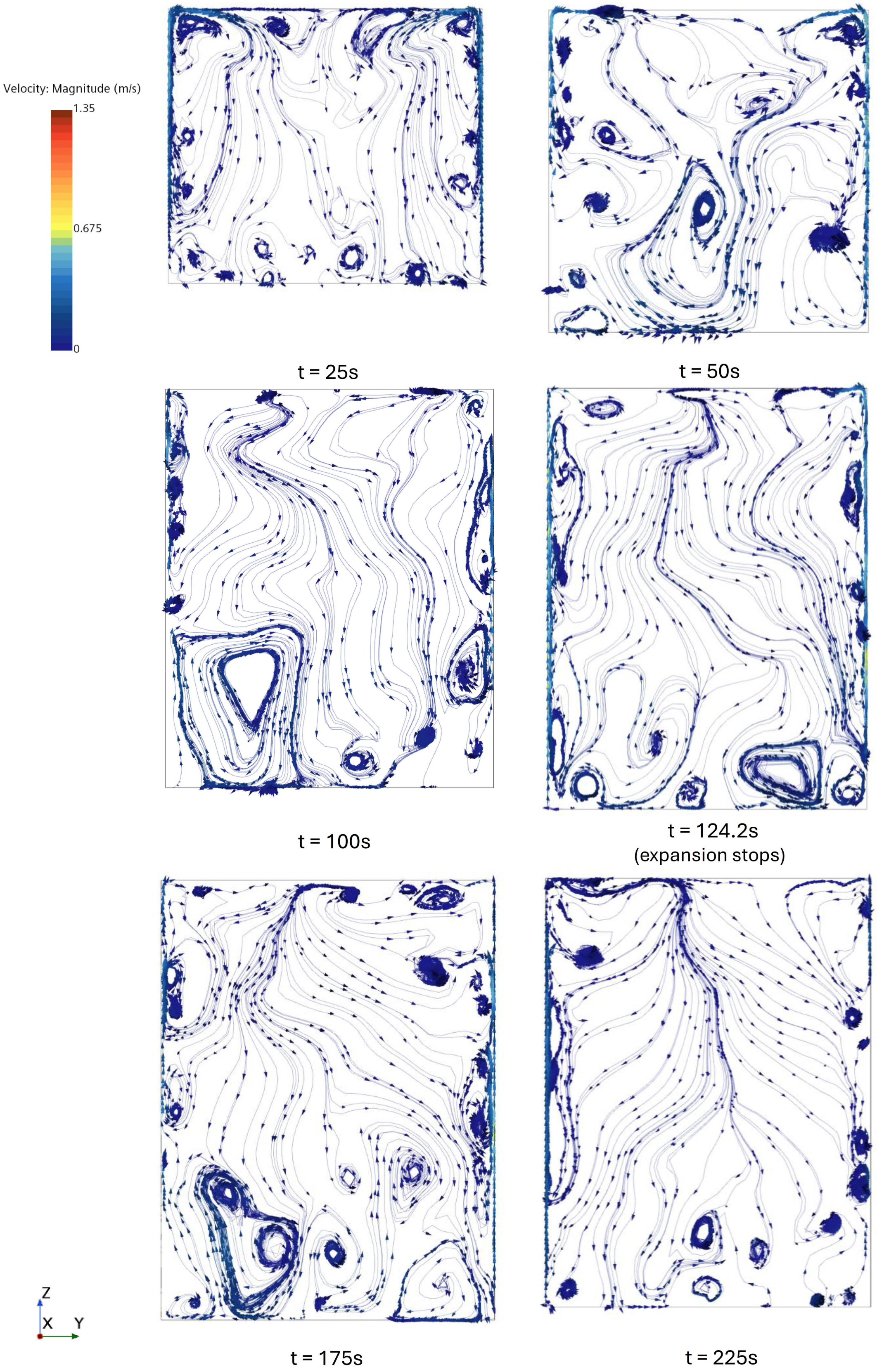

t = 25s

t = 50s

t = 100s

t = 124.2s
(expansion stops)

t = 175s

t = 225s

Figure 5.3: Velocity field for the full-scale model on the middle vertical plane at different times

5.1.3. Probe Monitor

Horizontal line probes

This section will analyze the temperature and velocity data from two horizontal probes. Figure 5.4 shows the distribution of the horizontal line probes. One probe is located at the initial geometry's bottom surface, while the other is positioned at three-quarters of the initial height. Therefore, one probe represents the temperature and velocity distribution in the central part of the container, while the other represents the distribution in the top region of the vessel.

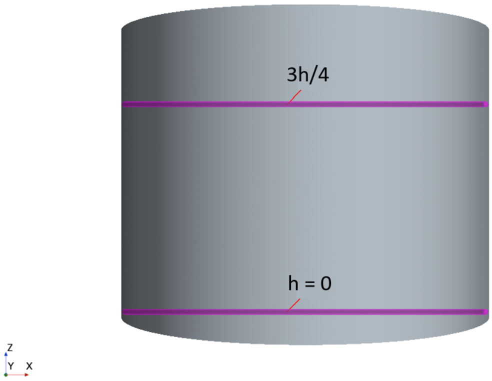

Figure 5.4: Geometry of two horizontal line probes for the full-scale model

Figures 5.5 and 5.6 show the temperature and z-direction velocity distributions from the line probes located at the bottom of the initial geometry. Corresponding to the observations mentioned in the previous section, it can be seen from the figures that the temperature near the wall rises sharply to the wall temperature of 288.44K, confirming the presence of a boundary layer near the wall. Additionally, the temperature distribution within the interior appears relatively uniform in the vertical direction. Also, the rate of temperature decrease slows down as the air expands, with the temperature showing almost no change between 100 and 125 seconds.

The velocity figure shows fluctuations in the central region during the initial phase of expansion. This is because the line probe is located in the bottom area at the beginning, where it is influenced by the small vortices and plumes near the bottom, leading to these fluctuations. After 100 seconds, the central region's velocity stabilizes. Additionally, it's evident that the velocity in the z-direction in the central region is negative and relatively low, while the velocity within the boundary layer is positive and high. This observation is related to the principle of mass conservation in the airflow within the vessel.

Figure 5.7 shows the temperature distribution captured by the line sensor positioned at $\frac{3h}{4}$ of the container's initial height. Compared to the line sensor at the bottom, it is evident that the temperature is more unstable during the expansion process. This instability is due to the influence of the ring vortex near the top of the container on the upper line probe. The figure also illustrates the circular ring effect mentioned in Section 5.1.1, where a low-temperature region exists near the boundary layer at the wall. Additionally, it can be observed that the temperature stabilizes around 75 seconds, which is earlier than the stabilization observed at the bottom sensor.

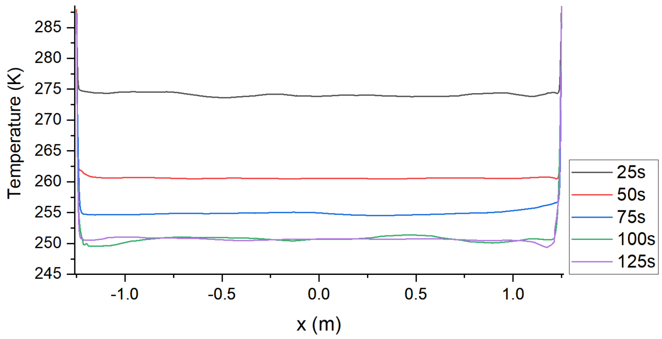

(a) from 25s to 125s

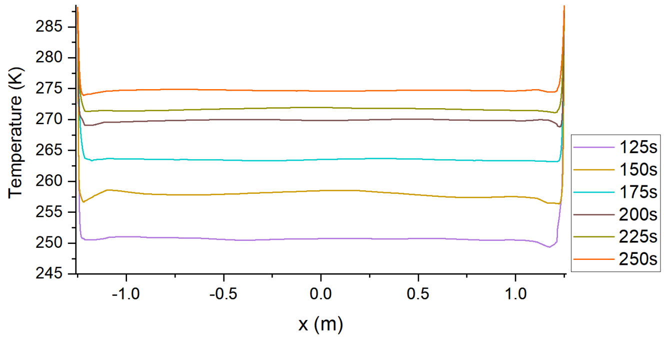

(b) from 125s to 250s

Figure 5.5: Temperature distribution of the horizontal line probe at h=0 for the full-scale model at different times

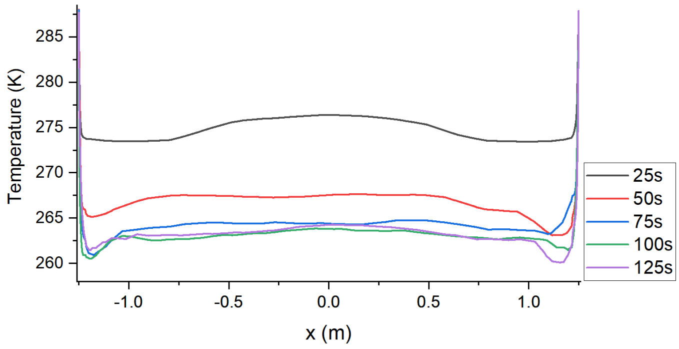

(a) from 25s to 125s

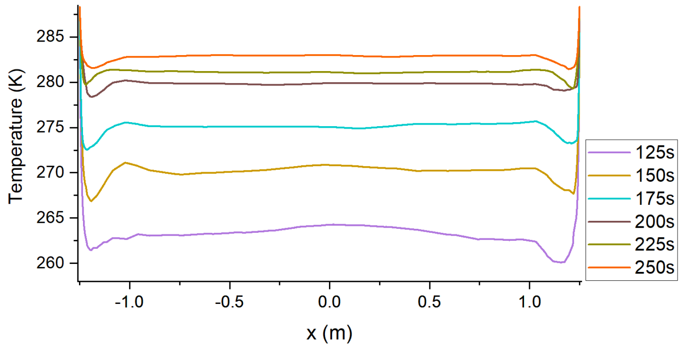

(b) from 125s to 250s

Figure 5.7: Temperature distribution of the horizontal line probe at h=$\frac{3h}{4}$ for the full-scale model at different times

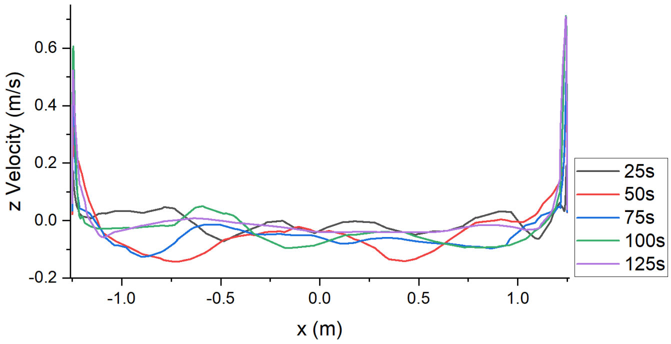

(a) from 25s to 125s

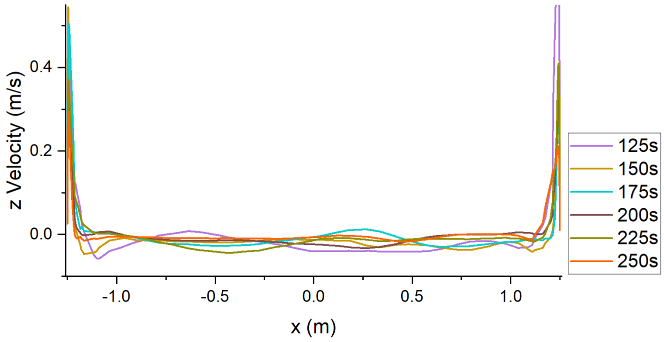

(b) from 125s to 250s

Figure 5.6: z-direction Velocity distribution of the horizontal line probe at h=0 for the full-scale model at different times

Vertical line probes

This section will analyze the temperature and velocity data from two horizontal probes. Figure 5.8 shows the distribution of the horizontal line probes. To smooth out the local fluctuations caused by vortices, the values for the vertical line probe are averaged across five line probes.

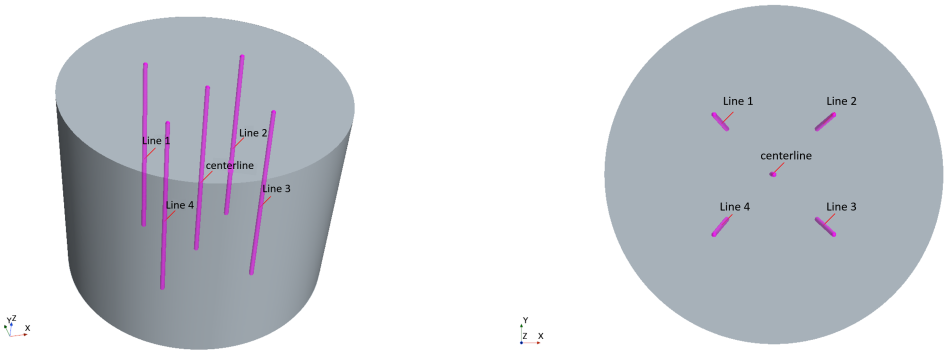

(a) (b)

Figure 5.8: Geometry of the vertical line probes for the full-scale model

A clear temperature stratification evolution with time is presented in Figure 5.9. Since the system is continuously expanding and the total height constantly changes, a scaled height, denoted as scaled h (height/current total height), is used to analyze the data. It can be observed that scaled h shows some fluctuations near 0, which confirms the presence of the small vortices at the bottom as discussed in the previous section. Additionally, the nearly vertical temperature distribution in the central region indicates good mixing in that area. After 125 seconds, a distinct temperature stratification phenomenon becomes evident, with the temperature tilt distribution in the central part appearing approximately linear.

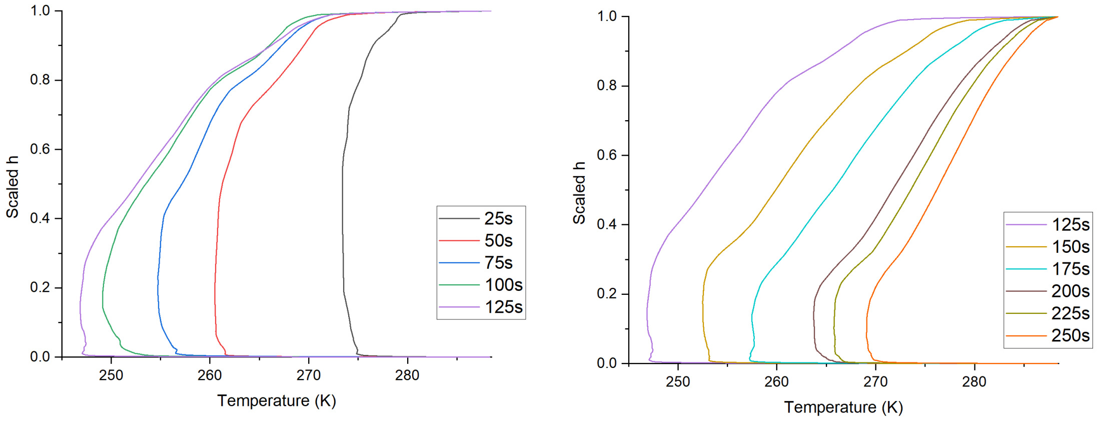

(a) from 20s to 120s

(b) from 120s to 250s

Figure 5.9: Temperature distribution of the vertical line probe for the full-scale model at different times

Point probes

Two representative points were selected from the 25 thermocouples for analysis, which are the k11 and k15 sensors. The k11 and k15 sensors are positioned at the highest and lowest points on the same support structure, respectively. Their temperature and velocity plots are shown in Figure 5.10, where velocity is represented by its magnitude.

From the graph, it is evident that the velocity and its fluctuations are relatively high from 30s to 80s, with 0.15 m/s for k11 and 0.12 m/s for k15. Then it decreases after 80s, with approximately 0.03 m/s for k11 and 0.02 m/s for k15. Moreover, in the k15 plot, a clear relationship between temperature and velocity can be observed: when the heated air in the container reaches the thermocouple, the velocity at the thermocouple increases. This corresponds to a halt or even a slight increase in the temperature.

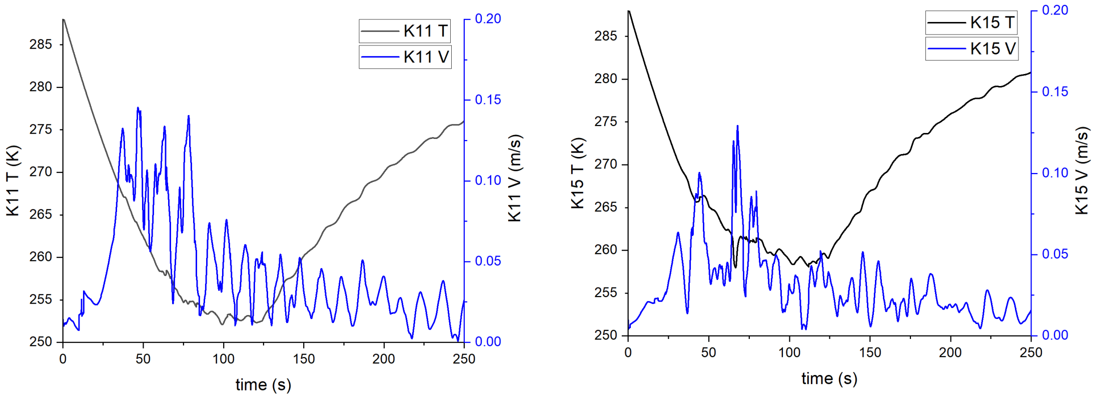

(a) k11

(b) k15

Figure 5.10: Temperature and velocity of the point probes for the full-scale model

5.1.4. Polytropic Number

Figure 5.11 illustrates the variation of the polytropic number n during the expansion process of the full-scale model by Equation 2.9. The polytropic number is observed to decrease gradually from approximately 1.4 to around 1.03, indicating that the behavior of the air inside the system transitions from being closer to adiabatic (n=1.4) towards more isothermal conditions (n=1.0) as the expansion progresses. This trend aligns with the observations in Figure 5.5 and 5.7, where the temperatures recorded by the horizontal line sensors remain relatively stable after 100 or 75 seconds.

Since the polytropic number n varies approximately linearly with time, a linear fit is applied to the data. The fitting result is: $n = -0.00304t + 1.40383$ with an R^2 value of 0.99617. The R^2 value represents the proportion of the variation in the dependent variable that can be predicted from the independent variable. A higher R^2 value indicates a better fit.

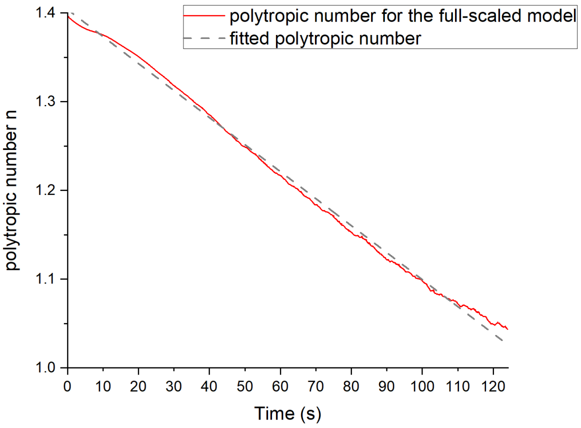

Figure 5.11: Polytropic number n during the expansion of the full-scale model and its linear fit

5.2. Scaled Small-Size Model

This section will describe the temperature and velocity fields in the scaled small-size model and compare these results with results from the full-scale simulation. For the scaled small-size simulation, the estimated maximum Rayleigh number (Ra) is 1.92 $\times 10^7$, which occurs at the time when the expansion stops (t = 124.2 s). This indicates that during the expansion process, the airflow inside the vessel remains laminar.

5.2.1. Temperature & Velocity Field

Figures 5.13 and 5.13 show the temperature and velocity distributions in the vertical central plane of the scaled small-size model. Compared to the full-scale model, the smaller geometry and Rayleigh number result in a more laminar flow regime in the air. Due to the varying temperature difference between the air and the walls, the height of the air region, and the air density, the Rayleigh number (Ra) also continuously changes throughout the expansion process. The average estimated Rayleigh number for the full-scale simulation is about 1.5×10^{10}, the scaled small-size simulation is about 1.5×10^7.

The temperature and velocity distributions in the small model are more symmetrical. Additionally, due to the smaller size of the model, the interaction between the vortices near the bottom surface and the

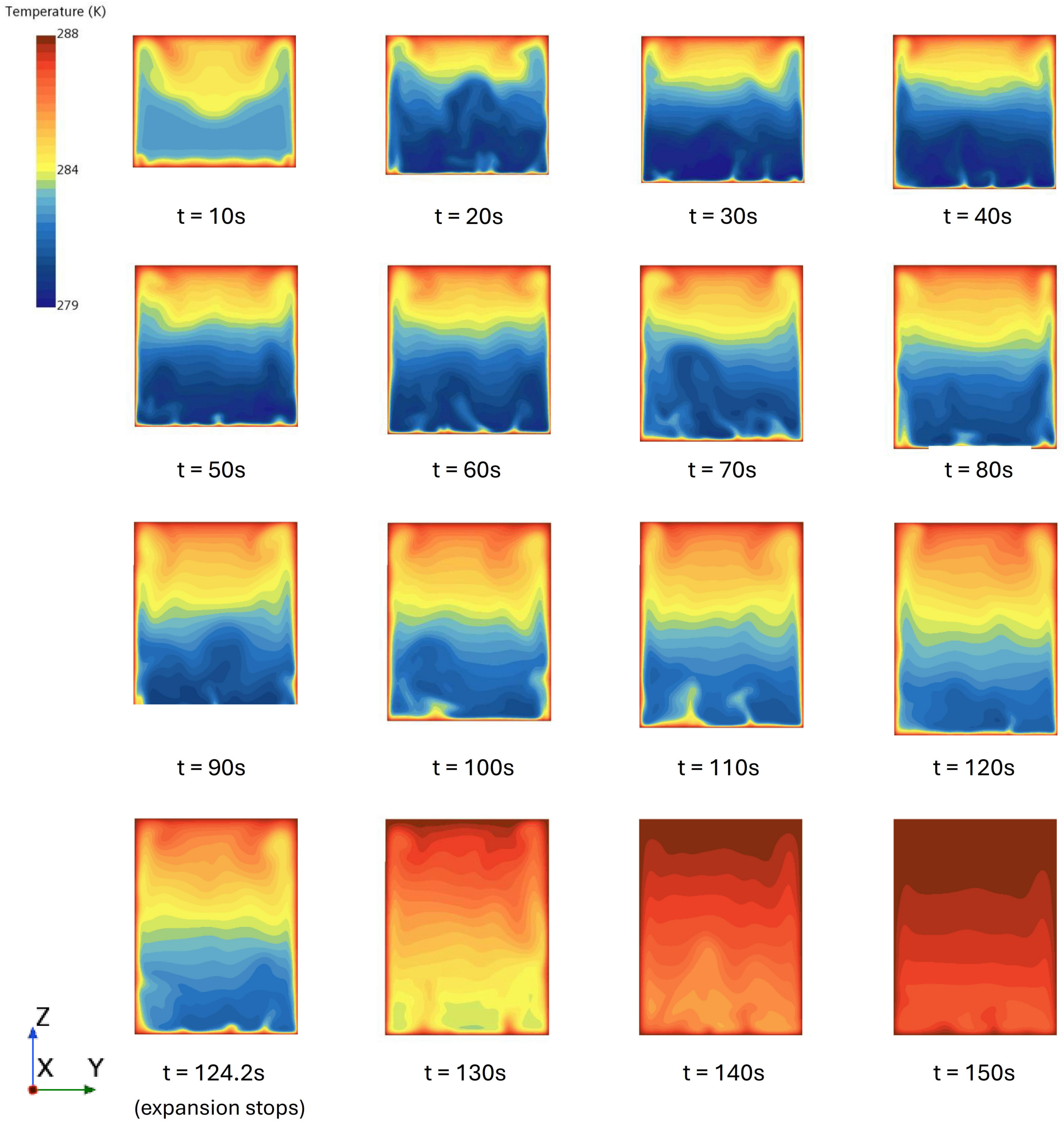

Figure 5.12: Temperature field for the scaled small-size model on the middle vertical plane at different times

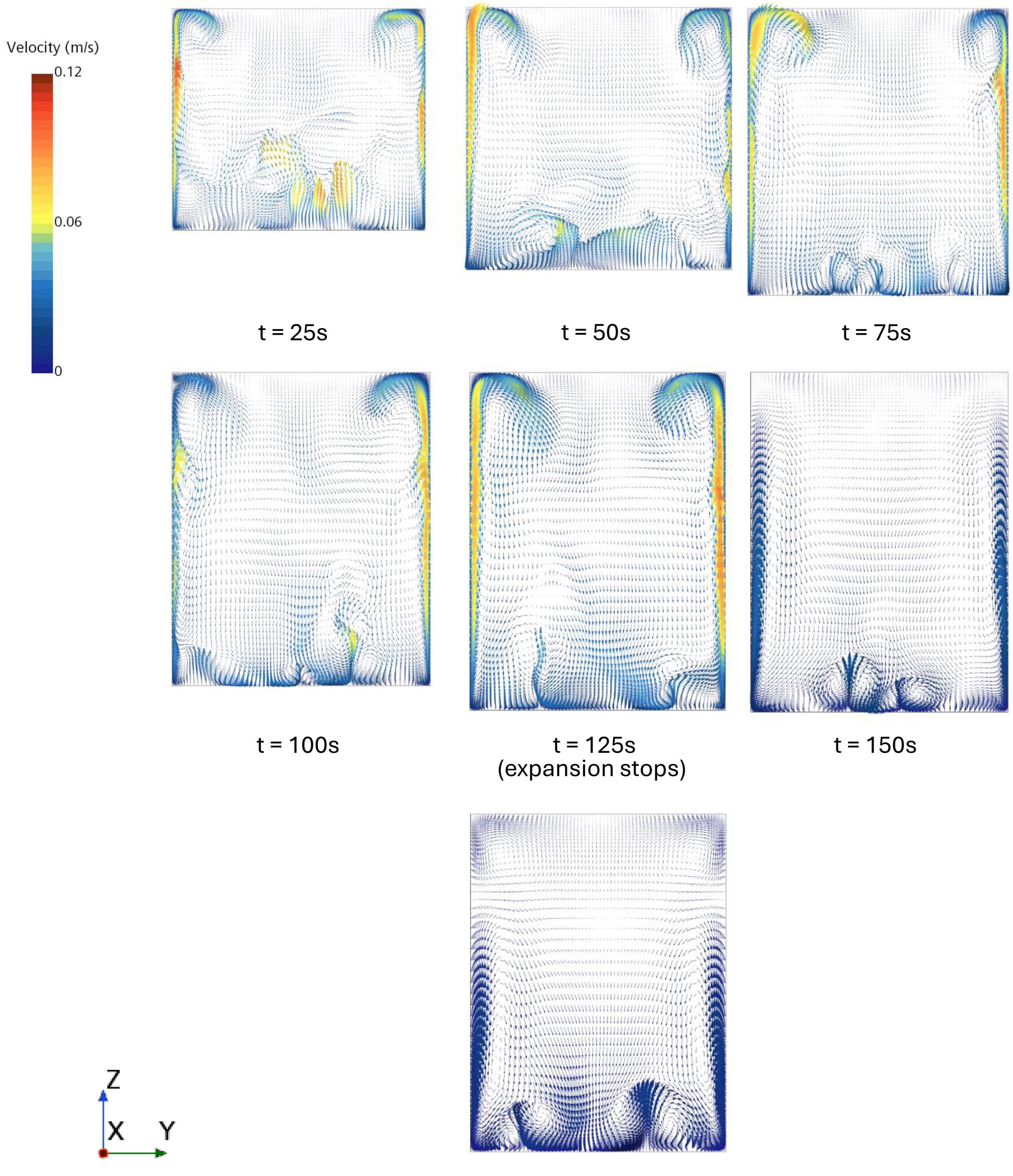

t = 25s

t = 50s

t = 75s

t = 100s

t = 125s
(expansion stops)

t = 150s

t = 175s

Figure 5.13: Temperature field for the scaled small-size model on the middle vertical plane at different times

internal air is more intense and obvious. The boundary layer on the side walls is also more clearly visible. Consequently, the temperature rises more quickly, with the internal air almost returning to the initial temperature by 150 seconds.

5.2.2. Probe Monitor

Five representative sensors, selected from five different heights (in the z direction) and four distinct vertical frame positions (in the x and y directions) among the 25 sensors, were compared. Figure 5.14 shows the temperature variations of these five sensors in both the scaled small-size model and the full-scale model. The comparison highlights that the model size has a significant impact on heat transfer. In both models, the temperature decreases similarly during the initial 10 seconds of expansion. However, after this point, the temperature trends begin to diverge. For the scaled small-size model, the temperature starts to rise before the expansion stops, indicating that the heat transfer within the container has surpassed the work done by the system at this stage. After the expansion, the temperature rises rapidly before gradually decreasing to near equilibrium. In contrast, for the full-scale model, the temperature continues to decrease throughout the expansion process until it stops.

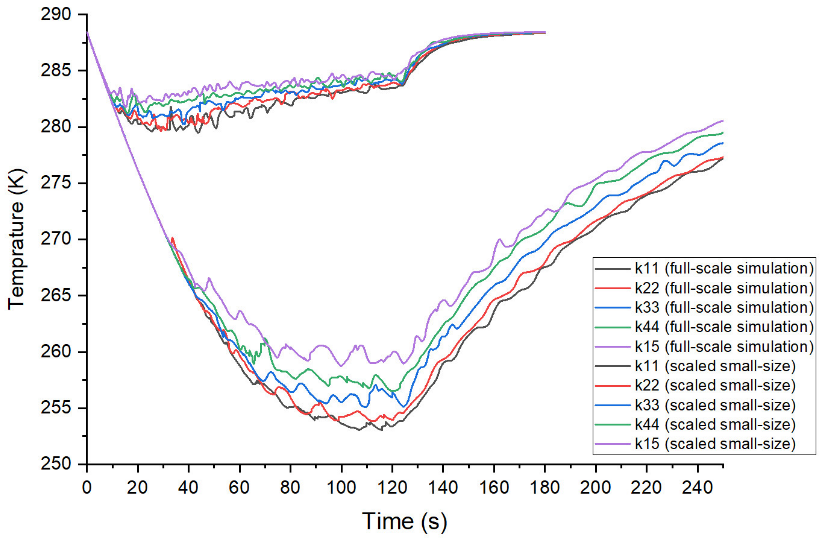

Figure 5.14: Temperature probe comparison between the scaled small-size and full-scale model

5.3. Experimental Measurements

This section focuses on comparing the simulation results of the full-scale model with experimental data to assess the accuracy and reliability of the simulations. The analysis aims to identify and explain the difference between the simulated and experimental results. This section is the extension of the discussion in Section 4.5.

5.3.1. Comparison between k-type and t-type Thermocouples in the Measurements

In the experiment, temperature measurements were collected using a total of 25 thermocouples, consisting of 20 k-type and 5 t-type thermocouples, as shown in Figure 3.3. The thermocouples were fixed on an aluminum frame. Each thermocouple is labeled using a three-alphabet/number system: the first number indicates the thermocouple type, the second represents the vertical frame number, and the third denotes the height position of the thermocouple. For instance, k15 refers to the k-type thermocouple located at the highest position on the first vertical frame. It is important to note that the measurements from k44 were found to be unreliable. Due to the large number of thermocouples, this section will select a few representative thermocouples for further discussion.

Figure 5.15 presents the data collected from both k-type and t-type thermocouples at positions 11 and 15. The t-type thermocouples exhibited slower response times and less sensitivity to temperature fluctuations, leading to a delayed and higher minimum temperature recording. Conversely, the simulated data has quicker response times and greater sensitivity to fluctuations. Therefore, k-type thermocouples will be used for comparison in subsequent discussions.

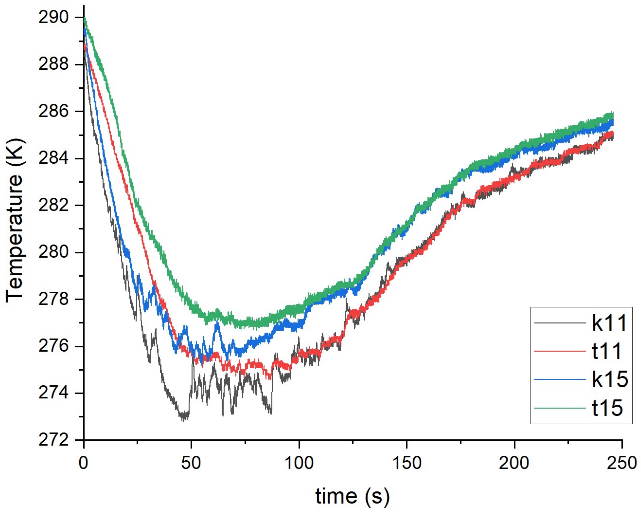

Figure 5.15: Comparison between the k-type and t-type thermocouples in the measurements for case 1

5.3.2. Comparison with Simulation Results

Probe Monitor

Figure 5.16 compares the temperature results from the full-scale simulation with the experimental measurements. The y-axis starts from the adiabatic expansion's minimum achievable temperature of 231.71K, as calculated in Section 4.1. The experimental data shows that the lowest temperature, around 273K, was recorded at approximately 40 seconds at the k11 position. After maintaining this temperature for about 45 seconds, the temperature began to rise gradually, reaching 277K by the time the expansion stopped at 124.2 seconds. In contrast, the simulation results indicate that the lowest temperature, around 253K, occurred near the end of the expansion, also at the k11 position. And a larger variation in temperature between different thermocouples appears, with a variation of approximately 15%.

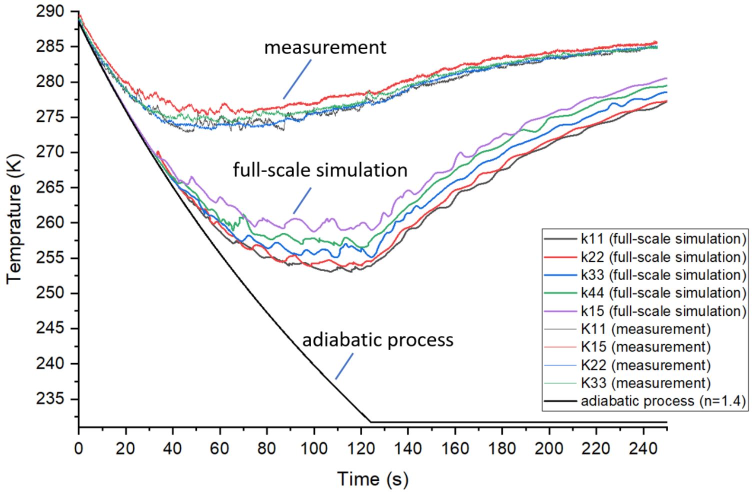

Figure 5.16: Comparison of temperature on probes between the measurements and full-scale simulation

Pressure

Figure 5.17 presents the comparison between the gauge pressure results from the full-scale simulation and the experimental measurements. The figure shows that the overall magnitude of pressure change is similar in both cases. In the experiment, the pressure drops rapidly at the beginning of the expansion, then gradually stabilizes. After the expansion ends, the pressure rises slowly. This observation corresponds with the temperature comparison, which exhibits a similar trend. In the experimental measurements, after 100 seconds, there is a big difference between the measured temperature and the simulated temperature. Consequently, due to the ideal gas law, the pressure is higher after 100 seconds, until around 180 seconds when the temperature difference decreases, causing the pressure to become a bit lower.

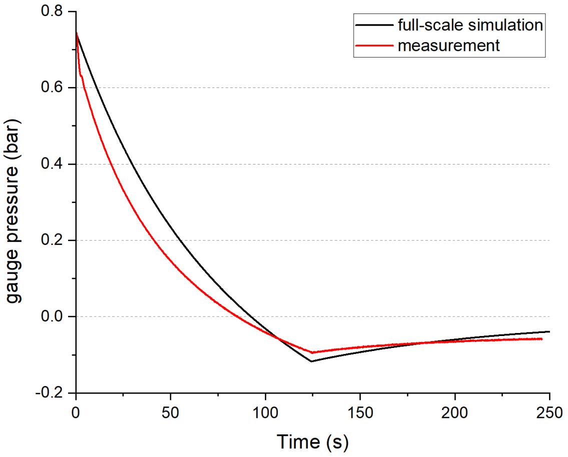

Figure 5.17: Comparison of pressure between the measurement and full-scale simulation

5.3.3. Discussion

Dome Volume

As discussed in section 4.3.2, considering the impact of the dome's volume would slightly reduce the air temperature inside the vessel. Since the current temperature within the vessel is already lower than the experimental measurements, the effect of the dome's volume is not taken into account.

Thermal Resistance in the Measurement

Figure 5.18 presents a thermal resistance schematic based on the experimental measurements. It extends the model shown in Figure 3.6 by incorporating the influence of the aluminum frame used during the experiment. The aluminum frame, which is used to fix the thermocouples (as depicted in Figure 5.19), transfers heat to the air inside the vessel via convection. The frame's total weight was measured to be 47.94 kg, with a specific heat capacity of 0.9 kJ/kg·K for the aluminum alloy. So the heat capacity of the frame is calculated to be 43.146 kJ/K. This indicates that for every 1 K decrease in the frame's temperature, it would transfer 43.146 kJ of heat to the surrounding air. Therefore, it is assumed that convective heat transfer from the aluminum frame to the air will affect the thermocouple readings during the measurements. To investigate the potential impact of the heated aluminum frame inside the vessel on thermocouple measurements, a simple simulation was conducted as detailed in the Appendix H.

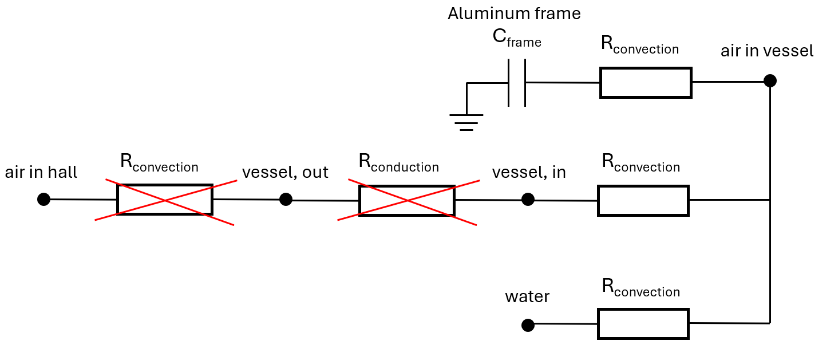

Figure 5.18: Thermal resistance schematic diagram in the measurements

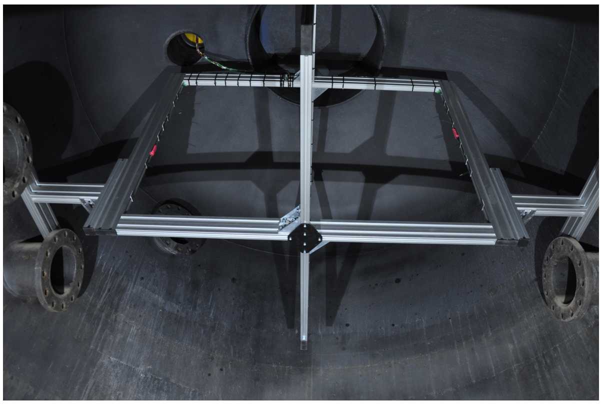

Figure 5.19: Aluminum frame photo in the measurements

5.4. Mathematical Calculation

This section is the calculated results of Section 3.2 and the extension of the discussion in Section 4.5.

5.4.1. Analytical estimation of heat transfer contributions

After the standard information about the expansion process is known, the different heat transfer processes discussed in Chapter 3.2 will be calculated quantitatively. Since the experimental measurements do not provide all the necessary information for the calculations, some of the calculations are based on a combination of experimental data and simulation results. Tables 5.2 and 5.3 summarize the key parameters of the vessel at the initial state and at the end of the expansion process (t = 124.2 s), respectively. These tables provide a comprehensive overview of the conditions within the vessel, reflecting both the initial setup and the state of the system after the expansion has stopped. Figures 5.20 and 5.21 present the measurement data from the pressure sensor and relative humidity sensor in the experiment, respectively. By analyzing these two sets of measurements, relevant data before the start and at the end of the expansion can be obtained for further calculations.

At the end of the expansion (124.2s), since the experimental data only includes thermocouple temperature readings and not the volume-averaged temperature, the volume-averaged temperature was calculated by combining experimental and simulation data as follows:

$$\begin{aligned}\text{Experimental Volume-Averaged Temperature} &= \text{Simulated Volume-Averaged Temperature} \\ &\quad + (\text{Average Experimental Thermocouple Temperature} \\ &\quad - \text{Average Simulated Thermocouple Temperature})\end{aligned} \tag{5.1}$$

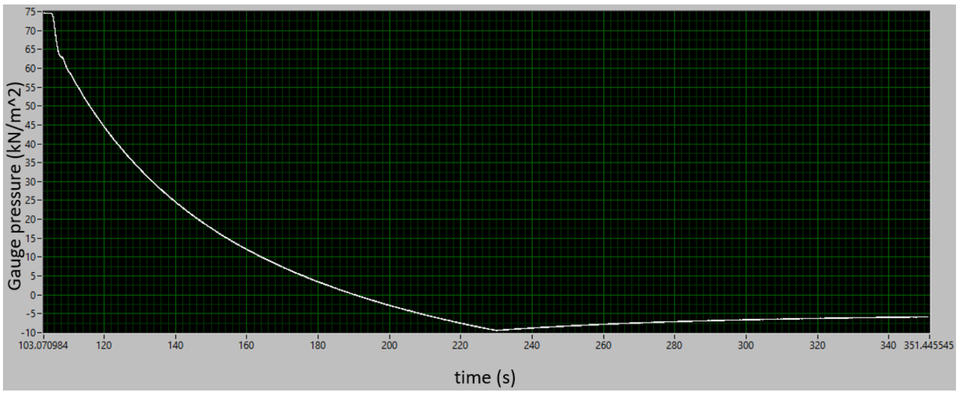

Figure 5.20: Measurement data from the pressure sensor in the experiment case 1

After substituting the experimental and simulation data into the respective equations discussed in Section 3.2, the resulting heat transfer magnitudes were calculated and are presented in Table 5.4. The data in the table indicates that heat transfer within the air inside the vessel primarily occurs through convective heat transfer with the vessel walls. The magnitude of convective heat transfer is 25 times greater than radiative heat transfer and 93 times greater than condensation heat transfer. However, the work done by

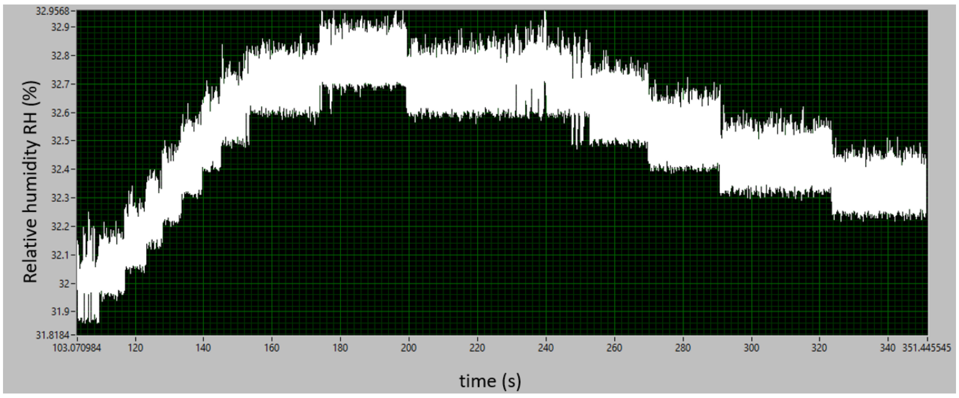

Figure 5.21: Measurement data from the relative humidity sensor in the experiment case 1

Table 5.2: Initial conditions of the experimental measurement case 1 for analytical estimation

Type		**Source**
volume average temperature T_{ini}	289.526 K	experiment
initial height h_{ini}	1.908 m	height with dome
initial volume V_{ini}	7.867 m^3	volume with dome
initial density ρ_{ini}	2.116 kg/m^3	ideal gas law
initial absolute pressure p_{ini}	175892.6 Pa	experiment
mass of air m	1.6649 kg	$\rho_{ini} \times V_{ini}$
initial relative humidity RH$_{ini}$	32%	experiment

Table 5.3: Final conditions of the experimental measurement case 1 for analytical estimation when t = 124.2s

Type		**Source**
volume average temperature T_{final}	275.8 K	experiment + simulation
final height h_{final}	3.299 m	height with dome
final volume V_{final}	14.6947 m^3	volume with dome
final density ρ_{final}	1.15982 kg/m^3	ideal gas law
final absolute pressure p_{final}	91825 pa	experiment
mass of air m	1.6649 kg	$\rho_{ini} \times V_{ini}$
final relative humidity RH$_{final}$	32.75%	experiment

the system is the most significant, approximately 5 times the sum of all forms of heat transfer combined.

Table 5.4: Analytical estimation of heat flow from the different processes and the work done by the system for experiment measurement case 1

Type	**Q /[kJ]**
condensation	1.7854
convection	165.275
radiation	6.684
work	913.948

5.4.2. RHT Model

Using the heat quantities obtained from Equation 2.13, the pressure change at each moment during the vessel's expansion can be calculated. By adding this change to the initial pressure, the pressure variation over time can be derived. Figure 5.22 shows the flowchart for calculating pressure variation using the RHT model. In the diagram, the formula for pressure variation dp is from Equation 2.13. The volume change $\frac{dV}{dt}$ becomes 0 after the expansion process ends (after t = 124.2s). The heat flow $\frac{dQ}{dt}$ is based on the sum of $\text{Q}_{condensation}$, $\text{Q}_{convection}$, and $\text{Q}_{radiation}$ from Table 5.4. The detailed MATLAB code can be found in the appendix J.

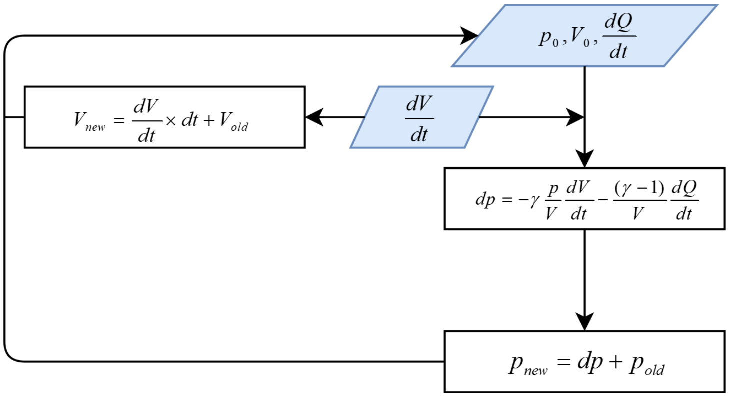
$p_0, V_0, \frac{dQ}{dt}$
$V_{new} = \frac{dV}{dt} \times dt + V_{old}$
$\frac{dV}{dt}$
$dp = -\gamma \frac{p}{V}\frac{dV}{dt} - \frac{(\gamma-1)}{V}\frac{dQ}{dt}$
$p_{new} = dp + p_{old}$

Figure 5.22: Flowchart for calculating pressure from the RHT model for case 1

Figure 5.23 presents and compares the gauge pressure results from the full-scale simulation, experimental measurements, and the RHT model calculations. From the figure, it can be observed that the RHT calculation results initially match the simulation results but diverge around 65 seconds. The RHT results continue to decline until the end of the expansion, remaining consistently below both the experimental and simulation pressures. This difference may be attributed to the fixed heat quantities used in the RHT calculation. As a result, this fixed heat value becomes increasingly inaccurate over time, leading to a growing error.

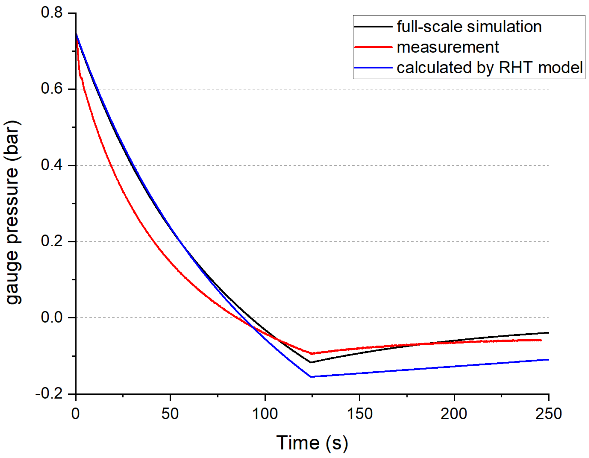

Figure 5.23: Comparison of full-scale Simulated, Experimental, and RHT-Calculated Pressure Values for case 1

5.4.3. Dynamic Heat Transfer Calculation using 0D Numerical Model

This section primarily uses MATLAB code to calculate the heat transfer values at each time step. The detailed MATLAB code can be found in the appendix J.

This code primarily integrates the ideal gas law (Equation 2.8) and energy balance equation (Equation 2.11), iterating over time to simulate the changes in system parameters and heat transfer during the expansion of the air pocket. The required initial conditions to be put in include the initial pressure, volume, and air temperature. Additionally, the wall temperature, the diameter of the vessel, and the volume change rate are also input values, which remain constant throughout the entire process. These input parameters are shown in the figure as blue parallelograms.

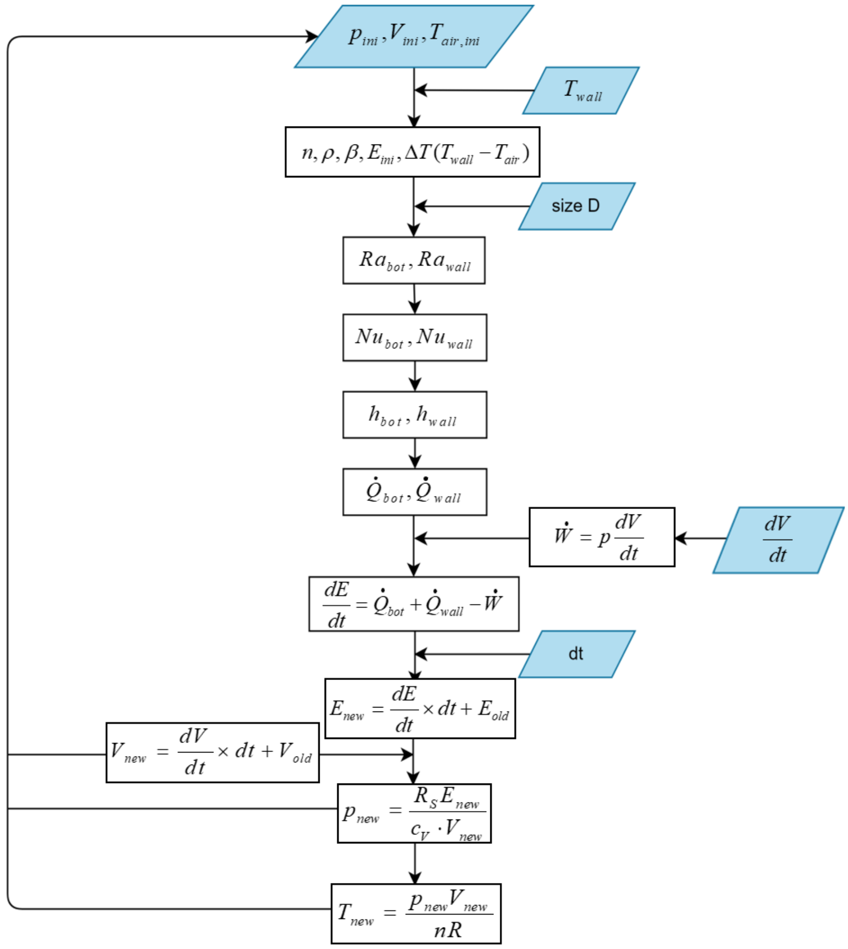
$p_{ini}, V_{ini}, T_{air,ini}$
T_{wall}
$n, \rho, \beta, E_{ini}, \Delta T(T_{wall} - T_{air})$
size D
Ra_{bot}, Ra_{wall}
Nu_{bot}, Nu_{wall}
h_{bot}, h_{wall}
$\dot{Q}_{bot}, \dot{Q}_{wall}$
$\dot{W} = p\frac{dV}{dt}$
$\frac{dV}{dt}$
$\frac{dE}{dt} = \dot{Q}_{bot} + \dot{Q}_{wall} - \dot{W}$
dt
$E_{new} = \frac{dE}{dt} \times dt + E_{old}$
$V_{new} = \frac{dV}{dt} \times dt + V_{old}$
$p_{new} = \frac{R_S E_{new}}{c_V \cdot V_{new}}$
$T_{new} = \frac{p_{new} V_{new}}{nR}$

Figure 5.24: Flowchart for calculating heat transfer over time for 0D numerical model

The formulas for the Ra number, Nu number, convective heat transfer coefficient h, and heat transfer $\dot{Q}$ are given by Equations 2.1, 2.3, 2.4, 2.6, and 3.2, respectively. The internal energy equation is given by Equation 5.2.

$$E = \rho c_v V T \tag{5.2}$$

The formula for p_{new} is given by Equation 3.15 and 5.2,which is:

$$p = \rho R_s T = R_s \cdot \frac{E}{V \cdot c_v} \tag{5.3}$$

The T_{new} equation is given by Equation 2.8.
Since the heat transfer from the top is small, it is neglected in the calculations. Figure 5.25 compares the heat transfer values obtained from the 0D numerical model with those from the full-scale model simulation for experiment case 1. Note that the heat transfer values are presented as negative in the plot to represent the heat leaving the vessel surfaces. This is equivalent to the positive values of heat absorbed by the air, with the magnitudes being the same but with opposite signs. It can be observed that the results are generally of the same magnitude and have similar trends. In the calculations, the heat transfer from the bottom is a bit higher than in the simulation, with the largest excess being around 100 W. For wall heat transfer and total heat transfer, the calculated values are slightly lower, with a difference of approximately 700 W. Reaching 250 seconds, the heat transfer values converge closely. Figure 5.26 compares the volume-averaged temperature results from the full-scale simulation and the 0D numerical model. The 0D numerical model predicts a lower volume-averaged temperature because its heat transfer is less than that of the simulation.

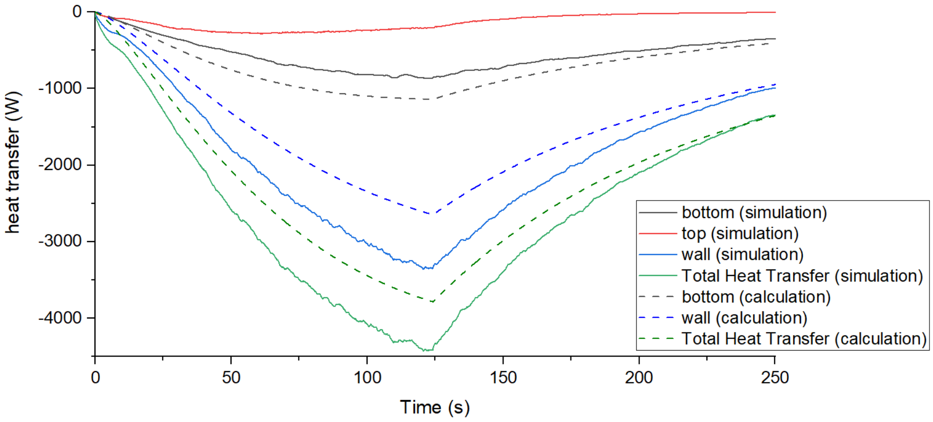

Figure 5.25: Comparison of Heat Transfer Leaving from Vessel Surfaces to the Inside Air between the Full-Scale Simulation and 0D Numerical Model Results for Case 1

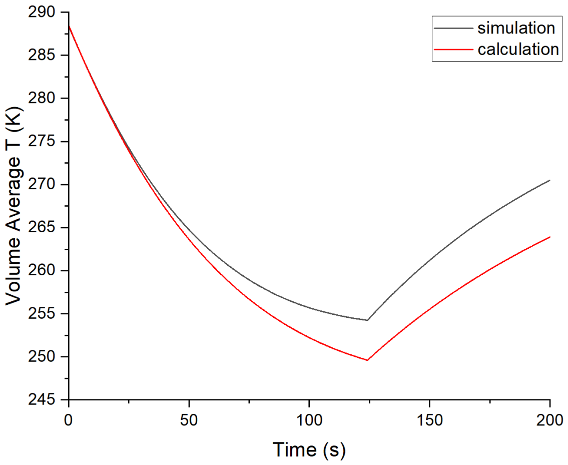

Figure 5.26: Volume average temperature comparison between full-scale simulation and 0D numerical model calculation results for case 1

5.5. Additional Experimental Case

This section is the extension of the discussion in Section 4.4.

To verify the accuracy of the results, a simulation analysis was conducted for another experimental case. For Case 2, the initial absolute pressure was 322 kPa, the initial temperature was 287.76 K, and the initial volume was 9.39 m^3. After 72.1 seconds, the system expanded to a volume of 16.44 m^3. For the simulation in case 2, the estimated maximum Rayleigh number (Ra) is 2.2×10^{11}, which occurs at the time when the expansion stops (t = 72.1 s).

Figure 5.27 shows the temperature on probes of the measurements and full-scale simulation in case 2. In Case 2, the expansion duration was only 72.1 seconds, leading to a greater decrease in temperature. The reasonable minimum temperature calculated using the ideal gas law is 230 K, which serves as the starting point for the temperature axis. The simulated temperature results are still approximately 20 K lower than the experimental results. This indicates that the temperature difference observed in Case 1 is not due to the specifics of the case itself. It is then possible that the aluminum framework within the vessel also plays a significant role in heat transfer.

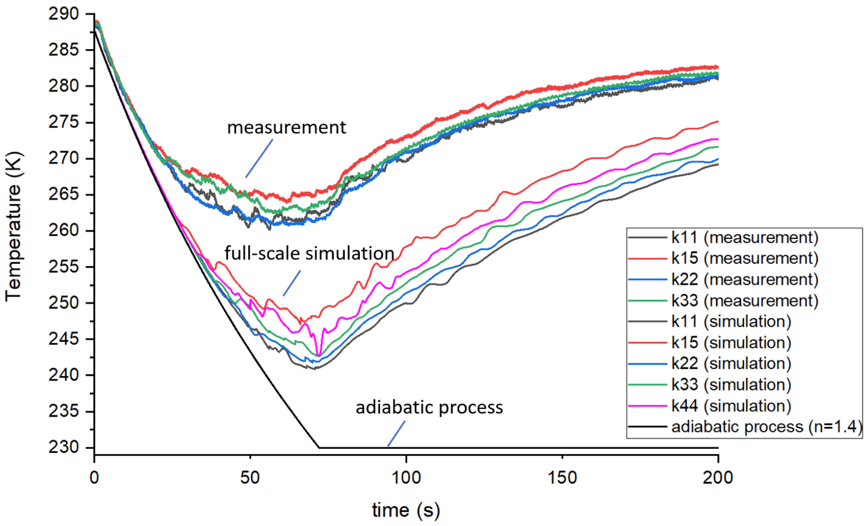

Figure 5.27: Comparison of temperature on probes between the measurements and simulation in case 2

Figure 5.28 illustrates the variation of the polytropic number n in Case 2. In this case, the polytropic number starts at approximately 1.4 and gradually decreases to around 1.17. It is worth noting that the polytropic numbers for case 2 and case 1 exhibit similar variations over time.

The dynamic heat transfer calculation code in section 5.4.3 is also applied to this experimental case. The comparison of heat transfer is shown in Figure 5.29. It can be observed that similar to Case 1, the calculation results are of the same order of magnitude as the simulation results. The calculated minimum heat transfer is slightly higher, while the wall heat transfer is a bit lower. The total heat transfer difference is approximately 1 kW. Similarly, due to the lower heat transfer, the volume-averaged temperature change in the 0D numerical model is also lower as shown in Figure 5.30. This observation is consistent with the results seen in case 1. This suggests that the 0D model agrees with the LES simulation for the two cases up to 12.2% in heat transfer.

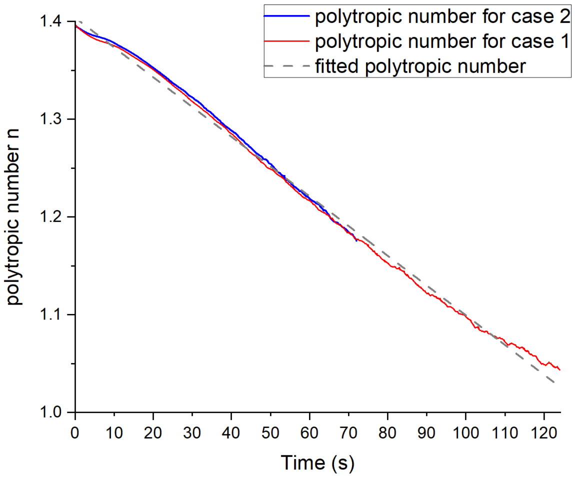

Figure 5.28: Polytropic number n comparison between case 1 and case 2

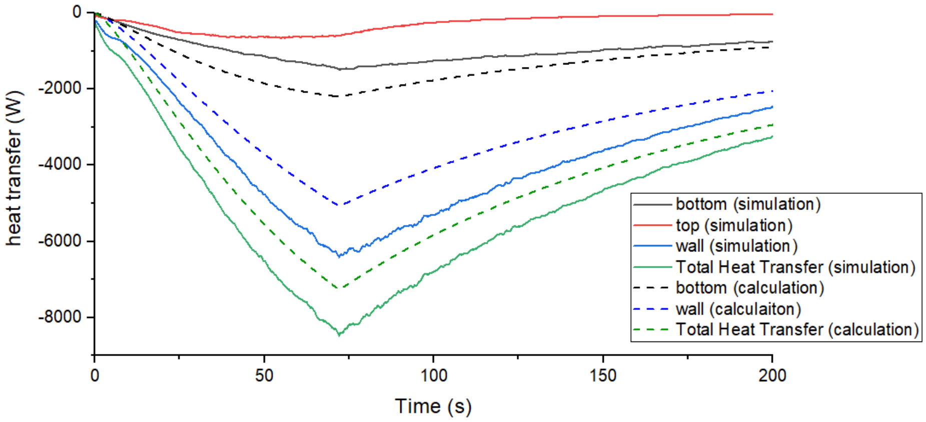

Figure 5.29: Comparison of Heat Transfer Leaving from Vessel Surfaces to the Inside Air between the Full-Scale Simulation and 0D Numerical Model Results for Case 2

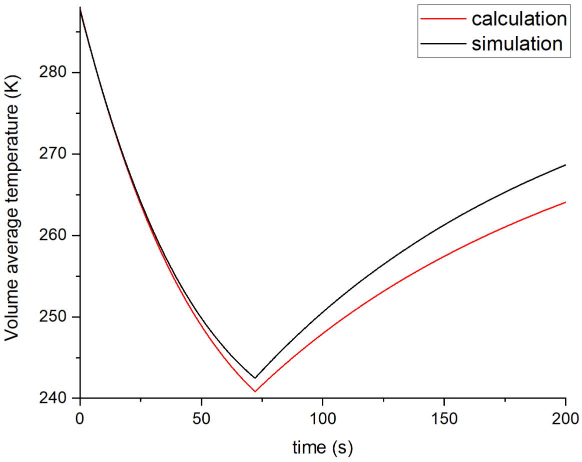

Figure 5.30: Volume average temperature comparison between full-scale simulation and 0D numerical model calculation results in case 2

6

Conclusions & Discussions

This section addresses the three tasks presented in section 1.2 by analyzing the findings from the results. Subsequently, a comprehensive examination of the limitations and future work is provided.

6.1. Conclusion

The objective of this project is to investigate the heat transfer behavior during the air expansion process in surge vessels. This thesis has provided a deeper insight into employing both lumped mathematical models and CFD simulations to explore the heat transfer mechanisms. The dynamic process of air expansion within the vessel is simulated and calculated, followed by a comparative analysis with experimental measurement data. The following conclusions can be drawn from the results presented in the previous chapter:

- The study compares the primary models used in the literature to analyze heat transfer in surge vessels: the polytropic model and the Rational Heat Transfer (RHT) model. The advantages and disadvantages of each model are outlined, highlighting their respective strengths and limitations in the heat transfer behavior during air expansion in surge vessels.
- For the first research objective, specific constant values of various heat transfer processes (convection, condensation, and radiation) were calculated. These values were analyzed and incorporated into the RHT model for further calculations. The pressure calculation results show a 7.14% error compared to the measured data and a 4.8% error compared to the simulation results, indicating good consistency in the analytical estimates.
- For the second research objective, the air pocket within the surge vessel was examined using the LES model to simulate the air expansion process. Simulations were conducted for both full-scale and scaled small-size models. The simulations successfully captured the temperature drop of the air inside the vessel during expansion and the heat transfer from the walls to the air. Additionally, a quantitative analysis of the various parameters involved in the expansion process was performed.

  - The heat transfer process during expansion is divided into three stages: the initial cooling stage, the rapid cooling and thermal stratification stage, and the reheat stage after expansion ends. During all these stages, the presence of boundary layers and the accumulation of hot air in the top region can be observed. The temperature field in the vertical direction exhibits an approximately linear distribution.
  - During the expansion process, the polytropic number of the internal air decreases from around 1.4 to around 1.05. This trend is consistent with the analysis in the literature, which describes the transition from a nearly adiabatic process to a nearly isothermal process.
  - For the scaled small-size model, the temperature drop is significantly less than that of the full-scale model, with a difference of about 25 K. Additionally, the temperature starts to rise even before the expansion stops. This indicates that the size has an impact on heat transfer within the surge vessel.

- For the third research objective, a 0D numerical model was developed to calculate the dynamic heat transfer during the expansion process. By employing the ideal gas law and the energy balance equation, the pressure, volume, and temperature are iterated over time to compute the heat transfer variations. When Compared with the simulation results, the overall heat transfer values are of the same order of magnitude, with an error of approximately 15.91% for experimental case 1 and 12.2% for experimental case 2.

Overall, this project conducted a comprehensive study of heat transfer in surge vessels through theoretical analysis, simulations, and lumped mathematical methods. The findings provide valuable references for validation and computational analysis in future related research, offering insights and guidance for understanding heat transfer phenomena in surge vessels.

6.2. Discussion

The study still has some limitations that can be improved in further research.

- **Ideal gas model**
  Both the simulations and mathematical calculations in this study used the ideal gas model. However, the actual properties of air in surge vessels are more complex. And the ideal gas model doesn't take the water vapor into account. To better simulate these complex air properties, future research could consider using a real gas model.

- **Boundary conditions**
  In the simulations, the wall boundary conditions were set as isothermal walls. However, in reality, the wall is influenced by both the low-temperature air inside the vessel and the convective heat transfer from the external environment. Consequently, the wall temperature in actual conditions should be lower than the ambient temperature. The study may have overestimated the heat transfer from the wall to the internal air. Future research could consider a coupled simulation taking into account heat transfer through the wall and convective heat transfer from the external environment to the wall.

Figure 6.1 illustrates the changes in the inner and outer wall temperatures during the air expansion experiments conducted by Haakh (Haakh, 2022). The data confirm that the wall temperature decreases due to the influence of the air inside and outside the vessel.

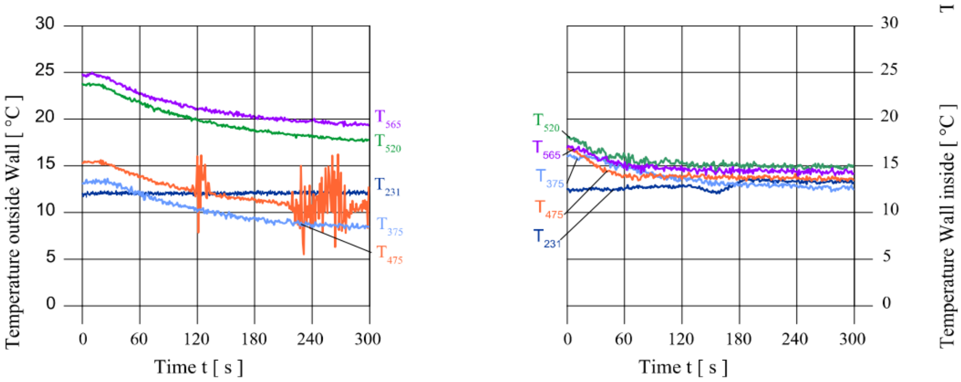

Figure 6.1: Temperature of the outside and inside wall during expansion in the experiment (Haakh, 2022)

- **”True” Temperature**
  When comparing the simulation results of the full-scale model with the experimental measurements, a temperature difference was observed. This difference may be attributed to the influence of the measurement support structure on the experimental results, or it could be attributed to simplifications in the simulation that excluded the effects of radiative heat transfer and phase change. The ”true” air temperature may lie between the simulation results and the experiment measurement results, or also be below the simulation results. Future research could investigate this.

- **Thermocouple types**
  In the experimental measurements, both k-type and t-type thermocouples were used to monitor temperature changes in the surge vessel. However, radiation heat within the container may affect the readings of these thermocouples (Mills, 1999). Haakh (Haakh, 2022) employed a fine wire thermocouple with a wire diameter of 0.08 mm and a time constant of $\tau_{air}90\% < 0.5\text{s}$, as shown in Figure 6.2. Future research could explore the selection of different types of thermocouples and include validations to ensure the accuracy of temperature readings.

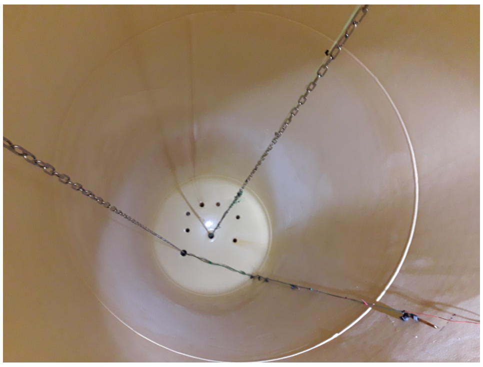

Figure 6.2: The wire thermocouple used in Haakh’s experiment measurements (Haakh, 2022)

For future related experiments about temperature measurements, it is recommended to consider the influence of radiation, wall temperatures (both inside and outside), using floating probes, and the methods to fix probes. These factors can influence the accuracy of measurements and offer valuable guidance for setting up numerical simulations.

- **Phase change**
  In the experiment for case 1, the temperature variation within the surge vessel was such that the minimum temperature was around 273 K at the sensor locations. However, for different initial conditions or surge vessel types, the minimum temperature might decrease further. During the experiments, phase changes within the surge vessel were challenging to record, so phase changes such as condensation or crystallization of the internal air were not clearly observed. In Haakh's experiments (Haakh, 2022), the minimum temperature recorded by thermocouples reached 240 K, suggesting that crystallization may occur in the air (Crank, 1979). Future research could focus on investigating phase changes occurring during the expansion process in the surge vessel.

- **Physical model**
  The current simulation model is a simplified model of the surge vessel, with the dome's impact on the volume being translated into the cylindrical height. However, in reality, the geometry of the dome may influence the internal airflow. Therefore, future research could involve a more precise model that accurately incorporates the dome's geometry to better understand its effect on heat transfer.

- **Compression process**
  This project focuses on the expansion process of air within the surge vessel. However, in practical applications, the compression and expansion of air in the vessel are continuous and dynamic processes. The compression phase influences the initial conditions and the temperature and velocity field distributions during the expansion phase. Therefore, future studies could consider the effects of the compression process to provide a more comprehensive understanding of the overall behavior.

- **RANS model**
  Section 4.3.1 discusses the validation of LES and RANS turbulence models. The LES model uses a local filtering approach, while the RANS model focuses more on averaged results. Although the RANS model shows an 11%-21% underestimation in heat transfer at the bottom, its overall performance is not significantly poor. Therefore, future research could involve a more detailed analysis of the feasibility of the RANS model, such as conducting RANS simulations on a full-scale model to compare the results with those of the LES model.

- **1D numerical model**
  This study only focused on the 0D numerical model. However, a 1D numerical model, like the Evans (Evans et al., 1968) model, is very important. The Evans model describes the axial temperature distribution over time. As described in Section 2.4.2, there is a stratified high-temperature region at the top of the model, which indicates that the heat transfer along the sidewall differs from the results calculated using the Nusselt number relationship for the vertical surface. In this study,

the impact of this high-temperature region is considered negligible, so a 0D numerical model is used to describe the heat transfer. Future research could explore the 1D numerical model.

Bibliography

Akpan, P., Mgbemene, C., Ume, J., Jones, S., Yeung, H., 2019. Constant heat outflow rates for air/surge vessel modelling during pressure transients. International Journal of Pressure Vessels and Piping 172, 295–303.

Akpan, P., Yeung, H., Jones, S., Njoku, H., Mgbemene, C., 2014. Mathematical models of air vessels for pressure transient control in water pipelines-a review. International Journal of Current Research 6, 5267–5272.

ANSYS, 2022. Ansys ICEM CFD Help Manual. 2023 r2 ed. Ansys.

Chen, X., Zhang, J., Yu, X., 2024a. Thermodynamic behaviour and heat transfer characteristics of air vessels in water delivery systems. Applied Thermal Engineering 236, 121428.

Chen, X., Zhang, J., Zhu, D.Z., Yu, X., 2024b. Surge analysis of air vessel with different connection types in pressurized water delivery systems. Journal of Hydraulic Engineering 150, 04023055.

Crank, J., 1979. The Mathematics of Diffusion. Oxford science publications, Clarendon Press. URL: https://books.google.nl/books?id=eHANhZwVouYC.

Drake, E.M., 1966. Transient natural convection of fluids within vertical cylinders. Ph.D. thesis. Massachusetts Institute of Technology.

Evans, L., Reid, R., Drake, E., 1968. Transient natural convection in a vertical cylinder. AIChE Journal 14, 251–259.

Graze, H., 1968. A rational thermodynamic equation for air chamber design, in: 3rd Australasian Conf. on Hydraulics and Fluid Mechanics, pp. 57–61.

Haakh, F., 2022. What happens in air vessels for water hammer protection? gwf Wasser / Abwasser 162, 489–503. doi:10.17560/gwfwa.v162i10.2549.

H.R.Graze, 1967. A rational approach to the thermodynamic behaviour of air chambers. Ph.D. thesis. University of Melbourne.

Incropera, F.P., De Witt, D.P., 1985. Fundamentals of heat and mass transfer .

Jones, C., Moore, D., Weiss, N., 1976. Axisymmetric convection in a cylinder. Journal of Fluid Mechanics 73, 353–388.

Leruth, P., Pothof, I., Naja, F., 2012. Validation of the surge model and lessons learnt from commissioning of the shuweihat water transmission scheme, uae, in: 11th International Conference on Pressure Surges, Lisbon, Portugal, 24-26 Oct., 2012, BHR Group Ltd.

Mills, A.F., 1999. Basic heat and mass transfer. (No Title) .

Mozayeni, H., Wang, X., Negnevitsky, M., Kefayati, G., 2020. Study of effect of heat transfer in an air storage vessel on performance of a pumped hydro compressed air energy storage system. International Journal of Heat and Mass Transfer 148, 119119.

Neumann, G., 1990. Three-dimensional numerical simulation of buoyancy-driven convection in vertical cylinders heated from below. Journal of Fluid Mechanics 214, 559–578.

Ortiz, A.V., Koloszar, L., 2023. Rans thermal modeling of a natural convection boundary layer at low prandtl number. Computers & Fluids 254, 105809.

Oyj, V., 2013. Humidity conversion formulas—calculation formulas for humidity. Humidity Conversion Formulas 16.

Siemens, 2021. Simcenter STAR-CCM+ User Guide. 2021.2 ed. Siemens. URL: www.siemens.com/mdx.

Slater, J.W., 2021. Examining spatial (grid) convergence. URL: https://www.grc.nasa.gov/www/wind/valid/tutorial/spatconv.html. accessed: 2023-09-09.

South, D., 2023. Spherical dome calculator. https://monolithicdome.com/spherical-dome-calculator?d=2.5&h=0.677&w=0&l=0&o=none&u=m&commit=Go.

Thorley, A.D., 2004. Fluid transients in pipeline systems: a guide to the control and suppression of fluid transients in liquids in closed conduits. John Wiley & Sons.

ToolBox, T.E., 2003. Air - thermophysical properties. URL: https://www.engineeringtoolbox.com/air-properties-d_156.html.

Toussaint, M., 2014. The effect of rational heat transfer on the behavior of surge vessels .

Vereide, K., Tekle, T., Nielsen, T.K., 2015. Thermodynamic behavior and heat transfer in closed surge tanks for hydropower plants. Journal of Hydraulic Engineering 141, 06015002.

Wikipedia contributors, 2024. Tetens equation — Wikipedia, The Free Encyclopedia. URL: https://en.wikipedia.org/wiki/Tetens_equation. [Online; accessed 22-August-2024].

Wylie, E.B., Streeter, V.L., Suo, L., 1993. Fluid transients in systems. volume 1. Prentice Hall Englewood Cliffs, NJ.

Yamaguchi, Y., Chang, C., Brown, R., 1984. Multiple buoyancy-driven flows in a vertical cylinder heated from below. Philosophical Transactions of the Royal Society of London. Series A, Mathematical and Physical Sciences 312, 519–552.

Zhang, J., Yu, X., et al., . Study on thermodynamic behavior and heat transfer characteristics of air vessel in water delivery system .

Zhang, S., 2022a. Large Eddy Simulation of Surge Vessel Thermodynamics. Technical Report. TUDelft, Deltares. Delft, the Netherlands.

Zhang, S., 2022b. Large Eddy Simulation of Surge Vessel Thermodynamics. Technical Report. Deltares.

Zhou, L., Lu, Y., Karney, B., Wu, G., Elong, A., Huang, K., 2023. Energy dissipation in a rapid filling vertical pipe with trapped air. Journal of Hydraulic Research 61, 120–132.

van der Zwan, S., Toussaint, M., Alidai, A., Pothof, I., Leruth, P., 2015. Thermodynamics of surge vessels, in: 12th International Conference on Pressure Surges, Dublin, Ireland.

Zwan, S.v.d., 2020. Minimizing the required surge vessel volume by an improved thermodynamic model. IAHR INSTITUTE MEMBERS PROJECTS 3, 90–91.

A

Simulation Setup and Parameters

This section outlines the specific parameters used in the expanding simulations. For non-expanding simulations, the mesh morphing model is disabled based on this setup.

A.1. Geometry

Table A.1: Geometry of the full-scale and scaled-small size model

Geometry	full-scale	scaled small-size
Diameter	2.5 m	0.25 m
initial height	1.908 m	0.1908 m
final height	3.299 m	0.3299 m

A.2. Initial & Boundary Conditions

Table A.2: Initial conditions

Initial condition	
Temperature	288.44 K
Pressure	175892.6 pa

A.3. Models & Solvers

Table A.3: Boundary conditions

Boundary condition		
Top	Isothermal wall	288.44 K
	Shear stress specification	no-slip
	Morpher	fixed
Bottom	Isothermal wall	288.44 K
	Shear stress specification	no-slip
	Morpher	displacement: grid velocity ($(Time)<124.20)? -0.0112:0
Wall	Isothermal wall	288.44 K
	Shear stress specification	no-slip
	Morpher	floating

Table A.4: Models & solvers used in the simulation

Models & Solvers	**Details**
LES turbulence model	
WALE subgrid scale model	
Segregated solver	
compressible ideal gas	air
Gravity	
implicit unsteady	
Adaptive time-step	mean CFL number 0.85 max CFL number 0.95
Solution interpolation	
Mesh morpher	

Table A.5: Stopping criteria

Stopping Criteria	**full-scale**	**scaled small-size**
Maximum inner iterations	20	10
Expanding time	124.2 s	124.2 s
Maximum physical time	250 s	180 s

B

Validation by Rayleigh-Bénard Convection

B.1. Model

To verify the capability of the StarCCM+ software for heat transfer analysis, a Rayleigh-Bénard Convection case is simulated and analyzed namely a case by Neumann (Neumann, 1990).

Experimental and numerical analysis of buoyancy-driven flow in a cylinder heated from below (Rayleigh-Bénard Convection) is included in the study by Neumann. The analysis covers fundamental aspects including the onset of convective instability, transitions to periodic and non-periodic motions, and examining the influence stemming from boundary and initial conditions. The main purpose of this case is to investigate natural convection in a vertical cylinder with a large aspect ratio (a = height/ diameter). In this section, the validation case only focuses on one set of numerical simulations with symmetrical temperature and velocity distribution.

The Boussinesq approximation is applied by adding buoyancy influences to the Navier-Stokes equations as Equation B.1. By the Boussinesq approximation, density variations resulting from inertial effects are ignored, and density becomes only a function of temperature as Equation B.2.

$$\rho_0\left(\frac{\partial u}{\partial t}+u\nabla u\right)=-\nabla p+\mu\nabla^2 u+(\rho_0+\Delta\rho)g \tag{B.1}$$

$$\rho=\rho_0(1-\beta\Delta T) \tag{B.2}$$

Where ρ_0 is the reference density at the reference temperature 300 K; β is the volumetric expansion coefficient, usually approximated as the reciprocal of the reference temperature: $\beta = 1/T_0$.

The continuity, momentum, and energy equations:

$$\frac{\partial u_i}{\partial x_i}=0$$

$$\frac{\partial u_i}{\partial t}+u_j\frac{\partial u_i}{\partial x_j}=-\beta\frac{T-T_0}{T_0}g_i-\frac{1}{\rho_0}\frac{\partial p}{\partial x_i}+\nu\frac{\partial^2 u_i}{\partial x_j^2} \tag{B.3}$$

$$\frac{\partial T}{\partial t}+u_j\frac{\partial T}{x_j}=\alpha\frac{\partial^2 T}{\partial x_j^2}$$

Where α is the constant thermal diffusivity, $\alpha = k/\rho_0 c_p$; g is the gravity acceleration.

The Rayleigh number Ra is a dimensionless number associated with buoyancy-driven flow, defined as the product of the Grashof number and Prandtl number:

$$Ra = GrPr = \frac{\beta \Delta T g h^3}{\nu^2}Pr \tag{B.4}$$

A series of Rayleigh numbers from 650 to 950 is simulated and analyzed. In Neumann's case, the Prandtl number is assumed to be 1, but the real air at normal temperature cannot reach this value. The Prandtl number of air at 293 K and 1 bar is supposed to be 0.705. The Prandtl number is the ratio of momentum diffusivity to thermal diffusivity as given in Equation B.5.

$$Pr = \frac{c_p \mu}{k} \tag{B.5}$$

Therefore, the air properties are adjusted to different temperatures, resulting in slight deviations from their values under normal temperatures. However, these adjustments together maintain the Prandtl number close to 1. The specific heat capacity c_p and the viscosity μ are interpolated at temperature T = 360K, and the thermal conductivity k is interpolated at temperature T = 240K under atmospheric pressure. The Prandtl number of 0.988 is reached by these numbers, with air property data from the engineering toolbox database (ToolBox, 2003). To ensure reasonable temperature differences for a range of Rayleigh numbers in Neumann's cases, the dimensions are set to a height of h = 0.01m and a diameter of d = 0.0345m, resulting in an aspect ratio of a = 0.2899.

The Nusselt number is the ratio of convective to conductive heat transfer at a fluid boundary:

$$Nu = \frac{hL}{k} \tag{B.6}$$

The average Nusselt number is typically used to describe the overall heat transfer:

$$\overline{Nu} = \frac{4a^2}{\pi}\int_0^{2\pi}\int_0^{\frac{1}{2a}} r(-\frac{\partial T}{\partial z}|_{z=0,h})drd\theta \tag{B.7}$$

Table B.1 lists the air properties and physical parameters.

At all the walls the shear-free velocity boundary condition is prescribed. The cylinder is evenly heated from below at a constant higher temperature $T_{bottom} = T_0 + \frac{\Delta T}{2}$ and cooled from the top at a lower temperature $T_{top} = T_0 - \frac{\Delta T}{2}$. The temperature difference is calculated from the Rayleigh number. The sidewalls are all adiabatic. As Figure B.1, the mesh of the cylinder has 36 cells in the radial direction and 32 cells in the vertical direction, such that the total element number approaches the mesh used in Neumann (Zhang, 2022b).

Table B.1: Air properties and physical parameters in the validation case

Specific heat capacity at constant pressure	c_p	1010.03	J/kgK
Dynamic viscosity	μ	2.13154×10^{-5}	Pas
Kinematic viscosity	ν	1.81100×10^{-5}	m^2/s
Thermal conductivity	k	0.0217728	W/mK
Density	ρ_0	1.177	kg/m^3
Thermal diffusivity	α	1.8315×10^{-5}	m^2/s
Volumetric expansion coefficient	β	0.00333	K^{-1}
Gravity	g	[0, 0, -9.81]	m^2/s
Height	h	0.01	m
Diameter	d	0.0345	m
Aspect ratio	a	0.2899	-

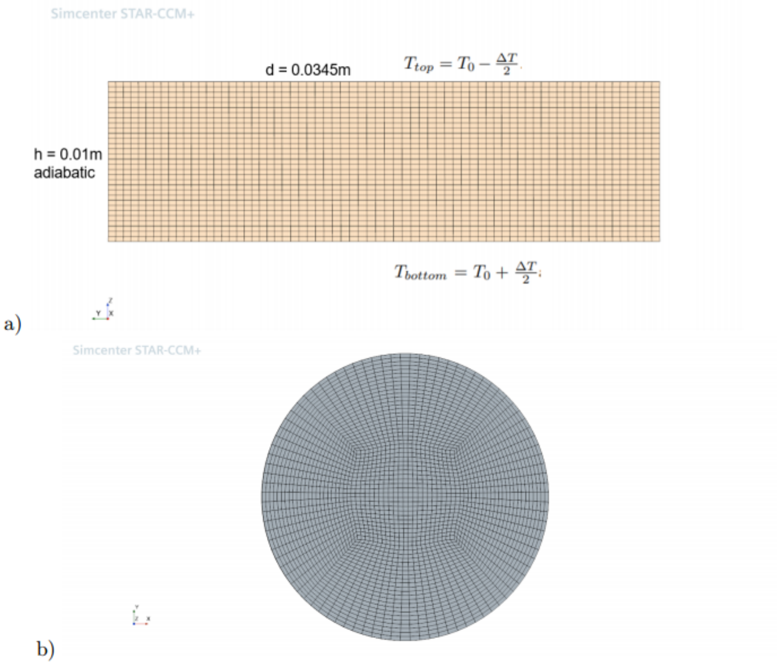
Simcenter STAR-CCM+
d = 0.0345m
$T_{top} = T_0 - \frac{\Delta T}{2}$
h = 0.01m
adiabatic
$T_{bottom} = T_0 + \frac{\Delta T}{2}$
a)
Simcenter STAR-CCM+
b)

Figure B.1: Mesh for the validation case, a) side view, b) top view

The simulation is executed by an implicit unsteady coupled DNS (direct numerical simulation) solver within StarCCM+, employing a 2nd-order temporal discretization with a consistent time step of 0.01 s. Spatial discretization is accomplished using bounded 3rd-order central differencing. The numerical computation initiates with an initial condition characterized by zero velocity and a temperature field distributed linearly. The calculation is stopped when the relative change of the Nusselt number between two time steps is smaller than 10^{-6}.

B.2. Results

Figure B.2 shows the streamline pattern and temperature distribution of the validation case. The heating of the air by the bottom surface within the cylinder results in a decrease in air density. Buoyancy forces then prompt the ascent of air from the center to the top, followed by descent from the sides back to the bottom, completing a circulation. Symmetry dictates that the gradient of the isotherms is zero at the centerline. Additionally, because of the adiabatic boundary condition of the sidewall, the gradient of the isotherms along the sidewall is also zero. The flow is laminar for the low Rayleigh number. The simulated results of isotherms and velocity vector field with Ra = 800 and Pr = 1 are similar to the validation case, as shown in Figure B.3. However, asymmetric streamlines and isotherms were observed in simulations with Ra of 700 and 750 as in Figure B.4. The temperature distribution is inclined and the velocity field is irregular. This observation may be due to the utilization of the bounded 3rd-order central difference method, which introduces numerical diffusion to the solution, whereas a second-order spatial discretization is employed in the work of Neumann.

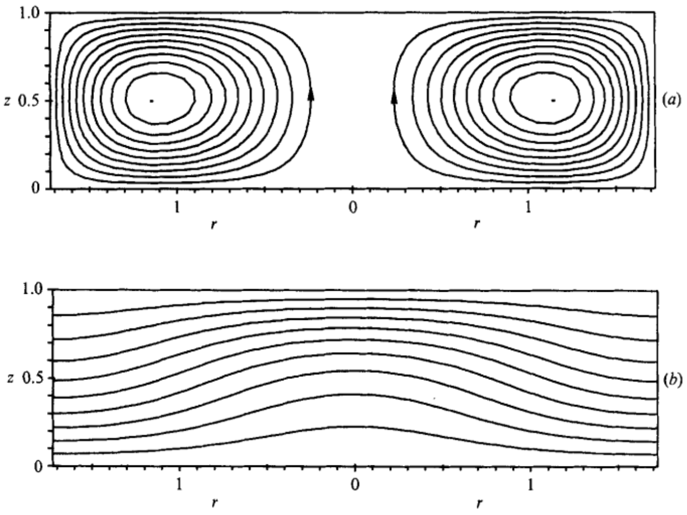

Figure B.2: streamlines and isotherms of the validation case with Ra = 700 and Pr = 1

The Nusselt number can be obtained from the simulation with different Rayleigh numbers. Figure B.5 shows the comparison of the Nusselt number from different approaches and validation cases. Generally, the simulation results are in good agreement with numerical results from Jones ea al. (Jones et al., 1976), Sackinger (Yamaguchi et al., 1984), and Neumann (Neumann, 1990). The critical Rayleigh number is 657.51, which is the start of the convective heat transfer. The Nusselt number is around 1 at Ra = 650, which means the heat transfer is pure conduction without convection, and no motion is driven. When the Rayleigh number is higher than 650, the Nusselt number also rises linearly, which shows that convection also plays a role. Besides, the flow gradually becomes turbulent. The simulation results are slightly different from the validation results from Neumann (1990), possibly due to the small difference in the Pr number.

RANS (Reynolds-averaged Navier-Stokes) models are also applied to this validation case with Ra = 850. Both realizable $k - \varepsilon$ and SST $k - \omega$ models are used. The mesh, initial conditions, and wall functions remain the same as the DNS model. Figure B.6 shows the velocity field and isotherms with SST $k - \omega$ model. The residual of Tke (turbulence kinetic energy) remains high and has almost no downward trend, which is in Appendix B. The velocity magnitude in the velocity field is extremely small and cannot be represented. Given the small Reynolds number characteristic of this validation case, the RANS model is inapplicable. Isotherms are all horizontal lines. The Nusselt number result

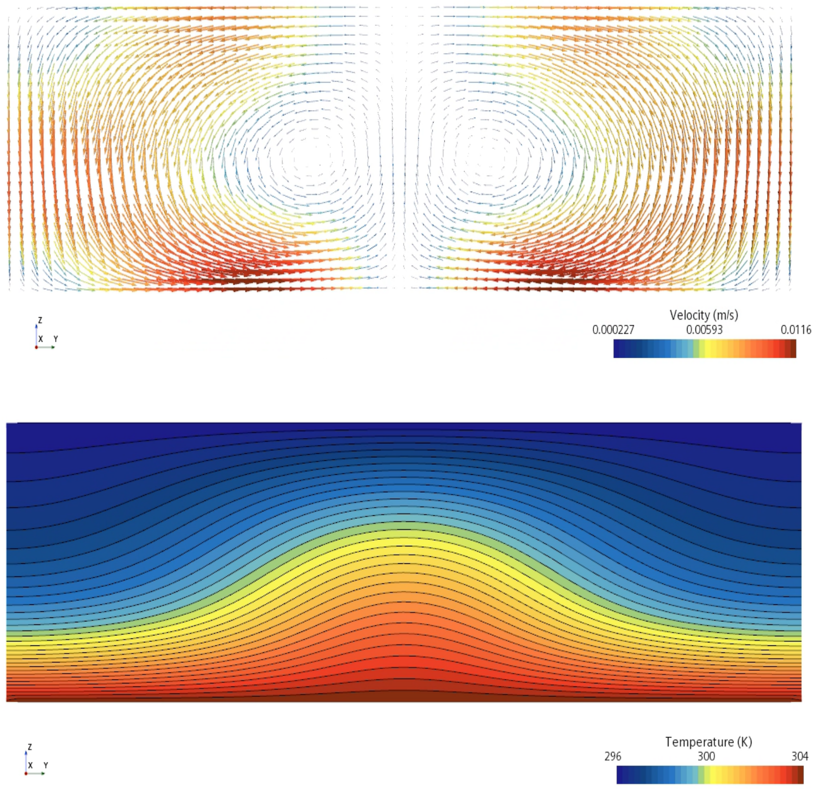

Figure B.3: velocity field and isotherms of the simulation with Ra = 800 and Pr = 1

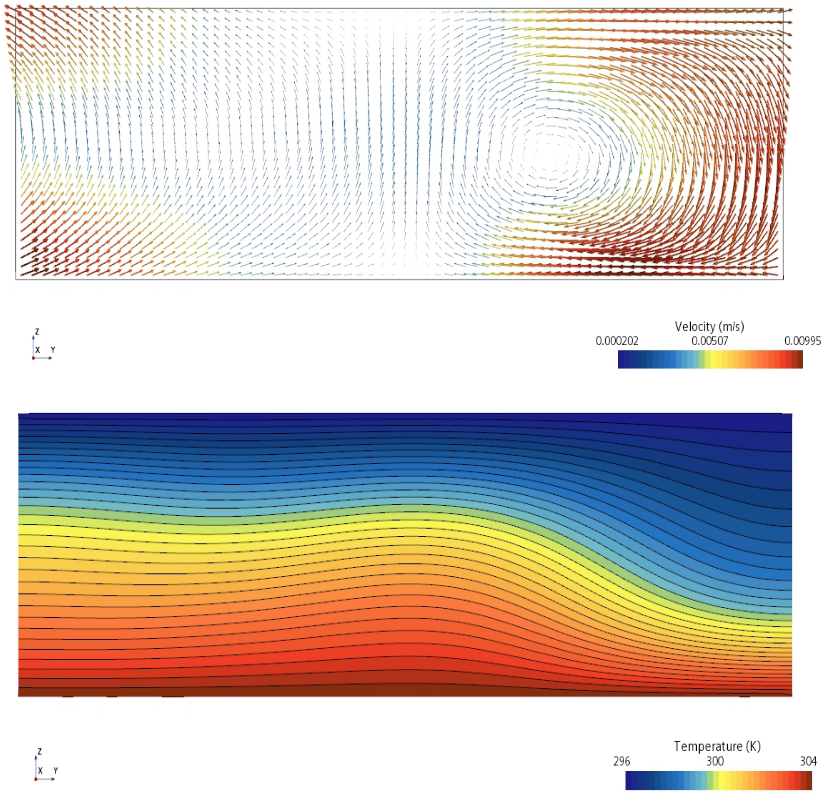

Figure B.4: velocity field and isotherms of the simulation with Ra = 750 and Pr = 1

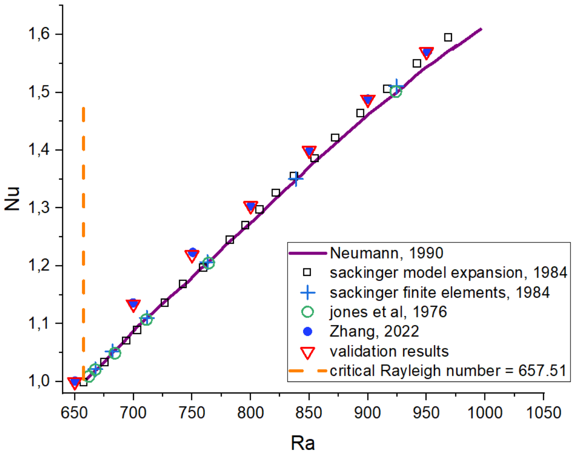

Figure B.5: Relationship between Nusselt number and Rayleigh number

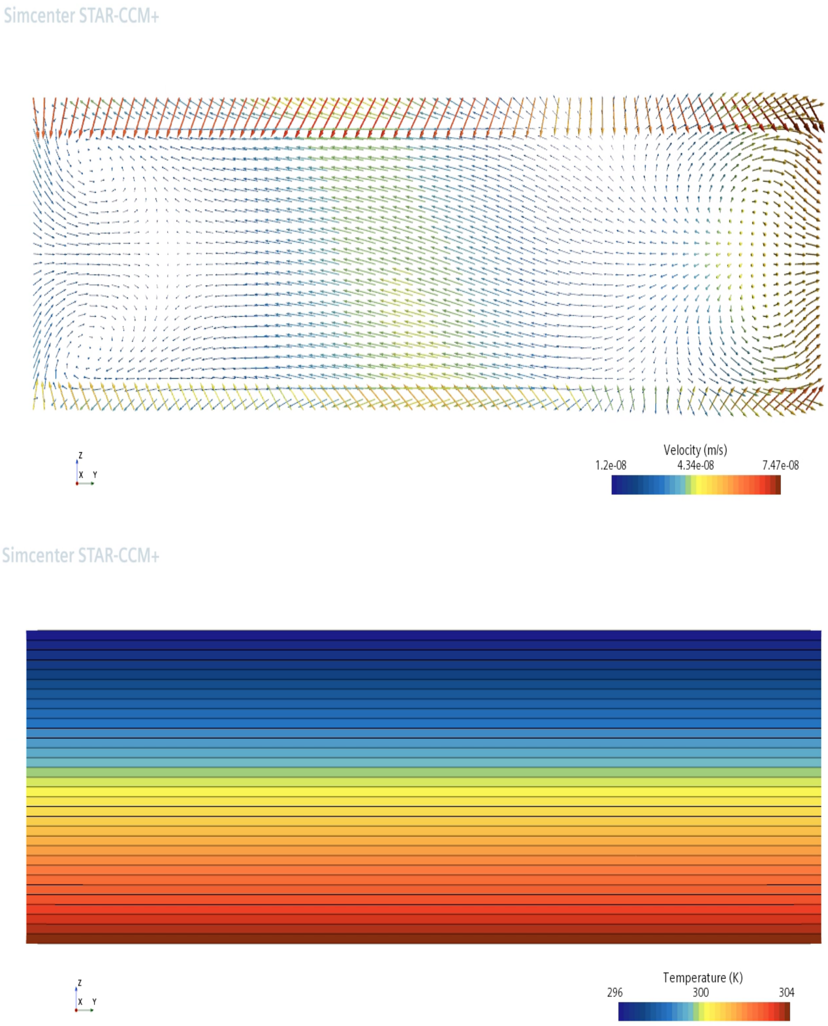
Simcenter STAR-CCM+
Z
X Y
Velocity (m/s)
1.2e-08
4.34e-08
7.47e-08
Simcenter STAR-CCM+
Z
X Y
Temperature (K)
296
300
304

Figure B.6: velocity field and isotherms of the simulation with a RANS model with Ra = 850 and Pr = 1

is close to 1, so no convective heat transfer occurs, which is not physical. The results of the realizable $k - \varepsilon$ model are similar.

Generally, the StarCCM+ code is qualified for further heat transfer analysis and applications.

C

Impact of Structured Mesh Deformation on Simulation Convergence For the full-scale model

This section describes the incompatibility issues encountered with the structured mesh of the full-scale model during the deformation process. At approximately 11 seconds of the solution time, the residuals for the energy, momentum, and continuity equations rapidly increase, leading to a simulation crash. The residual plot is shown in Figure C.1.

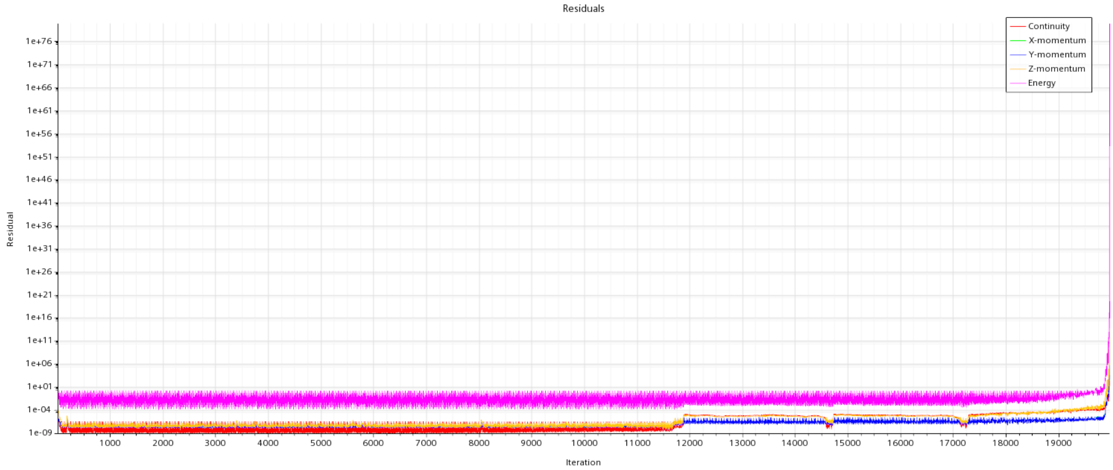

Figure C.1: Residual Explosion Plots Due to Structured Mesh Deformation for the Full-scale Model

The error output shows:
”*A floating point error has occurred. The following error has been logged:*
A non-finite residual (Energy) was added by star.segregatedenergy.SegregatedEnergySolver. Typical causes are overflow, underflow, or a division by zero.

Please check your usage and inputs."

C.1. Structured Mesh

The full-scale structured mesh uses the same meshing approach as the scaled small-size model. The Ogrid block method is applied to the top and bottom surfaces, which is shown in Figure C.2. An exponential distribution law is also used near the boundary regions. The minimum boundary grid size is 0.0001 m on both the side and top/bottom surfaces, ensuring that the wall shear stress y+ value remains below 1. The mesh consists of 50 cells in the radial direction and 120 cells in the vertical direction, with an overall mesh quality exceeding 0.7. The total number of grid cells is around 1.39 million.

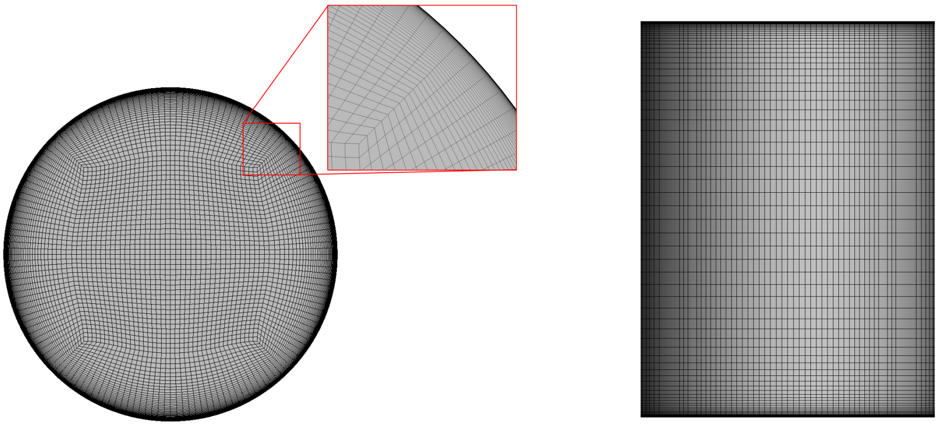

(a) Top view

(b) Side view

Figure C.2: Structured Mesh of the full-scale model

C.2. Models

The model and solver setup remain consistent with those used in the unstructured mesh simulation. The simulation employs the WALE LES turbulence model along with the segregated fluid and energy models, and an adaptive time-step model is utilized. During the expansion process, the bottom surface deformed downward at a constant speed, while the side surfaces remain floating.

C.3. Solutions

Several methods were employed to solve this issue:

- Check the mesh condition just before the crush.
  Figure C.3 shows the mesh scene just one iteration before the crash. As can be seen from the figure, before the simulation crash, the mesh did not have any irregular deformations that could potentially cause the program to crash. The mesh in the middle cut plane maintained the quadrilateral shape, and the elongation of the mesh was within acceptable standards. Therefore, it can be concluded that the mesh is not the cause of this issue.

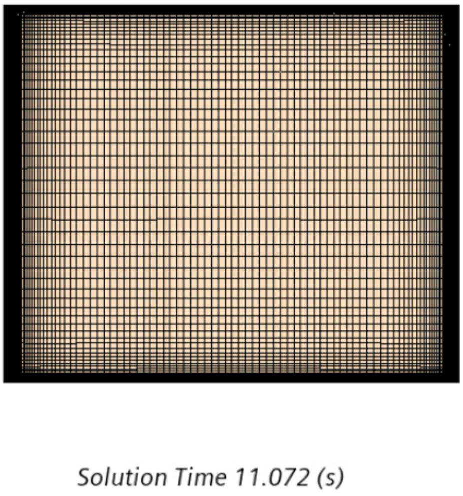

Figure C.3: The middle cut plane of the full-scale structured mesh one iteration before the crash with mesh deformation

- Increase inner iterations.

  Increasing the number of inner iterations can help reduce the residuals of energy, momentum, and continuity equations. It leads to better convergence thereby improving the stability and accuracy of the simulation. The number of inner iterations was increased from 20 to 40, and the residuals are shown in Figure C.4. As observed, the residuals still rise rapidly after a certain period, ultimately resulting in the program crashing. So this method is not considered as a solution.

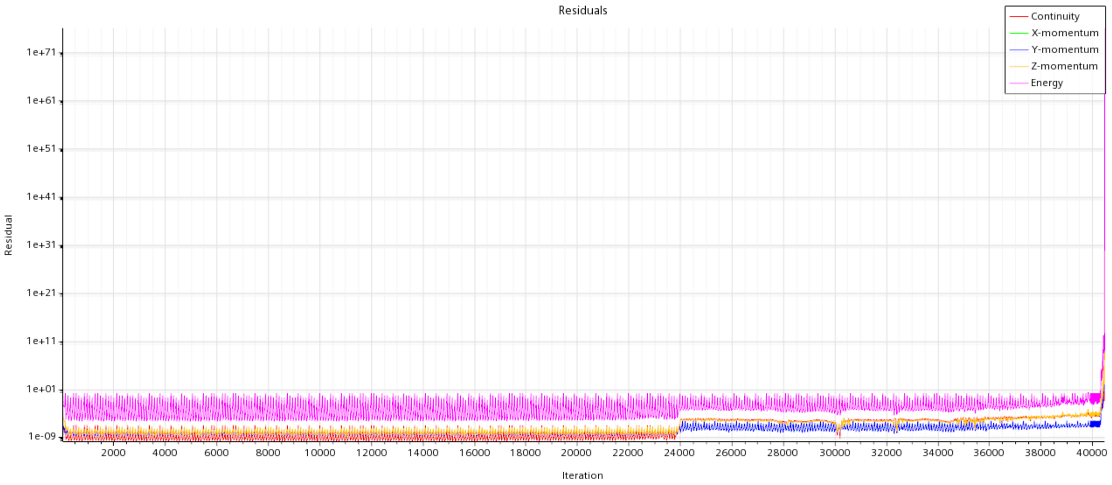

Figure C.4: Residual Explosion Plots by increasing inner iterations

- Lower the under-relaxation factor for the Segregated Energy Solver.

  Lowering the under-relaxation factor (URF) for the segregated energy solver improves numerical stability by preventing overshooting and oscillations in the energy equation. This ensures a more stable and accurate solution. The URF for the Segregated Energy Solver was reduced from 0.9 to 0.75. The residuals are shown in Figure C.5. The residuals still increase sharply after a certain period, causing the simulation to crash after maintaining this state for a while. However, due to the excessively large residuals (with energy residuals exceeding 1e50), the results during this maintained period are unreliable. Therefore, this approach is not considered a solution to the problem.

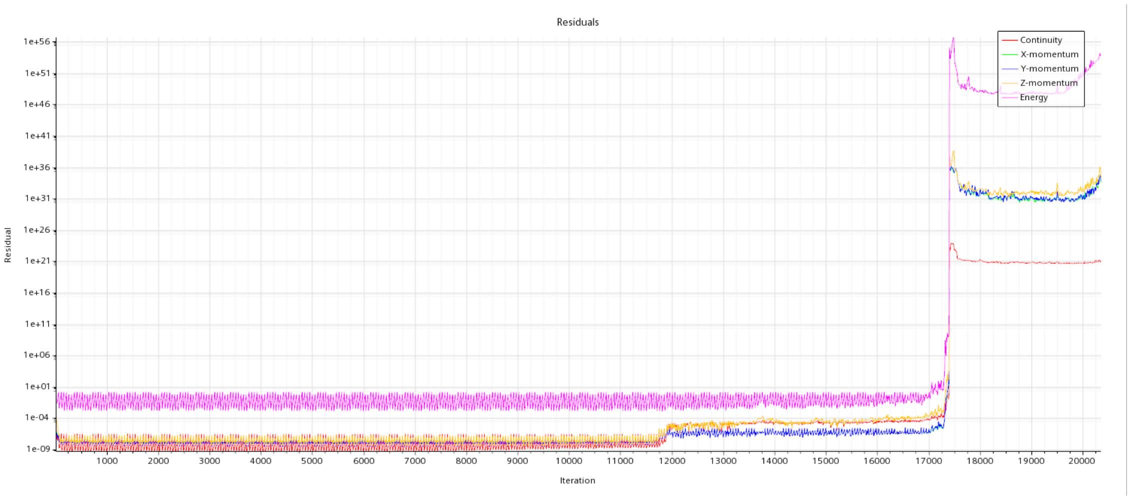

Figure C.5: Residual Explosion Plots by lowering the under-relaxation factor for the Segregated Energy solver

- Change the solver to the Coupled solver.
  A coupled solver was also employed in the simulation to investigate the sensitivity of the crash phenomenon to the choice of solver. The residuals are shown in Figure C.6. Similarly, the residuals increased rapidly after a certain period, leading to the simulation crashing. Therefore, the coupled solver was also unable to resolve the problem.

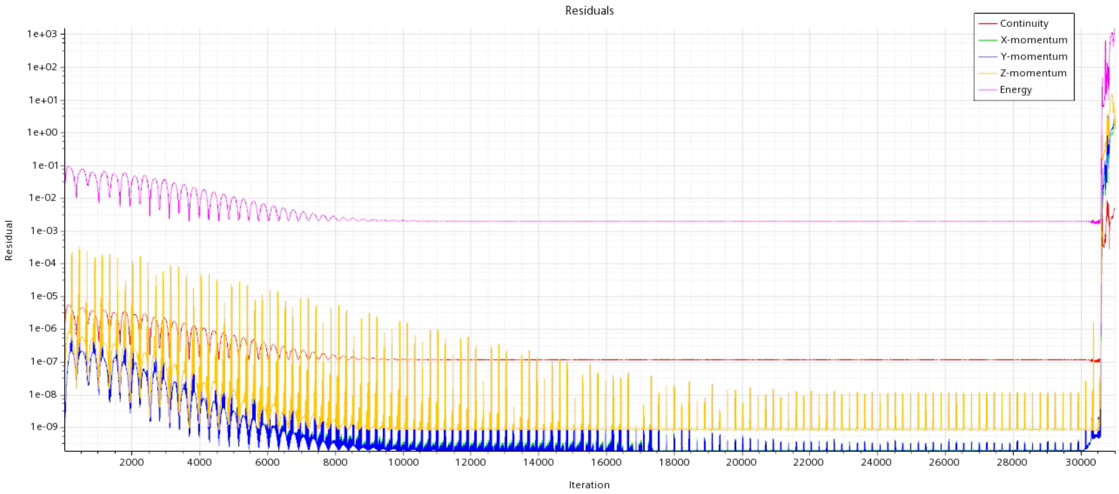

Figure C.6: Residual Explosion Plots by using the Coupled solver

C.4. Results

Therefore, when using structured mesh in the full-scale model for mesh deformation, the residuals rapidly increase after a certain period, leading to the simulation crashing. After attempting several solutions based on the error messages from the software, no improvement was observed. It can be concluded that the structured mesh deformation is incompatible with the full-scale model. Consequently, an unstructured mesh was employed in the simulation of the full-scale model.

D

Impact of the Coupled Solver on the volume change

This section describes the incompatibility of the expanding simulation when using the Coupled solver. When applying the Coupled solver along with the mesh morphing model, the internal temperature of the surge vessel does not decrease as the container volume changes.

In the scaled small-size model, using the Coupled solver and mesh morphing model, the expansion lasts for 60 seconds. Figure D.1 shows the changes in the vessel's volume and volume-averaged temperature over 60 seconds. As the volume gradually increases, the temperature change inside the vessel is minimal, amounting to only 0.02 K. This negligible temperature change can be considered insignificant. Figure D.2 shows the temperature contour of the vertical cross-section at the center of the model at 60 seconds. From the temperature range in the figure, it is evident that the internal temperature of the vessel remains nearly unchanged. Figure D.3 shows the residual plot from the simulation.

Due to this incompatibility, the Segregated solver was used for the expanding simulations.

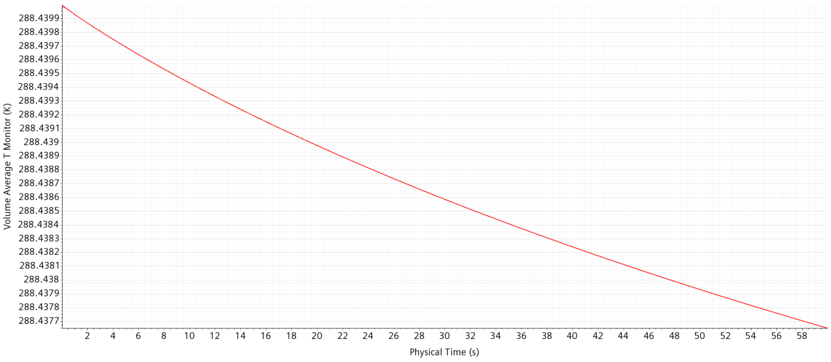

(a) temperature

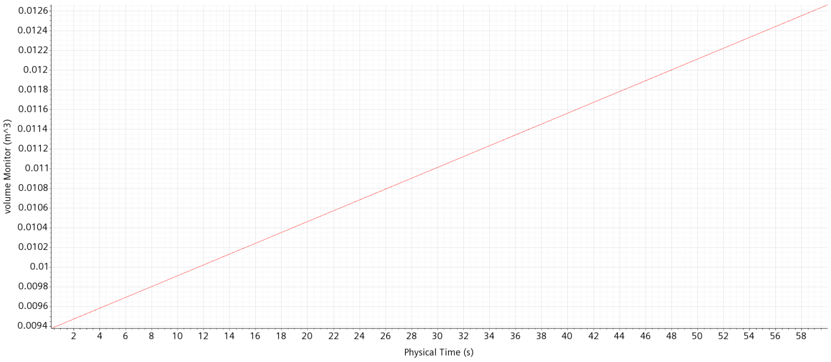

(b) volume

Figure D.1: Temperature and volume plots for the scaled small-size model simulation with the Coupled solver and mesh morphing model

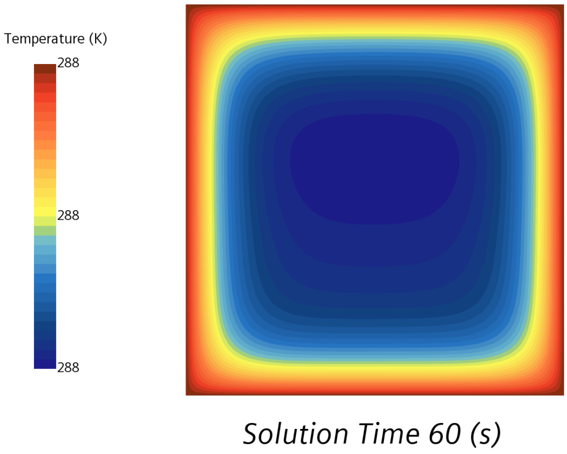

Figure D.2: Temperature contour on the vertical cut plane for the scaled small-size model simulation with the Coupled solver and mesh morphing model

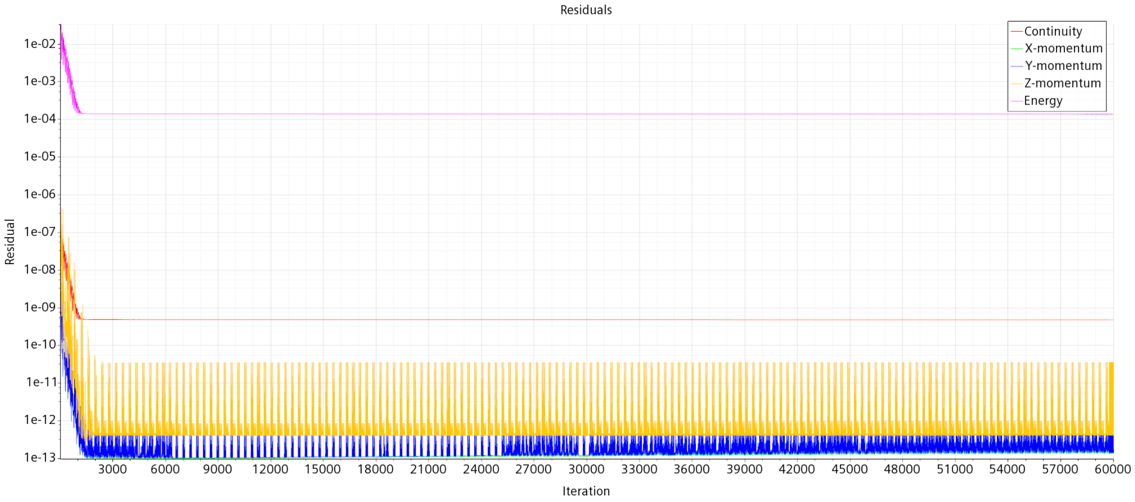

Figure D.3: Residual plot for the scaled small-size model simulation with the Coupled solver and mesh morphing model

E

Non-expanding simulation results

This chapter primarily describes the results of the non-expanding simulations, where the model's volume remains constant throughout the simulation. The initial volume is set to the final volume, with the initial air temperature at the measured lowest value of 273 K. The initial wall, top, and bottom surface temperatures are set to the ambient temperature of 288.44 K.

Simulations were conducted for both the scaled small-size and full-scale models. At 400 seconds, the full-scale model reached a volume-averaged temperature of 285 K, while at 60 seconds, the scaled small-size model achieved a volume-averaged temperature of 288 K.

E.1. Full-Scale

The temperature contours for the non-expanding full-scale simulation are shown in Figure E.1. It can be observed that in the non-expanding simulation, the temperature rises more quickly, but the overall trend and the conservation of energy and mass are consistent with the expanding simulation. Given the initial temperature difference between the inside and outside, the internal air takes some time to reach the velocity and temperature fields observed in the expanding simulation. However, since the non-expanding simulation does not account for the impact of bottom surface movement, the heat transfer within the container is relatively stable. Over time, it can be seen that the high-temperature air at the top gradually moves downward. It is unlike that in the expanding simulation where the high-temperature air accumulates at the top until the expansion stops, then it begins to move downward.

Figure E.2 shows the temperature changes for each sensor, with sensors at the same height represented by similar colors. It can be observed that sensors at the same height have similar temperatures, while there is a small difference in temperatures between sensors at different heights.

Figure E.3 compares the sensor temperatures from the non-expanding full-scale simulation with the experimental measurements. To better compare the two, the initial time for the simulation is set to 25 seconds after the experiment began, with experimental results shown in gray. It can be observed that before the expansion stops, the simulated temperatures are higher than the experimental data. However, after the expansion ceases, the simulated temperatures are lower than the experimental results for a

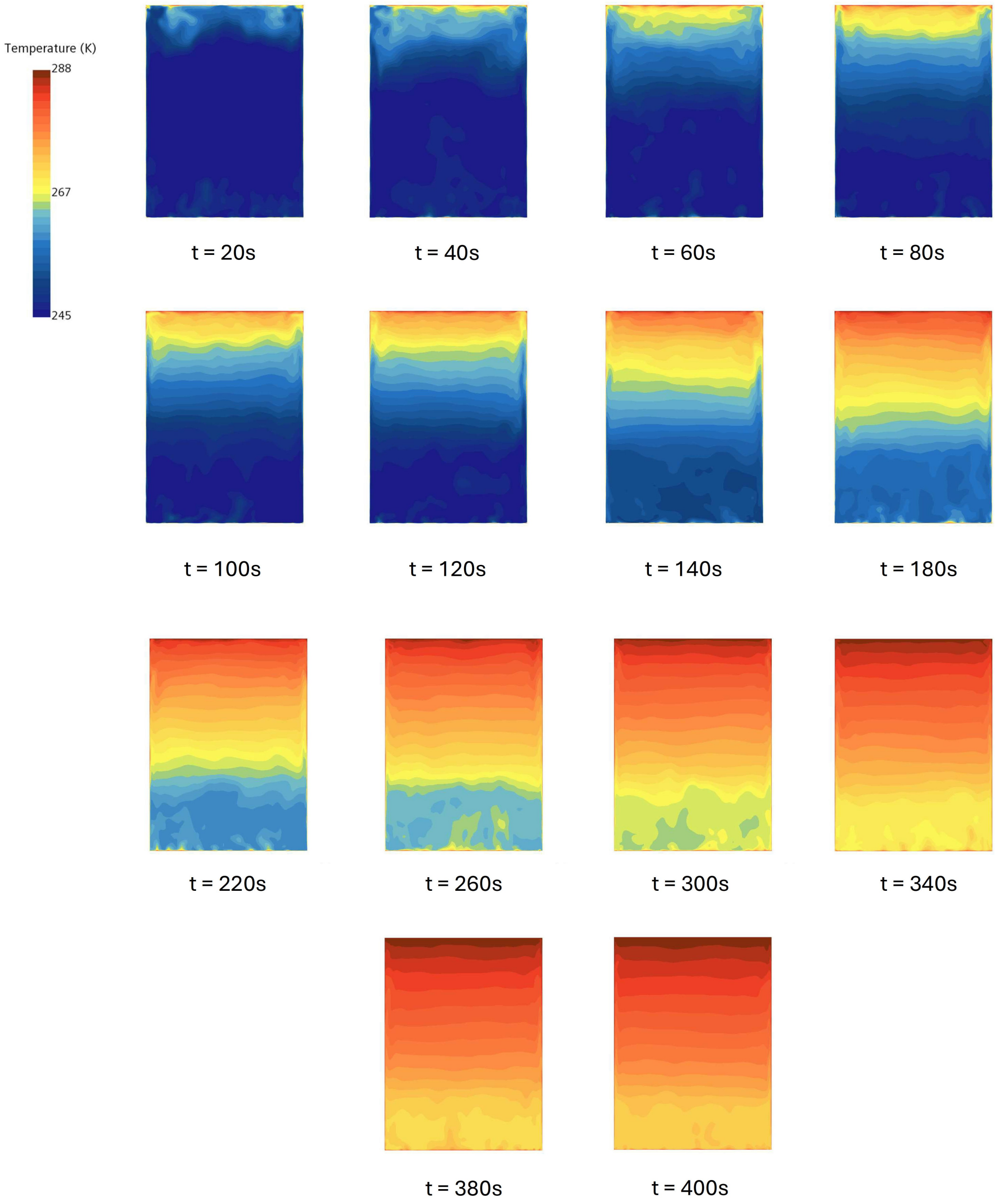

t = 20s t = 40s t = 60s t = 80s

t = 100s t = 120s t = 140s t = 180s

t = 220s t = 260s t = 300s t = 340s

t = 380s t = 400s

Figure E.1: Temperature field for the non-expanding full-scale model on the middle vertical plane at different times

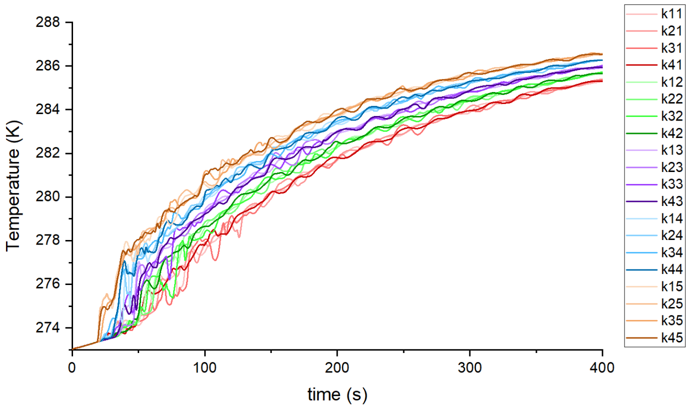

Figure E.2: Temperature probe for the non-expanding full-scale model

certain period.

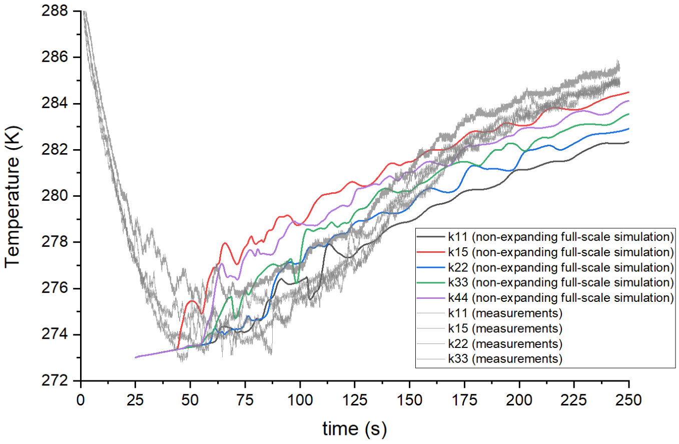

Figure E.3: Temperature probe comparison between the measurements and the non-expanding full-scale simulation

E.2. Scaled Small-size

For the non-expanding scaled small-size simulation, the simulation reached the ambient temperature within just 60 seconds, significantly surpassing the results observed in the expanding and full-scale simulations.

Figure E.4 shows the temperature changes at the sensors during the simulation. It can be observed that after 3 seconds, the temperature changes significantly across the sensors. The k15 sensor increased by 8 K within just 1 second, indicating a pronounced heating effect. However, this temperature variation cannot be directly compared with the experimental measurements.

E.3. Conclusion

For the non-expanding simulation, heat transfer occurs significantly faster than in the expanding simulation. Moreover, the simulation requires a period to initialize the flow field, making it difficult to compare the results with experimental measurements directly. Additionally, the initial conditions for the non-

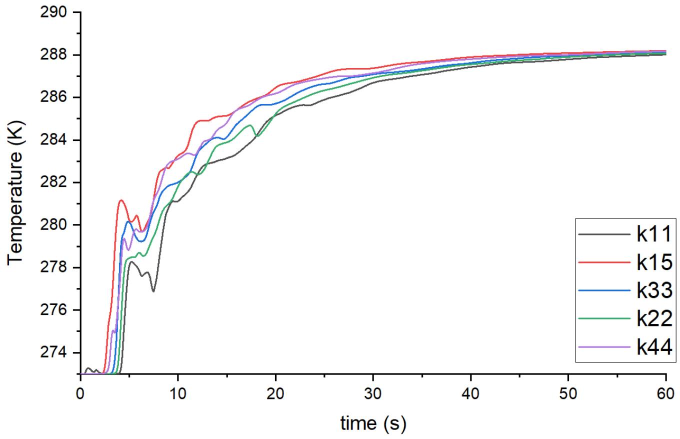

Figure E.4: Temperature probe for the non-expanding scaled small-scale model

expanding simulation depend on experimental data, such as the minimum temperature observed. This makes the simulation challenging to conduct without specific experimental data and limits its ability to validate the experimental measurements.

F

Convergence Plots of the expanding simulations

This chapter primarily presents the residuals and time step plots for the expanding simulations of both the full-scale and scaled small-size models, as shown in Figure F.1 and F.2. The results demonstrate the convergence of continuity, momentum, and energy in the simulations, confirming the stability and accuracy of the simulation processes. The time step is determined by the CFL (Courant–Friedrichs–Lewy) number. In the simulation, the mean CFL number is set to 0.85, with a maximum CFL number of 0.95.

For the full-scale model simulation, the residuals of the momentum and continuity equations remain below 1e-8, while the energy equation residual is maintained around 1e-4. The maximum time step is initially 0.01 s, but it decreases around 10 s due to an increase in the boundary layer velocity near the sides, which requires a reduction in the time step to maintain stable CFL numbers. Subsequently, the time step oscillates around 0.0045 s. After the expansion stops at 124.2 s, the time step gradually increases back to 0.01 s as the internal temperature rises and the boundary layer velocity decreases, consistent with the discussion in Chapter 5.

For the scaled small-size model, the residual plots are similar to those of the full-scale model. After the expansion ends, the residual of the energy equation gradually decreases. Regarding the time step, the scaled small-size simulation experiences less reduction compared to the full-scale model and remains relatively stable. This is attributed to the lower airflow velocities within the scaled small-size model.

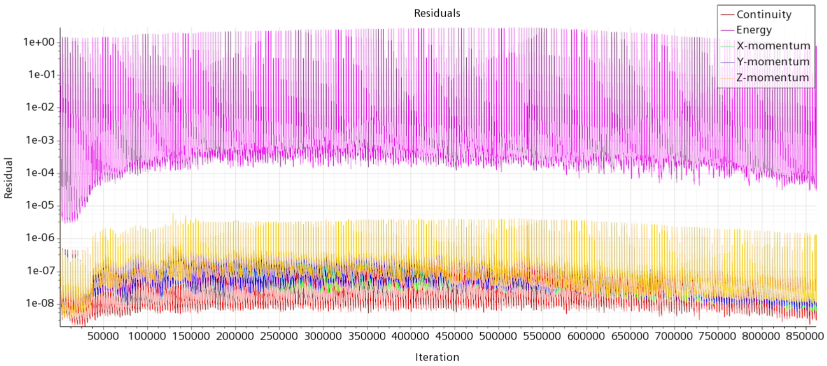

(a) residuals

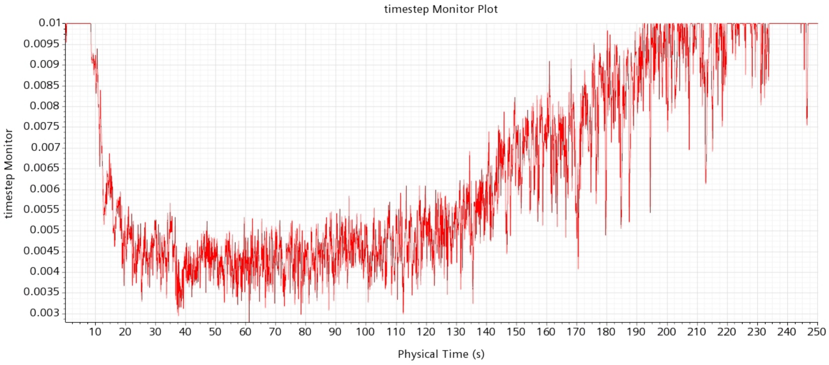

(b) time step

Figure F.1: Residuals and time step monitor for the full-scale model simulation

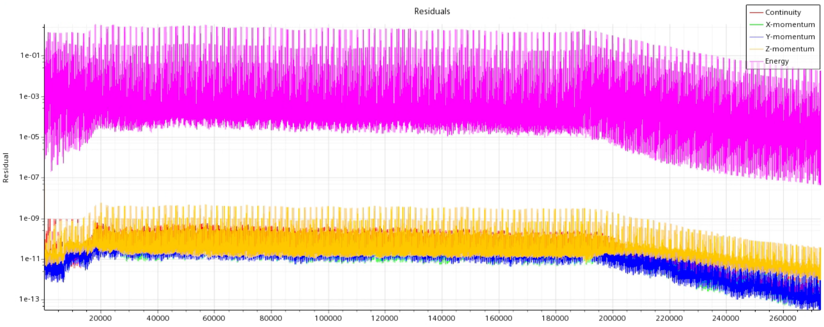

(a) residuals

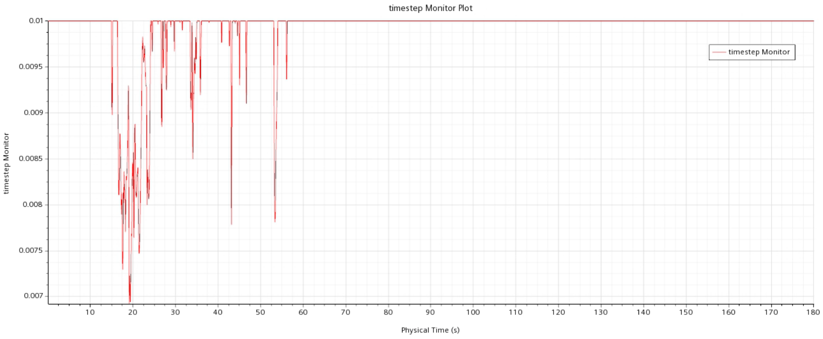

(b) time step

Figure F.2: Residuals and time step monitor for the scaled small-size model simulation

G

Measurement Data for the Simulation Case 1 & 2 in the Experiment

This chapter presents the original measurement data used for simulating Case 1 [1] and Case 2 [2]. The data visualization was done using the ReadBinFile software. The initial temperature, pressure conditions, air domain height, height changing rate, and relative humidity data for the simulations were all derived from the measurement data.

The temperature sensor data is used to compare and validate the simulation results. The differential pressure data is used to calculate the water surface height and height changing rate, thereby determining the air domain height and its rate of change, as described in Section 3.1. The valve position data provides the valve opening time, which corresponds to the expansion time in the simulation. The pressure data is used to set the initial pressure in the simulation and to validate the analytical estimation results using the RHT model. The ambient temperature data is the initial temperature and wall temperature in the simulation.

G.1. Case 1

G.1.1. Temperature probes measurements

k-type probes

The temperature of k-type probes on the first beam at different heights are in Figure G.1.

The temperature of k-type probes on the second beam at different heights are in Figure G.2.

The temperature of k-type probes on the third beam at different heights are in Figure G.3.

The temperature of k-type probes on the third beam at different heights are in Figure G.4.

---

[1] The data is from the Deltares experiment ID 38, with the specific file path:" P:\11210289-006-svthermodynamics2024\experiment data\test-setup\meetdata\BlauwVat\BlauwVat038.dat".

[2] The data is from the Deltares experiment ID 14, with the specific file path:" P:\11210289-006-svthermodynamics2024\experiment data\test-setup\meetdata\BlauwVat\BlauwVat014.dat".

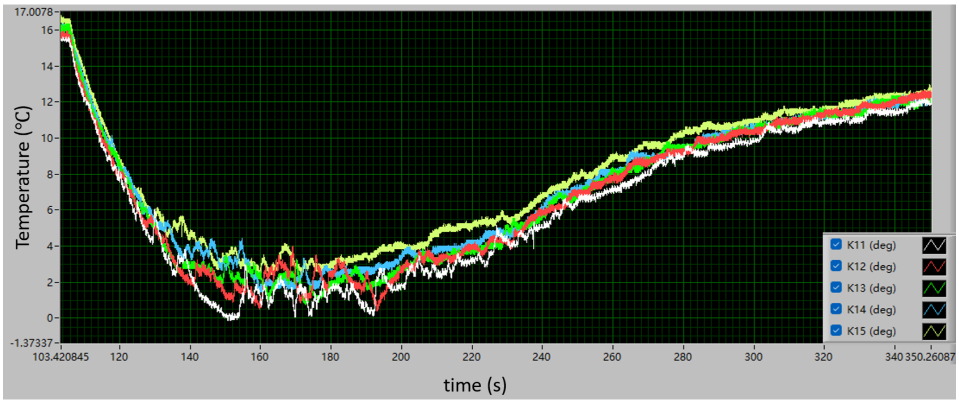

Figure G.1: Measurement data from the temperature sensors on the first beam in the experiment for case 1

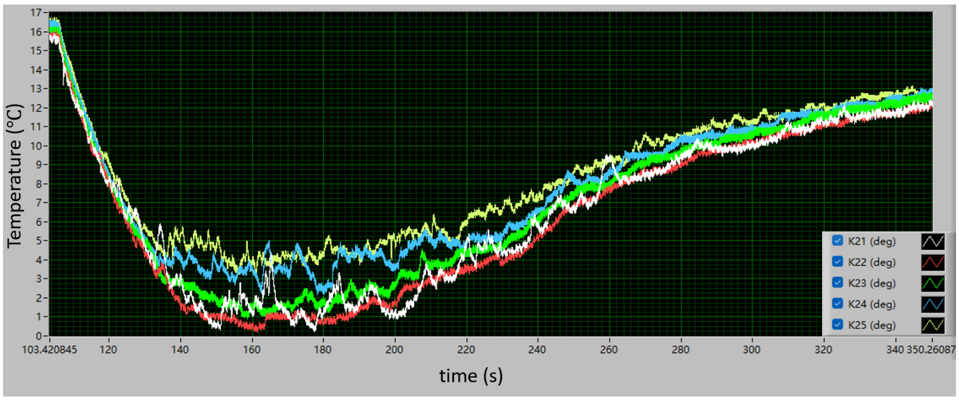

Figure G.2: Measurement data from the temperature sensors on the second beam in the experiment for case 1

t-type probes

The temperature of t-type probes are in Figure G.5.

G.1.2. Other measurements

The differential pressure monitor is shown in Figure G.7.

The pressure monitor is shown in Figure G.7.

The relative humidity monitor is shown in Figure G.8.

The ambient temperature monitor is shown in Figure G.9.

The valve position monitor is shown in Figure G.10.

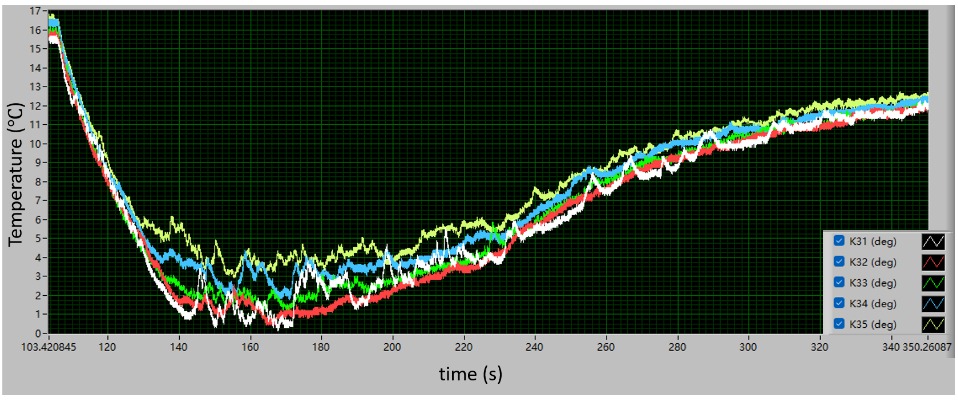

Figure G.3: Measurement data from the temperature sensors on the third beam in the experiment for case 1

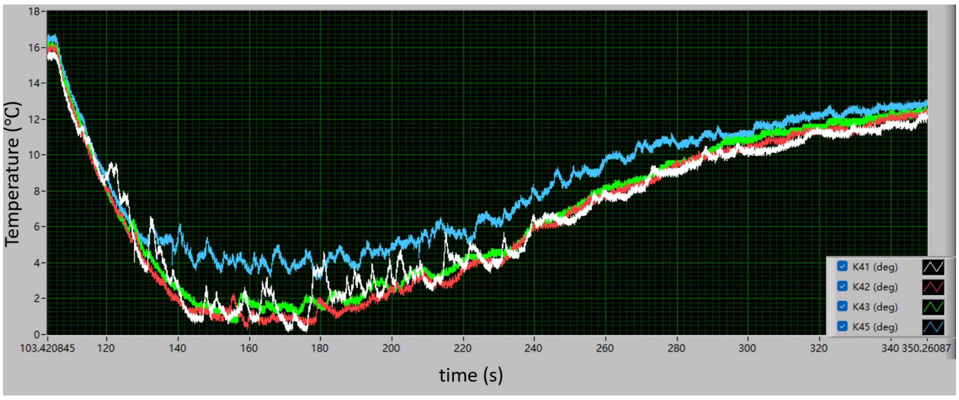

Figure G.4: Measurement data from the temperature sensors on the fourth beam in the experiment for case 1

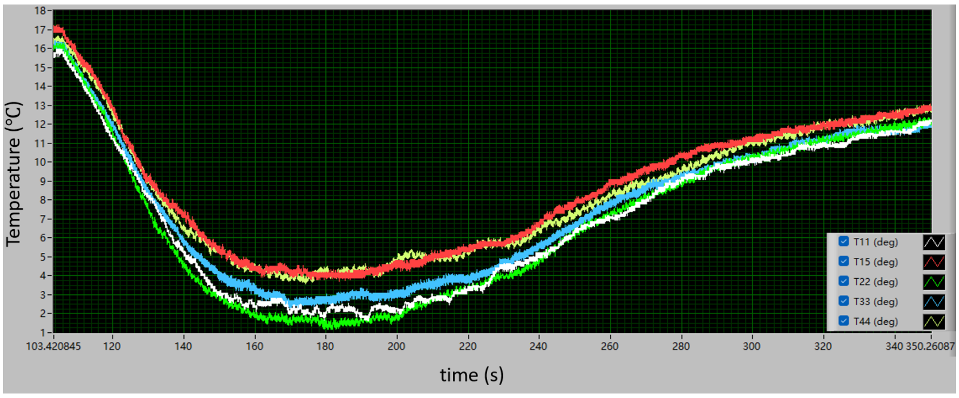

Figure G.5: Measurement data from the t-type temperature sensors in the experiment for case 1

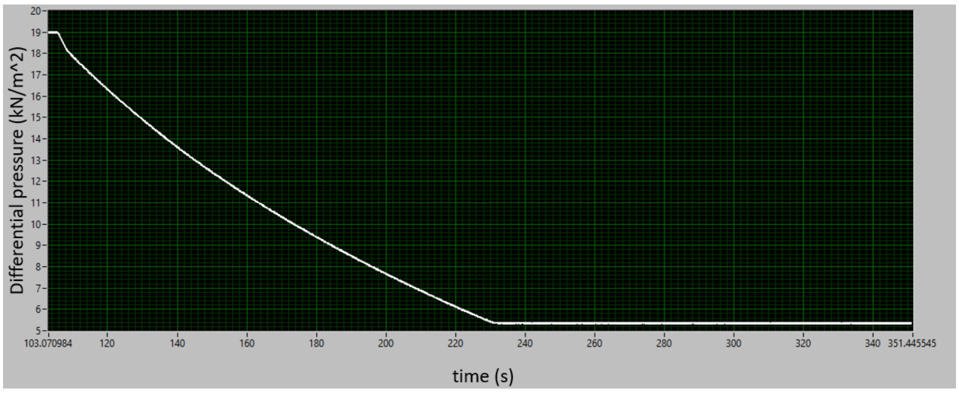

Figure G.6: Measurement data from the differential pressure sensor in the experiment for case 1

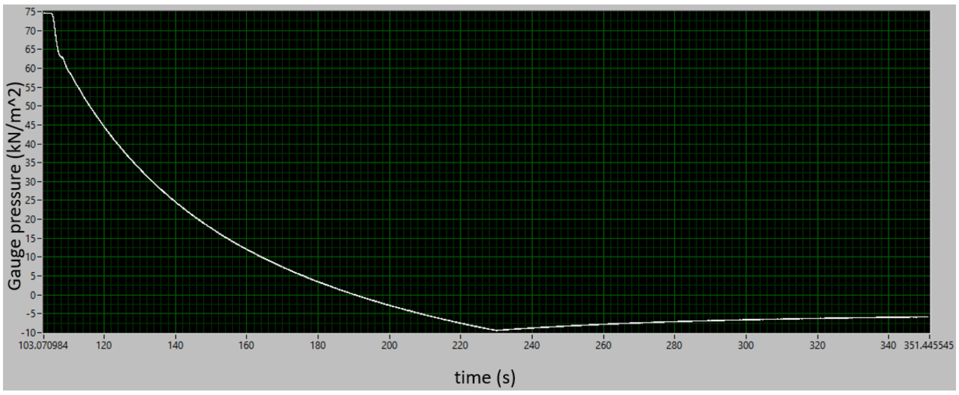

Figure G.7: Measurement data from the pressure sensor in the experiment for case 1

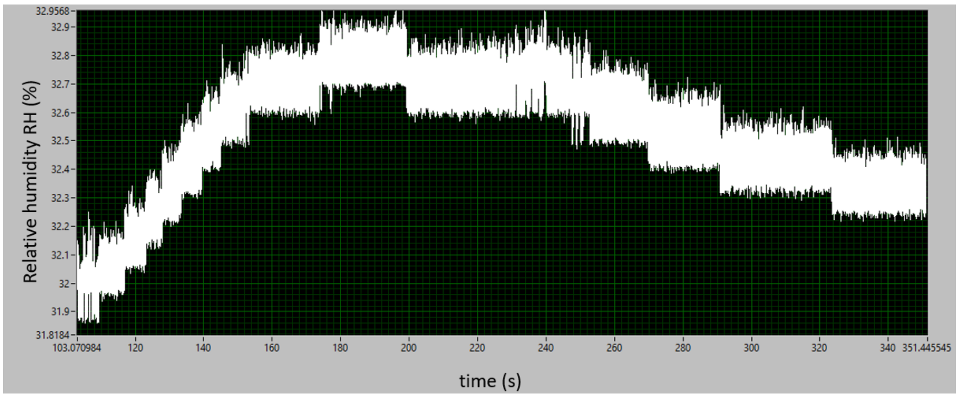

Figure G.8: Measurement data from the relative humidity sensor in the experiment for case 1

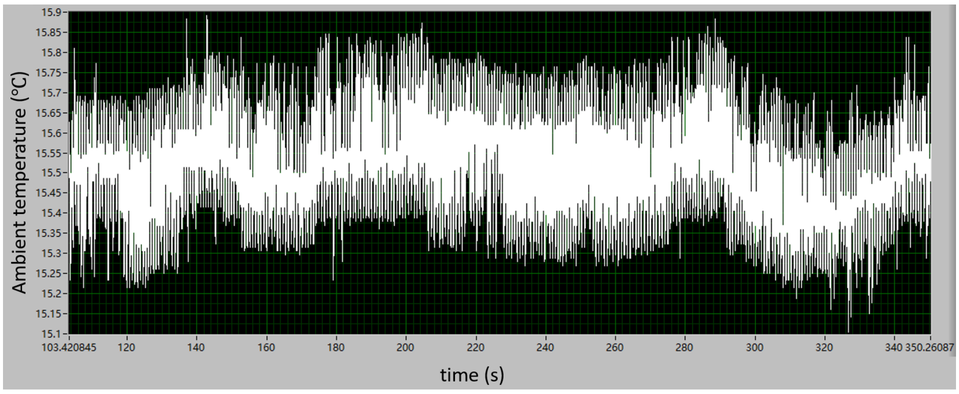

Figure G.9: Measurement data from the ambient temperature sensor in the experiment for case 1

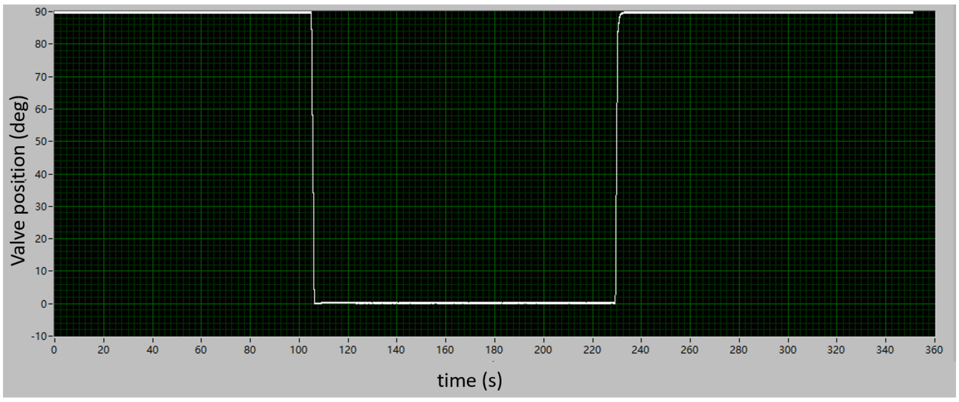

Figure G.10: Measurement data from the valve position sensor in the experiment for case 1

G.2. Case 2

G.2.1. Temperature probes measurements

k-type probes

The temperature of k-type probes on the first beam at different heights are in Figure G.11.

The temperature of k-type probes on the second beam at different heights are in Figure G.12.

The temperature of k-type probes on the third beam at different heights are in Figure G.13.

The temperature of k-type probes on the third beam at different heights are in Figure G.14.

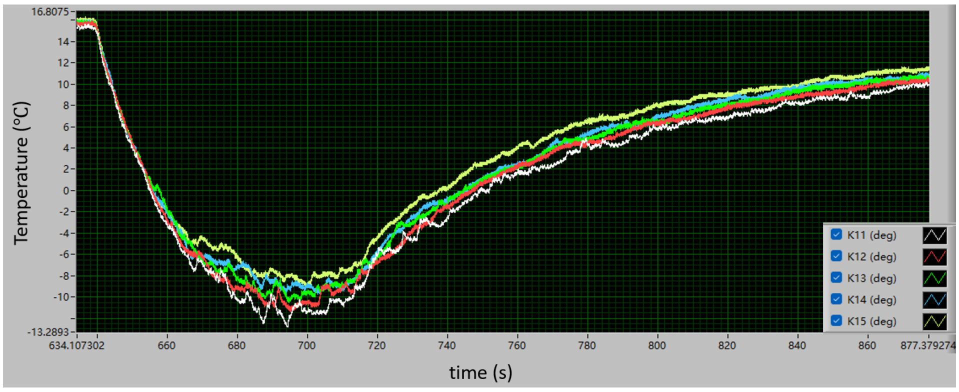

Figure G.11: Measurement data from the temperature sensors on the first beam in the experiment for case 2

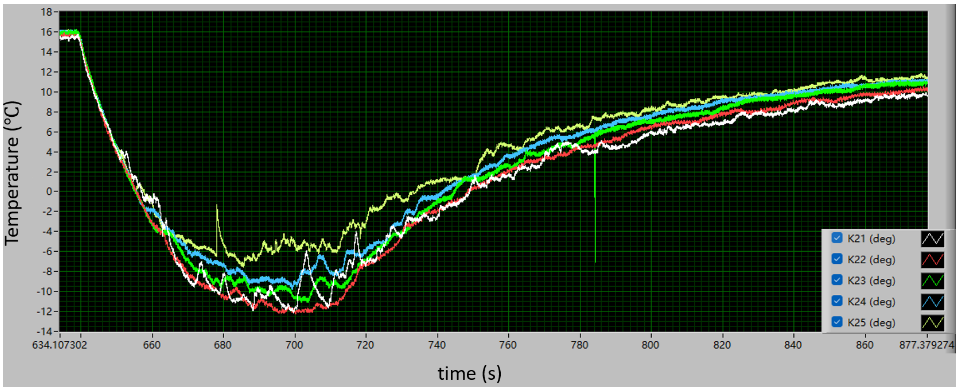

Figure G.12: Measurement data from the temperature sensors on the second beam in the experiment for case 2

t-type probes

The temperature of t-type probes is in Figure G.15.

G.2.2. Other measurements

The differential pressure monitor is shown in Figure G.17.

The pressure monitor is shown in Figure G.17.

The relative humidity monitor is shown in Figure G.18.

The ambient temperature monitor is shown in Figure G.19.

The valve position monitor is shown in Figure G.20.

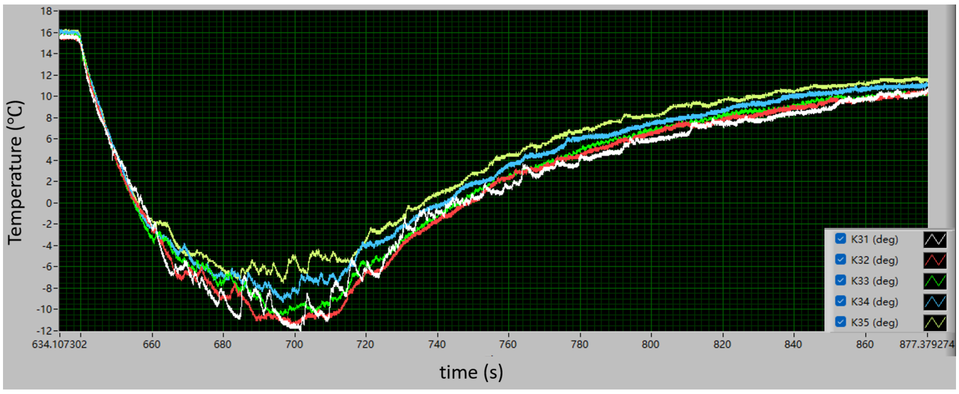

Figure G.13: Measurement data from the temperature sensors on the third beam in the experiment for case 2

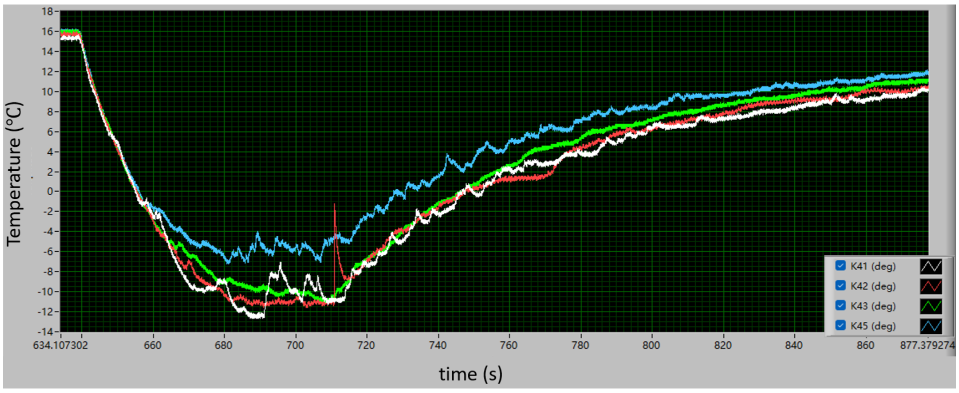

Figure G.14: Measurement data from the temperature sensors on the fourth beam in the experiment for case 2

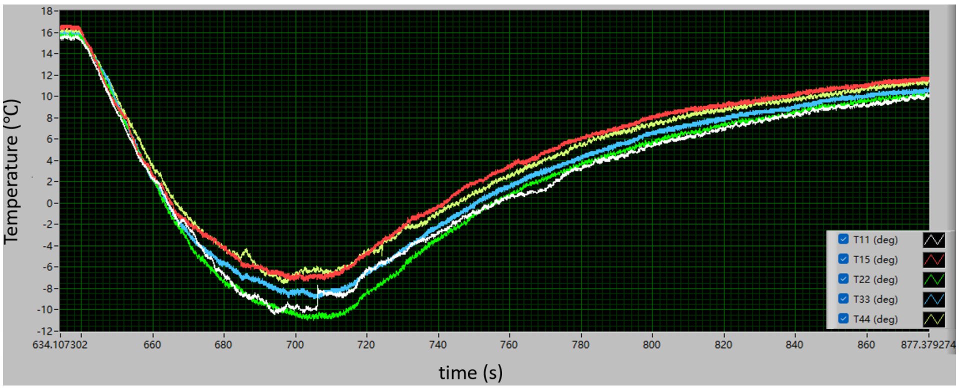

Figure G.15: Measurement data from the t-type temperature sensors in the experiment for case 2

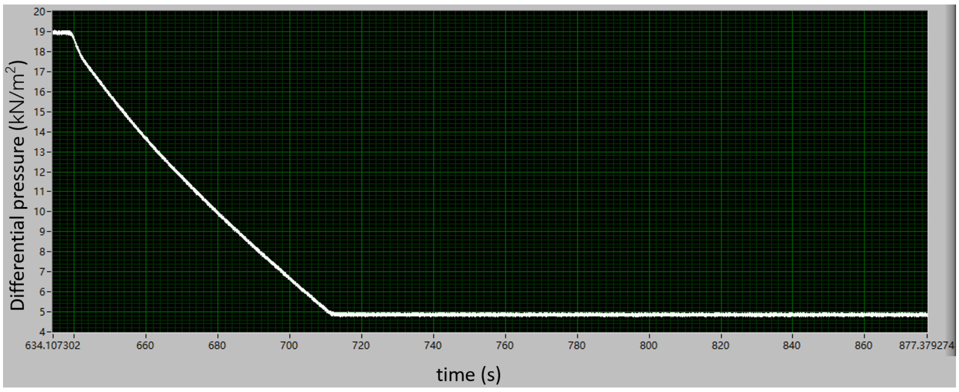

Figure G.16: Measurement data from the differential pressure sensor in the experiment for case 2

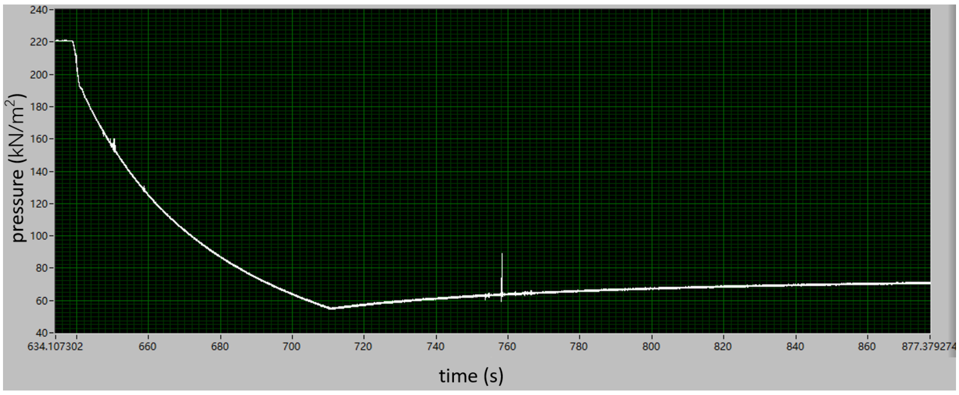

Figure G.17: Measurement data from the pressure sensor in the experiment for case 2

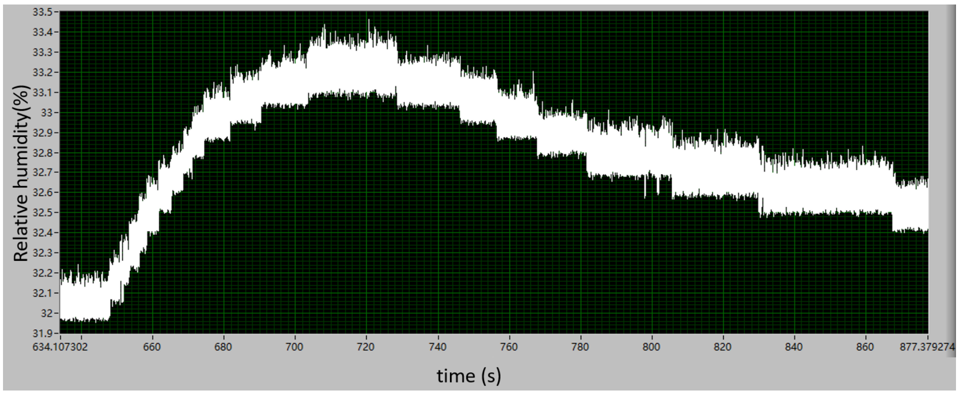

Figure G.18: Measurement data from the relative humidity sensor in the experiment for case 2

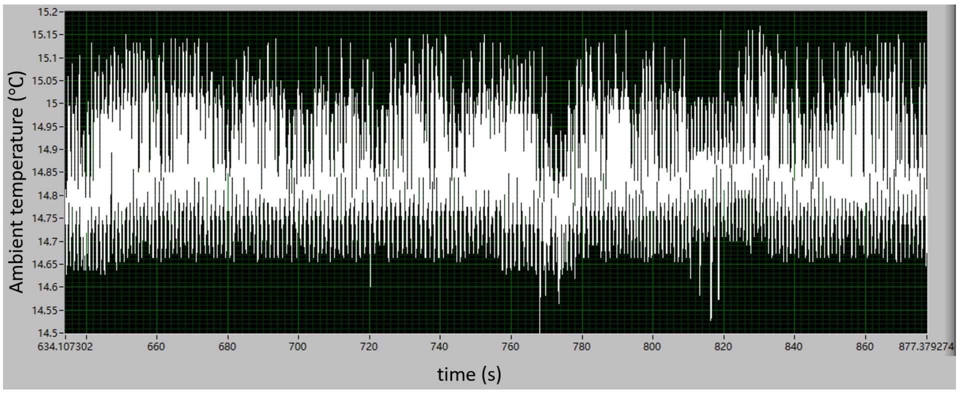

Figure G.19: Measurement data from the ambient temperature sensor in the experiment for case 2

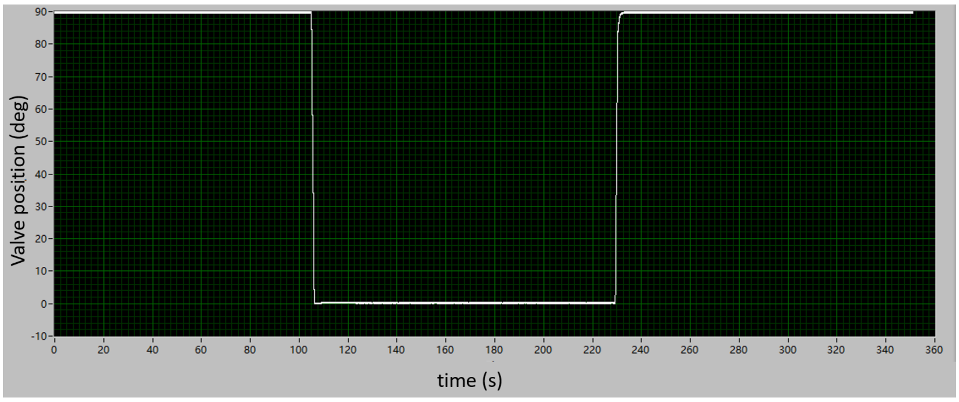

Figure G.20: Measurement data from the valve position sensor in the experiment for case 2

H

Impact of the Heated Frame on Thermocouple Measurements

This chapter provides a simple simulation validation for the assumption proposed in Section 5.3.3. The simulation places a heated aluminum frame inside the vessel and introduces several temperature sensors to investigate the impact of the heated frame on temperature measurements.

H.1. Geometry & Boundary Conditions

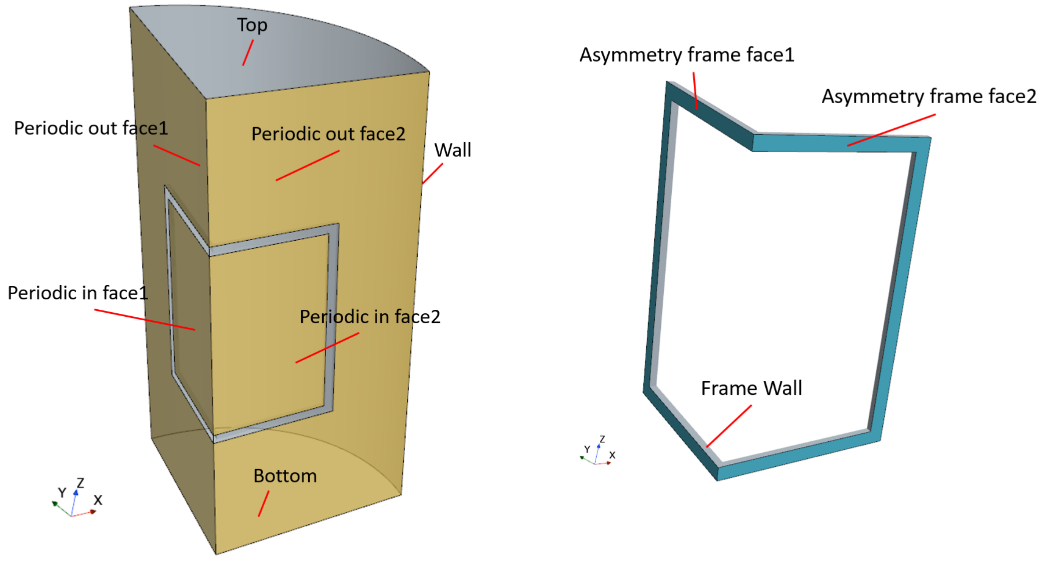
Top
Periodic out face1
Periodic out face2
Wall
Periodic in face1
Periodic in face2
Bottom
Y
Z
X
Asymmetry frame face1
Asymmetry frame face2
Frame Wall
Y
Z
X

(a) fluid region (air)

(b) solid region (Al frame)

Figure H.1: Geometry and names in the frame simulation

Figure H.1 shows the geometry and names in the frame simulation. Given that the flow is expected to be laminar and the model is symmetrical, only one-quarter of the vessel and the frame is simulated to reduce computational costs. The distance between the frame and the top surface is consistent with the experiment, and the distance between the frame and the bottom surface is set equal to that of the top. Therefore, this model represents a snapshot of the air during the expansion process.

In the model, the air domain and the solid (frame) domain are modeled separately. The intermediate boundary within the air domain is defined as rotational periodic, with the axis being the vertical centerline. The top, bottom, and wall surfaces are set as adiabatic boundaries. The initial temperature of the air domain is set to 265 K, derived as the midpoint of the average temperature from various thermocouples in both the simulation and experimental results for Case 1.

The solid domain represents the aluminum frame, with its dimensions estimated based on measurements. The boundary conditions for the two cross-sectional planes are set to symmetry. The temperature of the frame is set to 288 K, consistent with the initial air temperature in both the simulation and experiment.

H.2. Mesh

A structured mesh was applied to both the solid and fluid domains. The mesh configuration is shown in Figure H.2 and H.3. The O-grid meshing strategy was applied to the top and bottom surfaces of the cylinder to minimize mesh distortion on the curved surfaces. The number of cells for the frame is 1,638, and the overall number of cells is 1.5 million. The overall mesh quality exceeded 0.55.

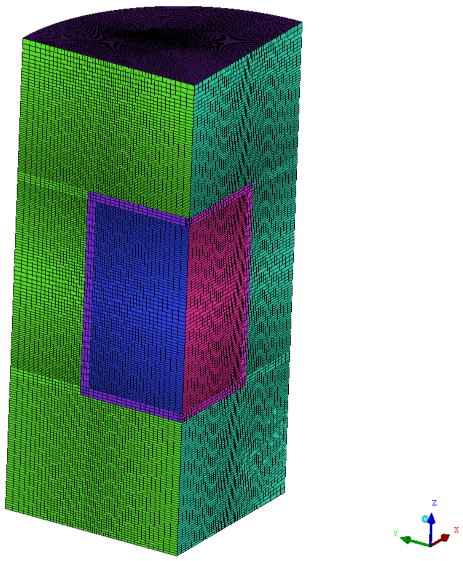

Figure H.2: Mesh of the frame simulation

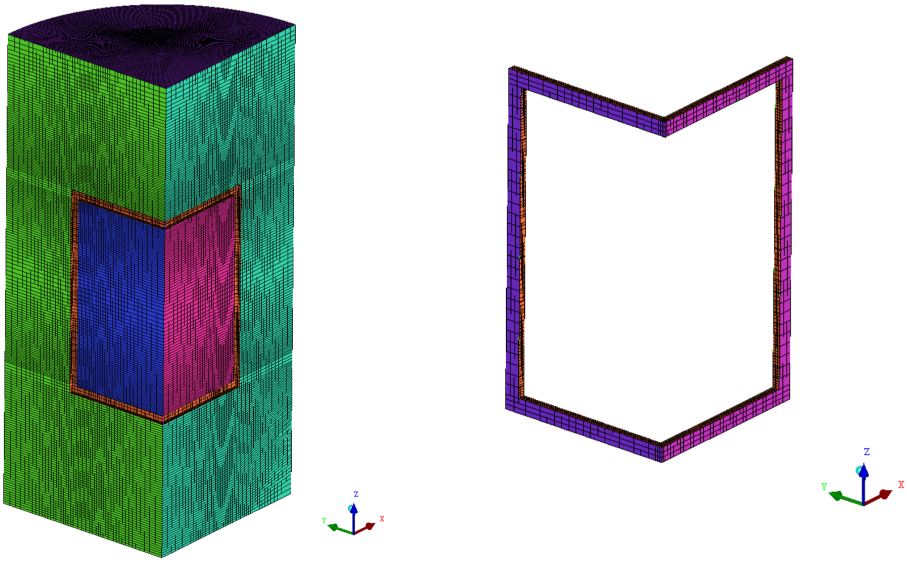

(a) fluid region (air) (b) solid region (Al frame)

Figure H.3: Mesh of the frame simulation for fluid and solid regions

H.3. Results

Figure H.4 shows the temperature contour of the x-z cross-section at t = 86.6 s, where the red dots represent the locations of the thermocouples. The heated frame warms the air inside the vessel. Due to buoyancy, the heated air rises upwards. The upward movement of heated air is more obvious above the frame, and it is also clear that the thermocouple positions are affected to some extent by this flow.

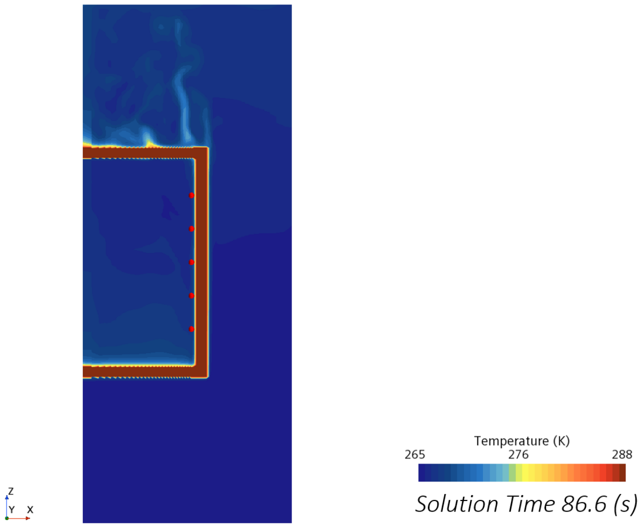

Figure H.4: Temperature contour for the frame simulation at t = 86.6 s (red dots: location of thermocouples)

To quantitatively analyze the effect of heat flow on the thermocouples, five probes were placed 3 cm horizontally away from the frame, as shown in Figure H.5. The vertical distance between each probe was set to 0.2 m, the same as the experimental setup. Figure H.6 shows the temperature variation of these five probes over time. It can be observed that Point 3, the highest probe, has the greatest influence, with a maximum temperature fluctuation of 4.5 K. Overall, the temperature fluctuations decreased after 35 seconds, stabilizing to a difference of 1-2.5 K from the initial air temperature. This demonstrates that while the heated frame does impact the thermocouple readings, the effect is relatively small.

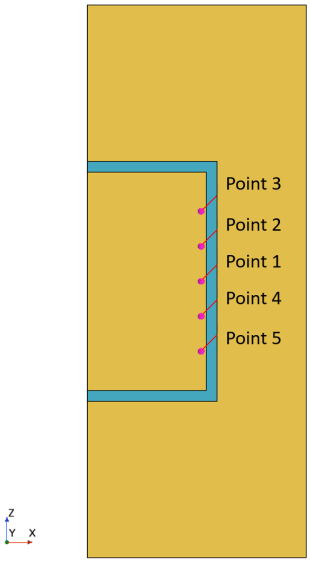

Figure H.5: Locations of probes for the frame simulation

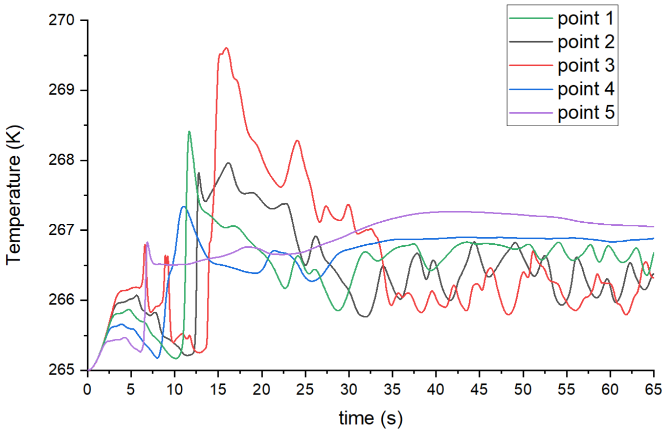

Figure H.6: Temperature on the probes for the frame simulation

This simulation is only a simple test, and at the time of writing, the simulation remains incomplete. There is still room for improvement in the model and boundary conditions. Additionally, in the experiments, there may be interactions between the downward airflow in the surge vessel simulations and the upward heated airflow in this chapter's frame simulation. Furthermore, the thermocouples used in experiments may be positioned at random angles, and their distance from the frame is only an estimated number. Accurate simulation of the thermocouples' response requires consideration of many additional factors.

I

Calculation Process of Heat Transfer Contributions

This chapter provides a detailed description of the heat transfer contribution calculation process. The data used for the calculations are from Section 5.4.1, and the formulas are derived from Section 3.2.

I.1. Parameters

t = 124.2 s (experiment)
T = 288.44 K (environment T)
r = 1.25 m (geometry)
h_{dome} = 0.677 m (dome height)
A_{dome} = 6.349 m^2 (dome area)
A_{bot} = 4.909 m^2 (bottom area)

I.2. Gas Properties

Enthalpy of Vaporization (water):
ΔH_{vap} = 2260 KJ/kg
Thermal conductivity of air:
k = 0.0251 W/mK (Engineering Toolbox)
Prandtl number of air:
Pr = 0.71
Dynamic viscosity of air:
η =1.48 $\times 10^{-5}$ m^2/s
ρ_{water} = 997 kg/m^3

I.3. Condensation

The Tetens equation for estimating the saturation vapor pressure is given by:

$$P = 0.61078\exp\left(\frac{17.27\,T}{T+243.5}\right) \tag{I.1}$$

where, P is the saturation vapor pressure at temperature T (in Pa), T is the temperature (in °C).

Initial

$$P_{sat,ini} = 0.61078\exp\left(\frac{17.27\,T_{ini}}{T_{ini}+243.5}\right) = 1862pa$$

$$p_{vapor,ini} = 32.1\% \times P_{sat,ini} = 597.702pa$$

$$m_{water,ini} = m_{air} \times \frac{M_{water}}{M_{air}} \times \frac{p_{vapor,ini}}{p_{ini} - p_{vapor,ini}} = 0.00353097kg$$

Where, $\frac{M_{water}}{M_{air}}$ is 0.622.

After expansion

$$P_{sat,final} = 0.61078\exp\left(\frac{17.27\,T_{final}}{T_{final}+243.5}\right) = 739pa$$

$$p_{vapor,final} = 32.75\% \times P_{sat,final} = 597.702pa$$

$$m_{water,final} = m_{air} \times \frac{M_{water}}{M_{air}} \times \frac{p_{vapor,final}}{p_{final} - p_{vapor,final}} = 0.002737kg$$

$$\Delta m = 7.9397 \times 10^{-4}kg$$

$$Q_{condensation} = \Delta m \cdot \Delta H_{vap} = 1.7854kJ$$

I.4. Convection (ignore heat transfer from the ceiling)

$$Q_{convection} = h \cdot A \cdot \Delta T \cdot t \tag{I.2}$$

$$h = \frac{k \cdot Nu}{D} \tag{I.3}$$

Where, D = $\frac{(h_{ini}+h_{final})}{2}$ = 1.9265 m for vertical plane; D = 2r = 2.5 m for horizontal bottom plane.

Vertical plane

From Mill's book:

For $10^9 \le Ra_L < 10^{12}$:

$$\Psi = [1 + \left(\frac{0.492}{Pr}\right)^{9/16}]^{-16/9} = 0.347 \tag{I.4}$$

$$\overline{Nu_L} = 0.68 + 0.670\,(Ra_L\Psi)^{1/4}\left(1 + 1.6 \times 10^{-8}Ra_L\Psi\right)^{1/12} \tag{I.5}$$

$$Ra = \frac{\rho\beta\Delta T l^3 g}{\eta\alpha} \tag{I.6}$$

Where,

$$\bar{\rho} = \frac{\rho_{ini} + \rho_{final}}{2} = 1.6382kg/m^3$$

$$\beta = \frac{1}{\bar{T}} = \frac{1}{\frac{T_{min}+T_{final}}{2}} = 0.00366\frac{1}{K}$$

$$\Delta T = 15.39K$$

$$\bar{l} = \frac{h_{ini} + h_{final}}{2} = 1.9265m$$

$$g = 9.81m/s^2$$

So,

$$Ra = \frac{\rho\beta\Delta T l^3 g}{\eta\alpha} = \frac{1.6382 \times 0.00366 \times 15.39 \times 1.9265^3 \times 9.81}{1.48 \times 10^{-5} \times 1.91 \times 10^{-5}} = 2.290 \times 10^{10}$$

So,

$$Nu = 300.43$$

So,

$$h_{ver} = \frac{k \cdot Nu}{D} = \frac{0.0251 \cdot 300.43}{1.9265} = 3.914W/mK$$

$$Q_{ver} = h \cdot A \cdot \Delta T \cdot t = 3.914 \cdot 15.1307 \cdot 15.39 \cdot 124.2 = 113.198kJ$$

Horizontal bottom plane

From Frank's book:

For $10^7 < Ra_L < 10^{11}$

$$\overline{Nu}_L = 0.15Ra_L^{1/3} \tag{I.7}$$

$$Ra = \frac{\rho\beta\Delta T l^3 g}{\eta\alpha} = \frac{1.6382 \times 0.00366 \times 15.39 \times 2.5^3 \times 9.81}{1.48 \times 10^{-5} \times 1.91 \times 10^{-5}} = 5.004 \times 10^{10}$$

Note that I use the same β and ΔT value as the vertical calculation. Maybe using the bottom half average temperature is better. But I don't have the precise number of that now. It can be improved later.

So,

$$\overline{Nu}_L = 0.15Ra_L^{1/3} = 552.75$$

So,

$$h_{hor} = \frac{k \cdot Nu}{D} = \frac{0.0251 \cdot 552.75}{2.5} = 5.550W/mK$$

$$Q_{hor} = h \cdot A \cdot \Delta T \cdot t = 5.550 \cdot 4.909 \cdot 15.39 \cdot 124.2 = 52.077kJ$$

$$Q_{convection} = Q_{ver} + Q_{hor} = 113.198 + 52.077 = 165.275kJ$$

I.5. Radiation

$$q_{radiation} = N_{droplets}\left(\varepsilon_{wall}A_{droplet}\sigma T_{wall}^4 - \varepsilon_{water}A_{droplet}\sigma T_{droplet}^4\right) \tag{I.8}$$

Where $\sigma = 5.67 \times 10^{-8} W/m^2K^4$; $\varepsilon_{wall} = 0.78$ (for black paint); $\varepsilon_{water} = 0.9$.

$$r_{droplet} = 1\mu m$$

So,

$$A_{droplet} = 1.26 \times 10^{-11} m^2$$

$$V_{droplet} = 4.189 \times 10^{-18} m^3$$

$$m_{droplet} = \rho_{water} \times V_{droplet} = 4.176 \times 10^{-15} kg$$

$$N_{droplet} = \frac{\Delta m(\text{from condensation})}{m_{droplet}} = 1.901 \times 10^{11}$$

Take $T_{droplet}$ as the $\bar{T}$ in the previous calculation.

$$q_{radiation} = N_{droplets}\left(\varepsilon_{wall} A_{droplet} \sigma T_{wall}^4 - \varepsilon_{water} A_{droplet} \sigma T_{droplet}^4\right) = 53.82W$$

$$Q_{radiation} = q_{radiation} \times t = 6.684kJ$$

I.6. Work

$$W = \int PdV = \bar{p}\Delta V = 133858.8 \times 6.8277 = 913.948kJ \tag{I.9}$$

I.7. summary

Type	**Q /[kJ]**
condensation	1.7854
convection	165.275
radiation	6.684
work	913.948

J

Matlab Codes

J.1. Pressure Calculation from the RHT model

```
close all
clear all

file_path = ’RHT.xlsx’;
data = readmatrix(file_path);

gamma = 1.4;
p0 = 175892.6;

t = data(:,1);
V = data(:,2);
dQ_dt = -1463.176;
n = height(t);
p = zeros(n, 1);
p(1) = p0;

for i = 2:n
    dt = 0.1; % Time step
    dV_dt = (V(i) - V(i-1)) / dt; % Volume rate of change
    dp_dt = - gamma * (p(i-1) / V(i-1)) * dV_dt - (gamma - 1) / V(i-
1) * dQ_dt;
    % Update pressure
    p(i) = p(i-1) + dp_dt * dt;
end
```

J.2. Heat Transfer Model of air in the surge vessel for the full-scaled model

```
close all
clear all

% Air and other data
c_v_air = 720; % J/(kg*K)
g = 9.81;% m/s2
k_air = 0.027; % Wdot/m*K
Rs = 287; % specific gas constant of air

% Case 1 from Blue vessel measurements
casename = ['Case 1: p_{ini} = 0.70 barg'];
filename = 'SUMMARY_big_moving_case1.xlsx';
data = readtable(filename);
t = data{:, 1};
V_air_array = data{:, 4};
p_air = 170000;% Pa

% calculate dV/dt
dt = t(2) - t(1);
dV_air_dt = [diff(V_air_array);NaN]/dt;
D_vessel = 2.5; % vessel diameter m
T_air = 288; % K
rho_air = p_air./(Rs*T_air);
nR = p_air*V_air_array(1)/T_air; % constant nR, needed for ideal gas law
T_wall = 288; % K
mu_air = 1.8e-5; % dyn visc kg/m*s

% set initial values
V_air(1) = V_air_array(1);
V_air_new = V_air_array(2);
p_new = p_air(1);
T_new = T_air(1);
rho_air_new = rho_air(1);

disp('');
for i_time = 1:length(t)
    if i_time == 1
        % initial value
```

```
     E(i_time) = c_v_air*rho_air(i_time)*T_air(i_time)*V_air(i_time);
    else
        E(i_time) = Enew;
    end
    % update
    V_air(i_time) = V_air_new;
   L_wall(i_time) = V_air(i_time)./(pi*D_vessel); % height of wall in contact with ai
    T_air(i_time) = T_new;
    rho_air(i_time) = rho_air_new;
    % volume expansion coefficient
    Beta_air(i_time) = 1.0/T_air(i_time);

    % Qwall, Nu relation from Winterton book

   Ra_wall(i_time) = ((rho_air(i_time)^2)*c_v_air*g*Beta_air(i_time)*(T_wall -
T_air(i_time))*L_wall((i_time))^3)/(k_air*mu_air);
    Nu_wall(i_time) = 0.1*Ra_wall(i_time)^(1/3);
   h_wall(i_time) = Nu_wall(i_time)*k_air/L_wall(i_time); % Wdot/m2*K
   Q_wall(i_time) = h_wall(i_time)*(T_wall - T_air(i_time))*L_wall((i_time))*pi*D_ve

   % Qbottom: Nu relation from Winterton book (hor plate facing up, eq 4.34)
   Ra_bottom(i_time) = ((rho_air(i_time)^2)*c_v_air*g*Beta_air(i_time)*(T_wall -
T_air(i_time))*D_vessel^3)/(k_air*mu_air);
    Nu_bottom(i_time) = 0.145*Ra_bottom(i_time)^(1/3);
    h_bottom(i_time) = Nu_bottom(i_time)*k_air/D_vessel; % Wdot/m2*K
   Q_bottom(i_time) = h_bottom(i_time)*(T_wall - T_air(i_time))*pi*(0.5*D_vessel)^2

    % Work
    Wdot(i_time) = p_air(i_time)*dV_air_dt(i_time); % Wdot

    % Calculate dEdt and step in time
    Edot(i_time) = Q_wall(i_time) + Q_bottom(i_time) - Wdot(i_time);
    Enew = E(i_time) + dt*Edot(i_time);
    V_air_new = V_air(i_time) + dV_air_dt(i_time)*dt;
    p_new = Rs*Enew/(c_v_air*V_air_new);
    T_new = p_new*V_air_new/nR;
    rho_air_new = p_new./(Rs*T_new);

end
```